SEARCH FOR CONTACT INTERACTIONS USING THE DIMUON MASS SPECTRUM IN P-P COLLISIONS AT $\sqrt{S} = 8$ TeV AT CMS

by

CHAMATH KOTTACHCHI

DISSERTATION

Submitted to the Graduate School

of Wayne State University,

Detroit, Michigan

in partial fulfillment of the requirements

for the degree of

DOCTOR OF PHILOSOPHY

2014

MAJOR: PHYSICS

Approved by:

_____

Advisor   Date

_____

_____

_____

to Alfredo Gutierrez for the fruitful discussions we had during the CSC ME 4/2 and Gas Electron Multiplier (GEM) detector developments.

Many thanks go to the department chair, Ratna Naik; graduate advisor, Jogindra Wadehra; lab supervisor, Scott Payson, and all the faculty in the department for their support and advice in countless ways throughout my graduate studies. I would also like to acknowledge Delores Cowen, Hassan Hussein, Doris King, Lashara Montgomery, and Wynell Pitts for their excellent administrative support over the years.

A special thanks goes to the founders of the free education system in Sri Lanka, which has brought the nation's brightest minds to internationally renowned research efforts.

Finally, I would like to thank my family and friends for their love, kindeness, and constant encouragement at every step of my life.

TABLE OF CONTENTS

LIST OF FIGURES

LIST OF TABLES

Chapter 1

Introduction

The study of the fundamental building blocks of matter and their interactions is the main objective of particle physics. The current theory of particle physics is the standard model (SM) [1–4], which was formulated in the mid 1970s. It is a simple and comprehensive theory that explains the details of hundreds of particles and their complex interactions with only 6 quarks (fermions, spin 1/2), 6 leptons (fermions, spin 1/2), 4 force carrying particles (bosons, spin 1) and 1 recently discovered Higgs boson (spin 0). All known matter particles are composed of quarks and leptons, and they interact by exchanging force carrier particles. These force carrier particles, which include photons that are packets of electromagnetic radiation, three gauge bosons (W^+, W^- and Z) that carry the weak force, and gluons that carry the strong force, are responsible for holding fundamental particles together to form more complex objects. The standard model falls short of being a complete theory because it makes no predictions for several concepts including gravity, the number of quark and lepton generations, the pattern of increasing masses, dark matter, and dark energy. These features of the SM suggest that there might be some other new physics lurking at higher energies.

This dissertation describes the work related to searching for such new physics using the Compact Muon Solenoid (CMS) detector at the Large Hadron Collider (LHC) [5], currently operating underground in France near Geneva, Switzerland. The CMS detector is one of the two general-purpose detectors at the LHC and it has many of the same physics

goals as the ATLAS detector, except it uses different techniques and detector design to achieve these goals. The LHC is constantly increasing luminosity while accelerating the collection of data, and this analysis is based on 2012 CMS data at 8 TeV center of mass energy which corresponds to an integrated luminosity of 20.6 fb^{-1}. The increase of luminosity results in multiple collisions in a single bunch crossing, known as the so-called "pile-up effect", which require the use of special filters to reduce this effect and optimize the results.

The compositeness of atoms describes the structure of the periodic table and the compositeness of hadrons is described by the eightfold way [6]. Similarly, the arrangement of quarks and leptons in the SM might be described assuming those particles are not fundamental particles, but composite with more basic constituents called preons [7, 8]. The compositeness of quarks and leptons is described in the low energy limit by four-fermion contact interactions (CI) with compositeness energy scale Λ [9–11]. Constructive and destructive interference between contact interactions in the left-left iso-scalar model (LLIM) of quark compositeness and the SM are considered in this study of the dimuon mass distribution at center of mass energy 8 TeV. The existence of a new particle interaction due to quark and lepton compositeness will be manifested as a deviation from the SM predictions for the invariant mass spectrum of oppositely charged dimuon pairs.

The motivation to choose muons as the final state is based on the clean signature that muons can provide in the detector. The agreement between data and the SM predictions is tested first and if there is no significant deviation observed, 95% confidence interval exclusion lower limits are set on Λ for constructive and destructive interference using a modified frequentist statistical method.

The conceptual framework necessary to establish the standard model and possible physics scenario beyond the standard model (BSM) that incorporates the compositeness of quarks and leptons will be reviewed in Chapter 2. Chapter 3 details the experimental setup used to perform the search for compositeness. The analysis strategy of the study is given in Chapter 4. Chapter 5 explains the Monte Carlo generators used, while CMS data and event selection are explained in Chapter 6. Full simulation of the contact

interaction signal (CI/DY) and background events (standard model DY and non$-$DY backgrounds) are described in Chapter 7. Chapter 8 presents the estimation of systematic uncertainties and Chapter 9 discusses the statistical methods used to determine the limits on compositeness energy scale Λ. Finally, results and the conclusion are given in Chapter 10.

Chapter 2

Theoretical Background

This chapter reviews the theoretical background of the standard model, the theory of the electroweak interaction and the four-Fermi interaction. The motivation for searching for new physics that lies beyond the standard model is also addressed.

2.1 The Standard Model of Particle Physics

The standard model of particle physics is a relativistic quantum field theory (QFT) [12] that incorporates the basic principles of quantum mechanics with special relativity. Similar to quantum electrodynamics (QED) [13–17], the standard model is a gauge theory with the non-Abelian gauge group $SU(3)_C \times SU(2)_L \times U(1)_Y$, rather than having the simple Abelian $U(1)_{em}$ gauge group of QED. The fundamental particles which have been observed can be divided into two main categories based on their spin: the spin-1/2 fermions with which matter is formed and the spin-1 gauge bosons which are responsible for mediating the fundamental forces. The standard model explains three of the four known fundamental interactions: the electromagnetic, the weak, and the strong. Even though gravity does not fit into the SM, some theories predict that the force may be mediated by an electrically neutral and massless spin-2 hypothetical particle known as the graviton. The SM allows every particle to have an anti-particle with the same mass and spin but charged oppositely. The remarkable success of the SM suggests that it is an excellent approximation to nature down to the distance scale 10^{-18} m.

Fermions in the standard model can be divided into two categories: quarks and leptons. Quarks come in six different flavors and carry fractional charges: up (u), charm (c), and top (t) quarks have charge +2/3; down (d), strange (s), and bottom (b) quarks have charge -1/3 in units of the proton charge. These quarks are subject to all three of the fundamental interactions in the SM: the strong, weak, and electromagnetic interactions, and cannot exist freely; therefore, they always group together by forming hadrons. Leptons also come in six different flavors and can be generally divided into two groups: electron (e^-), muon (μ^-), and tau (τ^-) with charge -1 in units of the proton charge, and electron neutrino (ν_e), muon neutrino (ν_μ), and tau neutrino (ν_τ) with no charge. The leptons only interact by electromagnetic and weak forces; they do not participate in any strong interactions since leptons do not carry color-charge. Generally, all the quarks and leptons are grouped into three generations as shown in Table 2.1.

Table 2.1. Generations of quarks and leptons in the SM.

	Leptons			Quarks		
Generation	Flavor	Charge	Mass (MeV/c^2)	Flavor	Charge	Mass (MeV/c^2)
1	e	-1	0.511	u	+2/3	1.5 - 4.5
	ν_e	0	$< 3 \times 10^{-6}$	d	-1/3	5 - 8.5
2	μ	-1	105.7	c	+2/3	(1.0 - 1.4) $\times 10^3$
	ν_μ	0	< 0.19	s	-1/3	80 - 155
3	τ	-1	1777	t	+2/3	(172.6 ± 1.4)$\times 10^3$
	ν_τ	0	< 18.2	b	-1/3	(40 - 4.5) $\times 10^3$

In the SM, the interactions between particles are explained in terms of exchanging bosons, integer-spin elementary particles which are carriers of the fundamental interactions. The main characteristics of the bosons are listed in Table 2.2, excluding the gravitational interaction. The photon is a massless spin-0 particle, which is responsible for mediating the electromagnetic interactions between charged particles. The W$^\pm$ and Z bosons mediate the weak force, and have charges of ± 1 and 0, respectively. The gluons mediate the strong force, and are electrically neutral and massless. Unlike the other force carriers, gluons carry a unit of color and anti-color, which give them the ability to have

self-interactions.

Table 2.2. The fundamental interactions in the SM.

Interaction	Mediator	Charge	Spin	Mass (GeV/c^2)	Range (m)	Relative Strength
Strong	Gluon (g)	0	1	0	10^{-15}	1
EM	Photon (γ)	0	1	0	∞	1/137
Weak	W$^\pm$	± 1	1	80.42	10^{-18}	10^{-5}
	Z^0	0	1	91.19	10^{-18}	10^{-5}

Electromagnetic Interactions

The electromagnetic interaction exists between all electrically charged particles and is governed by the theory of Quantum Electrodynamics (QED). This interaction is mediated by the photon, a massless particle. The coupling constant g_e of a photon to a charged particle depends on the fine structure constant ,α, as shown in the equation below,

$$g_e = \sqrt{4\pi\alpha} \tag{2.1}$$

where,

$$\alpha = \frac{e^2}{\hbar c} \approx \frac{1}{137}. \tag{2.2}$$

Since photons are massless, the electromagnetic force is considered a long-range interaction, and is responsible for nearly all the forces we feel on the macroscopic level, excluding gravitational force. This interaction is also responsible for holding electrons and protons together to form atoms.

Weak Interactions

The weak interaction is responsible for radioactive decays, and is characterized by long lifetimes and small cross sections. This interaction is mediated by massive W$^\pm$ and Z^0 bosons; due to the massiveness of these mediators, the weak interaction is short range. The masses of W$^\pm$ and Z^0 vector bosons are approximately 80 GeV/c^2 and 91 GeV/c^2, respectively. The weak interaction can act between quarks, charged leptons, and neutral leptons. The neutral current interaction involves the exchange of Z^0 bosons and couples to all fundamental particles, excluding the photon and the gluon. The charged current interaction involves the exchange of W$^\pm$ bosons and couples to all fundamental particles

except the gluon. The charged current interaction can change a charged lepton into its neutrino partner, or change a quark's flavor from up-type to down-type, or vice versa.

Strong Interactions

The third fundamental interaction, the strong interaction, is explained as the interaction between quarks and gluons which leads to the creation of nuclear matter. The strong coupling constant, α_s, is given by

$$\alpha_s = \frac{g_s^2}{4\pi} \approx 1, \tag{2.3}$$

in units where $\hbar = c = 1$. Quantum chromodynamics (QCD) is the theory that explains the properties of the strong interaction, and according to QCD, each quark has a color-charge: red (R), green (G), or blue (B). Quarks carry one of these colors and anti-quarks carry the corresponding anti-colors: anti-red ($\bar{R}$), anti-green ($\bar{G}$), and anti-blue ($\bar{B}$). Additionally, gluons also carry color-charges and can interact with themselves.

The strong interaction is unique in a number of ways since gluons have the ability to interact with themselves. This interaction gets stronger when the separation distance between color-charge particles increases. If a quark separates from another, the energy released as a result from the separation is enough for another quark-antiquark pair to pop into existence from the vacuum. The original quark then combines with these new particles in the process known as hadronization. Hadronization is driven by asymptotic freedom and quarks are restricted to be in a colorless bound state in nature.

2.2 The Fermi Interaction

The nuclear decays, $\alpha-$decay and $\gamma-$decay, which emit helium nuclei (α) and photons (γ), were observed with discrete energy spectra as suggested by theories. But the nuclear $\beta-$decay, where a neutron was observed to decay into a proton by emitting an electron, created a great deal of anxiety among particle physicists. In $\beta-$decay, the electron energy spectrum was observed to be a continuous spectrum, challenging the law of energy conservation; this continuous $\beta-$spectrum was puzzling to physicists.

In 1930, Wolfgang Pauli postulated that a new particle was also emitted in $\beta-$decay,

(a) Fermi's beta decay

(b) Present understanding of beta decay
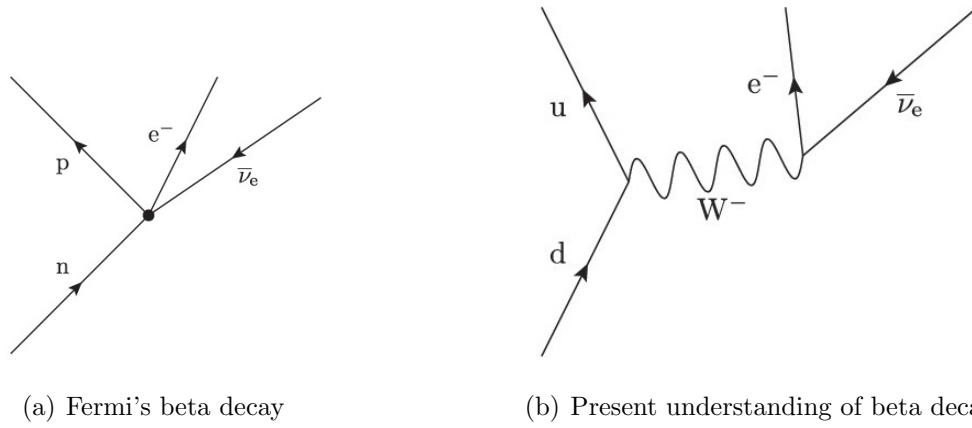
FIG. 2.1. Fermi's 4-fermion beta decay and present understanding of beta decay.

in an attempt to solve the energy conservation problem. But this new particle would have to be very light or massless to be consistent with the $\beta-$decay energy spectrum, and neutral to have avoided detection [18]. Based on this idea, Enrico Fermi postulated a 4-fermion contact interaction for $\beta-$decay as n $\rightarrow$ p + e$^-$ + $\bar{\nu}$, which happens at a single point in space-time, introducing a neutral particle called a "neutrino" [19]. However, the present understanding of $\beta-$decay is mediated by the massive gauge bosons, W$^{\pm}$. Fermi's idea and the present understanding of $\beta-$decay are shown in Figure 2.1.

2.3 The Electroweak Interaction

Electric and magnetic fields were considered two different phenomena without any connection until J.C. Maxwell and others formed the theory of electromagnetism, unifying these two fields in the 1860s. Similarly, electromagnetic and weak interactions are combined to form the electroweak theory. In 1961, Glashow discovered a way to combine the electromagnetic and the weak interactions, and postulated that both forces are manifestations of a single force called the electroweak force [20].

The weak interaction is explained by the $SU(2)_L$ group, generated by weak isospin I. The subscript L indicates that the weak force only interacts with left-handed particles. The electromagnetic interaction is mathematically described by the $U(1)_{em}$ group. The electroweak theory developed by Glashow was able to unify those two groups into a single

gauge group in the form of $SU(2)_L \times U(1)_Y$, with the weak hypercharge Y generating $U(1)_Y$. The new symmetry group is well-behaved above the electroweak scale, since all the fields corresponding to the unified group are predicted to be massless. But some other mechanism was required to break the $SU(2)_L \times U(1)_Y$ symmetry below the electroweak energy scale, and to give the weak gauge bosons mass. This was achieved by introducing spontaneous symmetry breaking, via the Higgs mechanism [21, 22] by S. Weinberg and A. Salam in 1967.

The Glashow-Weinberg-Salam (GWS) model eventually became what is known as the standard model of particle physics today. The precision of this model is remarkably high, holding up against experimental discoveries during last 45 years. The discovery of the tau lepton took place at the Stanford Linear Accelerator Center (SLAC), confirming the existence of the third generation of fermions in 1975 [23]. The Fermi National Accelerator Laboratory (FNAL) claimed the discoveries of the bottom quark in 1977 [24], and the top quark in 1995 [25, 26]. The tau neutrino was also observed at FNAL, confirming the third generation of neutrinos in 2000 [27]. The last missing piece of the standard model, the Higgs boson, was discovered in 2012 and confirmed in 2013 by the CMS and ATLAS experiments at CERN [28, 29].

2.4   Beyond the Standard Model

Although the standard model of particle physics successfully predicts and describes many fundamental particle processes with very high accuracy, there are some shortcomings within the theory. The discovery of the Higgs boson completes the SM, but has also left many important questions unanswered, such as: Why there are only three generations of fermions? Why does the SM not incorporate gravity or explain the method necessary to calculate the masses of quarks and leptons? Why are there four different forces? What happened to the dark matter and dark energy which is believed to make up 96% of the universe according to cosmological evidence? The SM also does not explain the reason behind the matter and anti-matter asymmetry. Neutrino oscillation experiments discov-

ered that neutrinos have mass, while the SM describes neutrinos as massless particles. The theory of beyond the standard model (BSM) is another possible theory to find the answers to many unanswered questions involved with the SM. There are a wide range of new physics searches that include extra dimensions, super-symmetry, new gauge bosons, and quark and lepton compositeness.

2.4.1 Four-Fermion Contact Interactions

The most appealing evidence for the presence of new physics beyond the standard model at the LHC would be the direct observation of a new particle appearing as a resonance or an excess in the number of events in the spectra at high masses. Contact interactions (CI) can provide important signals for possible new physics observations at the LHC. The concept of CI was first used by Fermi to explain the process of $\beta-$decay long before the discovery of the $W^{\pm}$ bosons; similarly, one can write an effective Lagrangian containing a new vector interaction occurring at a compositeness energy scale (Λ) without exactly knowing the intermediate process. The compositeness energy scale can be much higher than the designed maximum energy at the LHC, but its effects can be still detectable at energies much below Λ.

An experimental signal for contact interactions is a non-resonant enhancement of the expected dilepton (dimuons or dielectrons) events at high masses. In the case where both quarks and leptons share common constituents, it is possible to write the Lagrangian density for the four-fermion contact interactions [30] in the dimuon final state with the equation,

$$
\begin{aligned}
L_{ql} \quad &= (g_0^2/\Lambda^2)\{\eta_{LL}(\bar{q}_L\gamma^\mu q_L)(\bar{\mu}_L\gamma_\mu\mu_L) + \eta_{LR}(\bar{q}_L\gamma^\mu q_L)(\bar{\mu}_R\gamma_\mu\mu_R) \\
&\quad +\eta_{RL}(\bar{u}_R\gamma^\mu u_R)(\bar{\mu}_L\gamma_\mu\mu_L) + \eta_{RL}(\bar{d}_R\gamma^\mu d_R)(\bar{\mu}_L\gamma_\mu\mu_L) \\
&\quad +\eta_{RR}(\bar{u}_R\gamma^\mu u_R)(\bar{\mu}_R\gamma_\mu\mu_R) + \eta_{RR}(\bar{d}_R\gamma^\mu d_R)(\bar{\mu}_R\gamma_\mu\mu_R)\}
\end{aligned}
\tag{2.4}
$$

where, $q_L = (u,d)_L$ is a left-handed quark doublet, u_R and d_R are right-handed quark singlets, and μ_L and μ_R are the outgoing left-handed and right-handed muons. By convention, $g_0/4\pi =1$. The sign factor η is, -1 for constructive and +1 for destructive
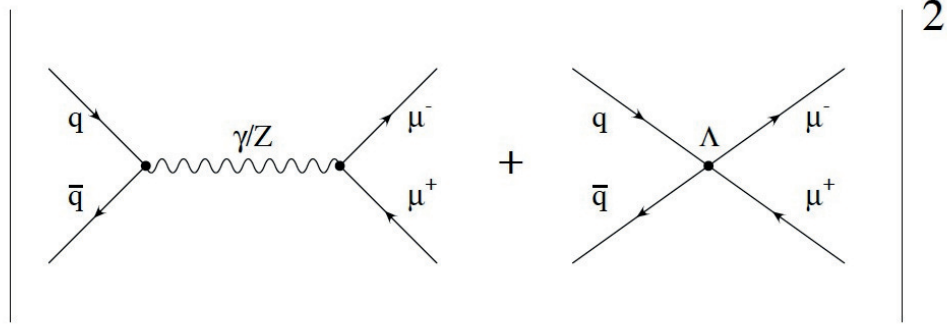
FIG. 2.2. Production mechanism of DY with additional contact interaction term with compositeness energy scale, Λ in the dimuon final state

interference. The compositeness energy scale Λ, is potentially different for each of the individual terms in the Lagrangian, so lower limits on Λ are set separately for the individual currents appearing in Equation 2.4.

Since the standard model DY dimuon production and CI dimuon production have identical final states, as shown in Figure 2.2, their scattering amplitudes are added together. The observed differential cross section is given by

$$\frac{d\sigma}{dm}(\Lambda) = \frac{d\sigma}{dm}(DY) - \eta\frac{I(m)}{\Lambda^2} + \eta^2\frac{C(m)}{\Lambda^4} \qquad (2.5)$$

where m is the dimuon invariant mass, $I(m)$ is magnitude of the product of DY and CI amplitudes, and $C(m)$ corresponds to the magnitude of the square of the contact interaction term.

2.4.2 Manifestation of Compositeness

One possible explanation for the mass hierarchy problem in the standard model is that quarks and leptons might not be fundamental particles. They could be composite made of constituents, often referred in the literature as "preons". In order to confine the constituents and to account for the properties of quarks and leptons, a new gauge interaction, "metacolor", is introduced. Below a given interaction energy scale Λ, the effect of the metacolor interaction is to bind the preons into metacolor-singlet states. For proton--proton center of mass energy values that are much less than the Λ energy scale, the

metacolor interaction will manifest itself in the form of a flavor-diagonal contact interaction. However, given the present limits on substructure within quarks and leptons, it is expected that Λ will be at least of the order of TeV.

The left-left isoscalar model (LLIM) of quark compositeness [10], which is the conventional benchmark model for contact interactions [31], is used in this analysis. This model corresponds to the first term of the Lagrangian, L_{ql}, in Equation 2.4, and assumes all the initial state quarks are composite objects.

2.4.3   Review of Previous Searches

Past quark and lepton compositeness studies were performed by almost all the leading particle physics experiments in dilepton and dijet final states. However, there is no direct evidence to confirm the concept of compositeness, and all experiments resulted in exclusion lower limits on the compositeness energy scale Λ.

The Hadron Electron Ring Accelerator (HERA) at DESY collided proton and electron, or positron beams, for experiments [32, 33] from 1992 to 2007. The Large Electron-Positron Collider (LEP) at CERN used electron and positron beams during its operations from 1989 to 2000 [34–36]. The Tevatron at Fermilab used proton and anti-proton beams for compositeness studies at a center of mass energy of 1.96 TeV [37–39] from 1983 to 2011. Recent studies on quark compositeness were performed by the ATLAS [40, 41] and CMS [42, 43] experiments at CERN using proton-proton collisions at a center of mass energy of 7 TeV. The most stringent limits in quark compositeness using LLIM for dimuon final states are currently $\Lambda > 13.1$ TeV for constructive interference and $\Lambda > 9.5$ TeV for destructive interference at the 95% confidence level [43].

2.5   Collider Physics

The understanding of the compositeness and the internal structure of protons depends on the energy scale with which it is probed. The substructure of the proton cannot be resolved at low energies as it behaves like a point-like particle. Static properties of a

proton, such as electric charge and quantum numbers, are determined by two up-type quarks and one down-type quark (uud), referred to as valence quarks. However, the actual structure inside the proton is far more complex than the uud model. The proton structure includes contributions from a large number of virtual quark-antiquark pairs, commonly known as sea quarks, valence quarks, and gluons. The dynamics of protons can be understood by studying how the proton momentum is distributed among the constituent partons; here, parton refers to quarks and gluons. Note that at the LHC, the Drell-Yan processes ($q\bar{q} \rightarrow Z/\gamma^* \rightarrow l^+l^-$) can occur only by utilizing an anti-quark from the available sea quarks. Parton distribution functions (PDFs) [44] are defined to predict the rates of various processes that occur via these partonic constituents of the protons. The PDFs, $F_a(x_A, Q^2)$, represent the probability density of a parton a in hadron A that carries a momentum fraction of x_a, when probed at a momentum transfer scale Q^2. The PDF may include terms up to leading order (LO), next-to-leading order (NLO), next-to-next-to-leading order (NNLO), and so on, and may be expressed as a power series expansion in the coupling constant α_s. The groups that produce PDF sets for LHC are CTEQ [45], MSTW [44], and NNPDF [46]. The MSTW NLO PDF of the proton is illustrated in Figure 2.3.

Although the valence quark constituents of a proton play a major role in PDFs, a large fraction of the proton momentum is carried by gluons and sea quarks. Since the number of these sea particles depend on the momentum of the proton, the calculation of the full production cross section is complicated. Therefore, the QCD factorization theorem [47] is used in these hadron-hadron collisions. This theorem states that the total cross section can be seperated into two parts: the hard scattering interaction between the two colliding partons, and the PDFs for those partons. If hadrons A and B interact to produce X, the cross section for the process can be determined from the convolution of the cross section of the interacting partons a and b, and the PDFs of the hadrons:

$$\sigma(A + B \rightarrow l^+l^- + X) = \sum_a \int dx_A dx_B F_a(x_A, Q^2) F_{\bar{a}}(x_B, Q^2)\sigma_{a\bar{a} \rightarrow l^+l^-}(Q^2), \qquad (2.6)$$
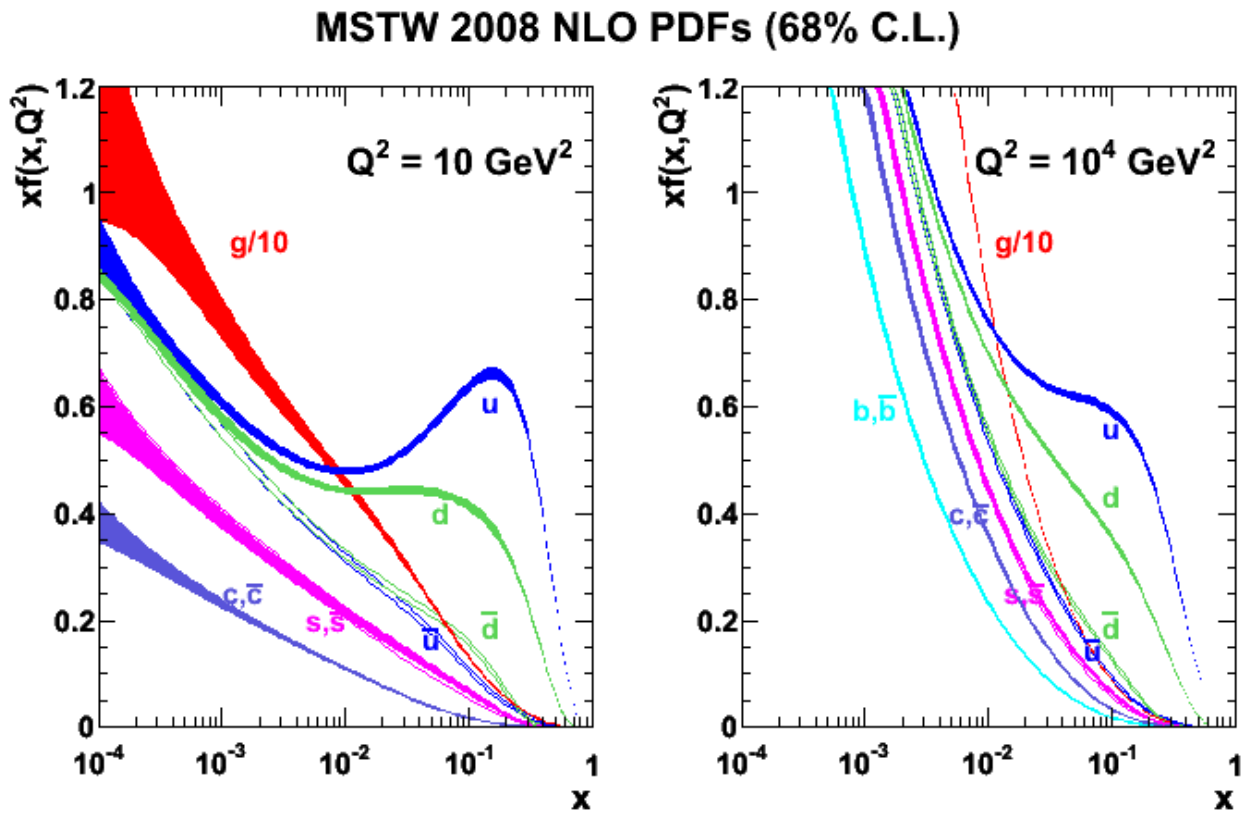
FIG. 2.3. MSTW 2008 NLO PDFs at momentum transfer scale of 10 $(\text{GeV/c})^2$ and 10^4 $(\text{GeV/c})^2$ [44].

where x_A and x_B are the momentum fractions of hadrons A and B carried by partons a and b respectively, $\sigma_{a\bar{a}\rightarrow l^+l^-}$ is the hard scattering cross section, and X is everything else that exists from left over proton fragments. This is usually known as the QCD underlying event.

The hard scattering is not the only interaction which occurs in a proton-proton collision; photons or gluons are radiated as initial and final state fermions accelerate in the collision. The initial state radiation (ISR) occurs as the incoming quarks become asymptotically free, and the final state radiation (FSR) occurs due to the radiation of photons from leptons produced after the hard scattering.

In a proton-proton collision, more than one pair of partons may interact, known as a multiparton interaction (MPI); this should be accounted for when calculating the hadron-hadron interaction cross section. These interactions are relatively more visible due to the higher center of mass energy of the colliding beams at the LHC.

The valence and sea quarks of the proton that are not participating in MPI are often called proton remnants. These beam remnants travel in the same direction as their parent proton, and are color connected to the hard scattering. The proton remnants are not free particles; this can cause quark-antiquark pairs and gluons to be produced from the vacuum, which in turn may radiate gluons and decay into more quark-antiquark pairs. This process is known as a parton shower (PS), which typically assumes that the transverse momentum of emitted gluons is small. The quarks undergo hadronization, where they bind together into colorless states and form hadrons that may be unstable and decay further. This complex parton showering and hadronization are handled differently and effectively by event generators that simulate signal and background physics processes.

The program PYTHIA is a full event generator to handle hard scattering at LO accuracy that uses the LO PDF set CTEQ6L1. The program MC@NLO is a hard event generator at NLO accuracy which can be interfaced with the HERWIG MC generator for showering. The MC@NLO generator uses the NLO PDF set CTEQ6M [45]. The program POWHEG is another hard event generator for heavy quark production in hadronic collisions at NLO accuracy. The HERWIG and HORACE generators are also used in this

anlaysis to generate events as described in Section 5.1.

Chapter 3

The Experimental Apparatus

This chapter introduces the experimental setup used to collect data to find quark and lepton compositeness using proton-proton collisions. After a brief overview of the Large Hadron Collider, the CMS detector is described highlighting the main features of the sub-detectors, driven by physical requirements.

3.1   The Large Hadron Collider

The Large Hadron Collider (LHC) [48–50], which is located at CERN near the city of Geneva, on the border of Switzerland and France, is the largest and the highest energy particle accelerator in the world. It was installed in the 26.7 km tunnel constructed for the former Large Electron-Positron Collider (LEP). The collider contains high frequency accelerating cavities, focusing quadrapole magnets, and superconducting dipole magnets for bending protons in the plane of the accelerating ring. Some 1232 superconducting dipole magnets are needed which operate at a design field of 8.3 T, and are maintained at a fixed temperature via superfluid helium at 1.9 K. Also, two separate beam pipes are incorporated for proton beams to circulate in opposite directions. The LHC is designed to produce proton-proton collisions up to a center of mass energy of 14 TeV.

The LHC startup was in September 2008, but due to an accident caused by a failure in an interconnection between two magnets, the operation was stopped and not restarted until March 2010. In the following years, the LHC was running at $\sqrt{s} = 7$ TeV in 2010
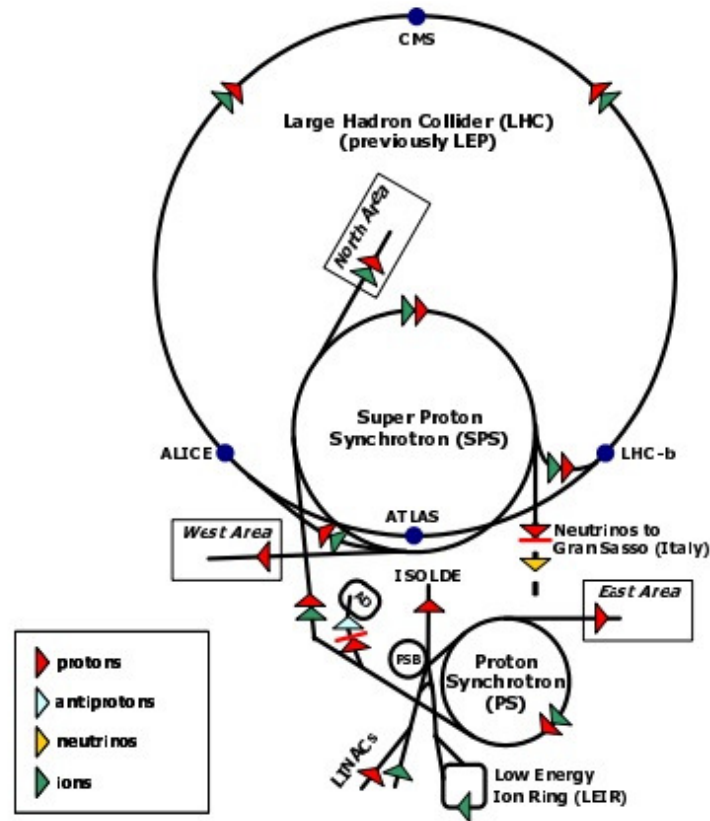
FIG. 3.1. Overview of the CERN accelerator system [51].

and 2011, and $\sqrt{s} = 8$ TeV in 2012.

The main reason to choose a proton-proton collider (as opposed to an electron-positron collider) is the need to reach a very high energy without great loss due to synchroton radiation, which is proportional to the fourth inverse power of mass of accelerated particles. The protons are accelerated up to 50 MeV by the LINAC (LINear ACcelerator) and put into the Proton Synchroton Booster (PSB) to accelerate up to 1.4 GeV. Protons are grouped in bunches and accelerated further, up to 26 GeV, in the Proton Synchroton (PS) with the correct bunch spacing, and then are injected into the Super Proton Synchroton (SPS), which accelerates them up to 450 GeV. Finally, the proton bunches are transferred into the two rings of the LHC, circulating with guidance of high field superconducting magnets cooled by a huge cryogenics system. An overview of the CERN accelerator complex can be seen in Figure 3.1. Additionally, there are four experiments operating on the ring: CMS (Compact Muon Solenoid) [52], ATLAS (A Toroidal LHC ApparatuS) [53], LHCb (Large Hadron Collider beauty experiment) [54], and ALICE (A
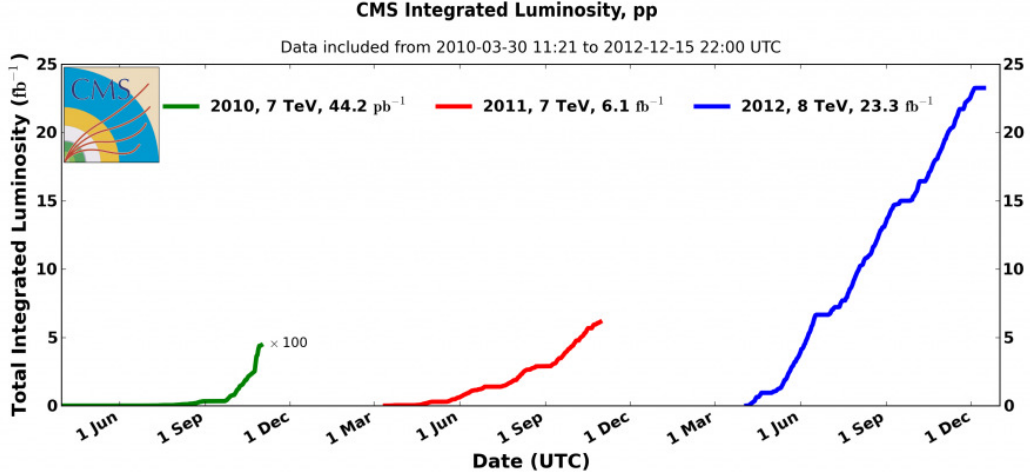
FIG. 3.2. Development of the integrated luminosity from LHC proton-proton collisions at the CMS interaction region during 2010 (green), 2011 (red) and 2012 (blue).

Large Ion Collider Experiment) [55].

One of the most important parameters of an accelerator is the instantaneous luminosity, L [56], which is related to the total cross section σ of the process under study, and to the average expected event rate for that process $\langle dN/dt \rangle$ by the relation

$$L = \frac{\langle dN/dt \rangle}{\sigma}.$$

Accordingly, the integrated luminosity, $\mathcal{L} = \int_{t_0}^{t_0 + \Delta t} L\, dt$, of a dataset recorded during a time interval Δt specifies the average expected number of events $\langle N \rangle$ for a given cross section σ. Figure 3.2 shows the evolution of the integrated luminosity at the CMS experiment during 2010, 2011, and 2012 proton-proton data collections.

3.2   The Compact Muon Solenoid Experiment

The CMS experiment is one of two general purpose experiments that collect data at the LHC. Its aim is to investigate a wide range of possible interactions, including the Higgs boson search, which was reported in July of 2012, and searching for new physics beyond the standard model. The main body of the CMS detector has a diameter of about 14 m and a length of about 22 m, which is roughly a cylindrical shape. The overall layout of CMS is shown in Figure 3.3.
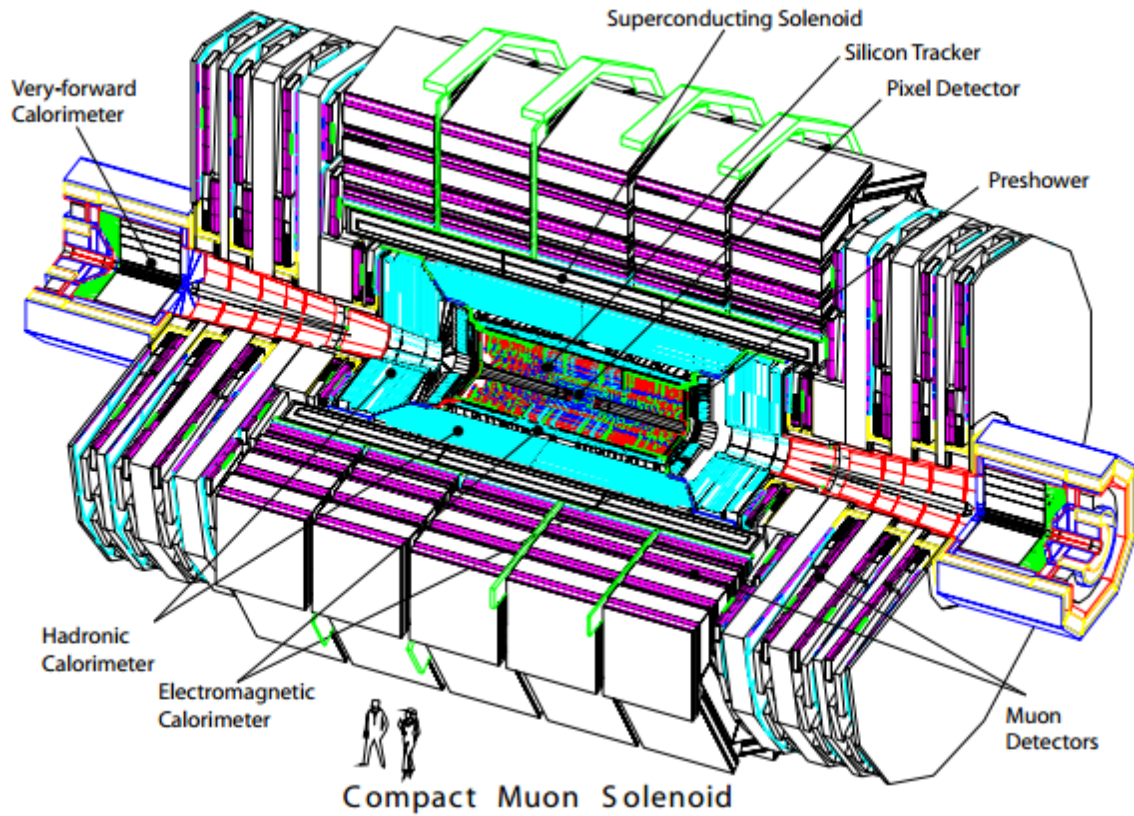
FIG. 3.3. An overview of the CMS detector.

The central feature of the CMS apparatus is a superconducting solenoid with an internal diameter of 6 m, providing a magnetic field of 3.8 T. The magnet allows for a compact design of the detector, and ensures a very good muon momentum resolution, along with dimuon invariant mass resolution and high capability to determine unambiguosly the charge of muons up to 1 TeV.

The CMS detector is designed to operate under challenging conditions, such as a high rate of collisions and a large number of multiple interactions overlapping in the same event. Products of different collisions within the same bunch or even different bunches can pile up in the same event.

3.2.1   Coordinate System

CMS uses a right-handed coordinate system that has the origin centered at the nominal collision point, the y axis pointing vertically upward, the x axis pointing radially inward toward the center of the LHC, and the z axis along the beam line. Since the CMS

detector has cylindrical symmetry around the z axis, a cylindrical coordinate system is more convenient given by the radius r, i.e., the distance from the z axis, the azimuthal angle ϕ defined from the x axis in the $x - y$ plane (transverse plane), and the polar angle θ measured from the $z-$ axis. The projection in the $r - z$ plane, where $r = \sqrt{x^2 + y^2}$, defines a longitudinal plane. The pseudorapidity $\eta \in [-\infty, \infty]$ is defined as

$$\eta = -\ln \tan \left(\frac{\theta}{2} \right). \tag{3.1}$$

The pseudorapidity of a particle with four-momentum $p^\mu = (E, p_x, p_y, p_z)$ converges to the rapidity

$$h = \frac{1}{2} \ln \left(\frac{E + p_z}{E - p_z} \right), \tag{3.2}$$

in the limit $m^2 = E^2 - \bar{p}^2 \to 0$; the rapidity is linear under a longitudinal Lorentz boost. The transverse momentum p_T is defined as the magnitude of the projection of the three momenta on the transverse plane, $p_T = \sqrt{p_x^2 + p_y^2}$, and the transverse energy is defined as $E_T = E \sin \theta$.

The CMS detector is longitudinally segmented into a central part (barrel), covering the range $|\eta| \leq 1.3$, and two lateral segments (endcaps), covering $0.9 \leq |\eta| \leq 2.4$. Both the barrel and the endcaps are equipped with an electromagnetic calorimeter (ECAL), a hadronic calorimeter (HCAL), and muon detectors, while vertexing and tracking detectors are only contained in the barrel. The barrel muon system is comprised of drift tubes (DTs) and resistive plate chambers (RPCs) while the endcap muon system consists of RPCs and cathode strip chambers (CSCs).

The endcaps are subject to a higher flux of radiation than the barrel, requiring more radiation-hardness than the barrel. The tracking detectors and the calorimeters are hosted inside the superconducting coil, while the muon detectors are integrated within the iron return yoke. Figure 3.4 shows a transverse slice of the detector barrel, with particle trajectories traversing the detector material.
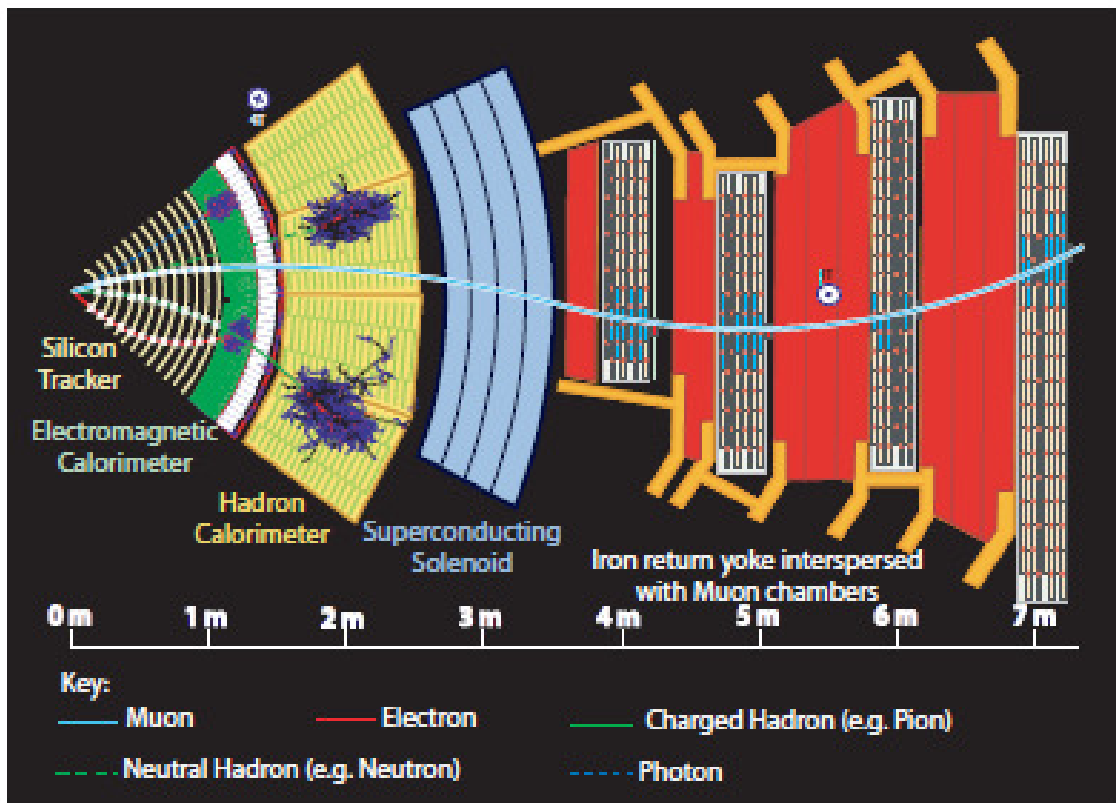
FIG. 3.4. Transverse view of the CMS detector, showing particle trajectories traversing the detector material.

3.2.2 Superconducting Magnet

The CMS magnet [57] is a large superconducting solenoid currently operating at a central magnetic field of 3.8 T. However, after the first years of operation, once the aging of the coil is better understood, it may reach the design field of 4 T [58]. The flux is returned through a 10,000 ton iron yoke comprised of 5 wheels and 2 endcaps, composed of 3 disks each. The main role of each disk is to increase the field homogeneity in the tracker volume, and to reduce the extra field by returning the magnetic flux of the solenoid. The magnet parameters are given in Table 3.1.

Table 3.1. CMS superconducting solenoid parameters.

Field	4 T
Inner Bore	5.9 m
Length	12.9 m
Number of turns	2168
Current	19.5 kA
Stored energy	2.7 GJ
Hoop stress	64 atm

3.2.3 Tracking Detectors

Tracking detectors [59] are used to reconstruct the trajectories of electrically charged particles, known as tracks. In the presence of a magnetic field, the bending of the track can be used to measure the momentum component transverse to the field. The CMS inner tracker measures the tracks from charged high-energy particles emitted during a given bunch crossing. In CMS, associating reconstructed particles with a specific proton-proton interaction from the bunch crossing relies heavily on the information provided by the inner tracker. The CMS muon system, embedded in the magnet yoke, is also designed as a tracking detector. The high material budget between the collision point and the muon system implies low background rates from particles emitted from the proton-proton collisions other than muons, as most of their energy is expected to be abosorbed in the calorimeters.

Inner Tracking System

The inner tracking system [60,61] allows the reconstruction of charged particle tracks, from which the primary and displaced vertices can be identified. This is designed to provide a precise and efficient measurement of the trajectories of charged particles coming from LHC collisions. It is placed in the inner part of the apparatus, completely immersed in the 4 T magnetic field generated by the solenoid. It extends for a length of 5.8 m, has a diameter of 2.5 m, and is centered around the interaction point.

The reconstruction of charged particle tracks can be decomposed into four logical parts: reconstruction of the track impact positions in the pixel and strip sensors (hits), generation of track seeds with the pixel hits, pattern recognition, and final fit of the track. The hit reconstruction consists of the clustering of the energy depositions in pixel and strip sensors. The hit positions and their uncertainties are estimated in the local coordinate frames of the sensors and then are transformed into the global CMS coordinate system for the subsequent reconstruction steps.

The CMS inner tracking system is subdivided into two subsystems: the silicon pixel detector and the surrounding silicon strip detector. The layout of the tracker is shown in Figure 3.5. The pixel detector system is the detector component closest to the interaction region of the colliding proton beams. It consists of three cylindrical layers with the beam pipe in the center and two transverse disk components on each side. In both transverse and longitudinal directions, the achieved spatial resolution for each layer is $\approx 9~\mu$m.

The silicon strip tracker covers $|\eta| < 2.5$. Its modules are arranged in barrel and end-cap sections. Each module has either one "thin" detection layer or two "thick" detection layers that feature a small angle between their strip directions. This angle allows for a position measurement along the direction of the strips. For the region $|\eta| < 2.4$, tracks are likely to traverse nine or more measurement layers.

3.2.4   Calorimeter

Calorimeters are designed to absorb the total energy of particles and provide a signal with a well-understood relation to this energy. Subdividing the calorimeter into subunits
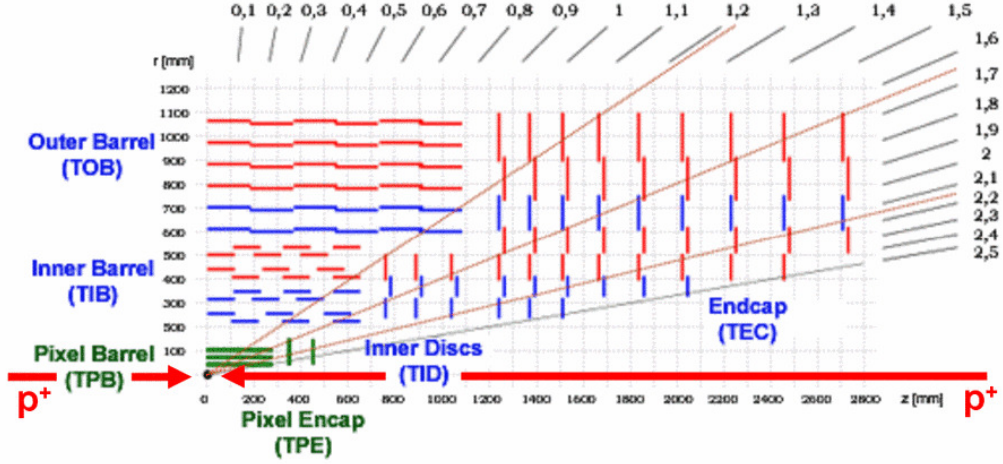
FIG. 3.5. View of the CMS tracker silicon layers projected in the longitudinal plane. The green shows the pixel detector and the red and the blue show the silicon track layers.

allows information recovery about the direction of flight of the measured particles and details about their showering into other particles during the process of energy deposition. The main subsystems of the CMS detector are the electromagnetic calorimeter (ECAL) and the hadron calorimeter (HCAL).

Electromagnetic Calorimeter

The ECAL [62,63] is important for the identification of electrons and photons, and allows for a precise measurement of their energies. Its high granularity in the ϕ and η directions improves the precision at which the direction of the incident electrons and photons are determined.

The ECAL consists of about 75,000 active cells made of lead tungstate (PbWO$_4$), packed together into a quasi-projective structure. Lead tungstate is chosen because of its small radiation length ($X_0 = 0.89$ cm) and moliere radius ($R_M = 2.2$ cm), thus making it ideally suited to be deployed for high granularity calorimeters inside the reduced volume of the coil. In addition, PbWO$_4$ is particularly radiation-hard and the decay life of the scintillation light is short enough to ensure that 80% of the light yield is delivered before a new collision occurs.

The energy resolution $\sigma(E)/E$ has been measured in test beam studies and it is parametrized as

$$\frac{\sigma(E)}{E} = \frac{2.8\%}{\sqrt{E(GeV)}} \oplus \frac{12\%}{E(GeV)} \oplus 0.3\%. \tag{3.3}$$

At high energies, the resolution is dominated by the constant term which is connected to the control of energy leakage, non-uniformities in the light collection, and inter-calibration between different ECAL components. During data collection, this term is also influenced by the level of accuracy to which temperature, voltage, and transparency loss in the crystals due to radiation damage can be monitored.

The barrel section of the ECAL covers the region $|\eta| < 1.479$, with 61200 crystals of dimensions 22×22 mm^2 at the front face, 26×26 mm^2 at the rear face, and a length of 230 mm corresponding to 25.8 X_0. The endcap section has a front face cross section of 24.7×24.7 mm^2 with 220 mm long crystals. A preshower device covers the region $1.653 < |\eta| < 2.6$. It is made of two planes of silicon strips, placed behind disks of lead absorber at depths of $2X_0$ and $3X_0$. The aim of the preshower detector is to identify neutral pions in the endcap region, and also to help with the position determination of electrons and photons.

Hadron Calorimeter

The HCAL [63, 64] is built as a sampling calorimeter: absorber plates are interleaved with tiles of plastic scintillators; these tiles are piled-up into quasi-projective towers. The HCAL measures the amount and location of the deposited energy of jets, and is also a crucial component for evaluating missing transverse energy. The HCAL has been designed to cover a wide range of physics processes with different signatures in final states, particularly those involving hadronic jets, along with neutrinos or exotic particles resulting in apparent missing transverse energy. In order to have good jet four-momentum and missing transverse energy measurements, the HCAL must have good energy resolution, and provide good containment, transverse granularity, and hermeticity. An important condition for the HCAL is its location surrounding the ECAL and inside the magnet coil. The HCAL extends from a radius of 1.77 m to the inner surface of the magnet at a radius of 2.95 m. In order to absorb the hadronic shower, a brass absorber has been chosen because of its short interaction length. Moreover, this material is non-magnetic and suitable to be placed inside the magnetic field.

The hadron calorimeter barrel (HB) is a sampling calorimeter covering the range
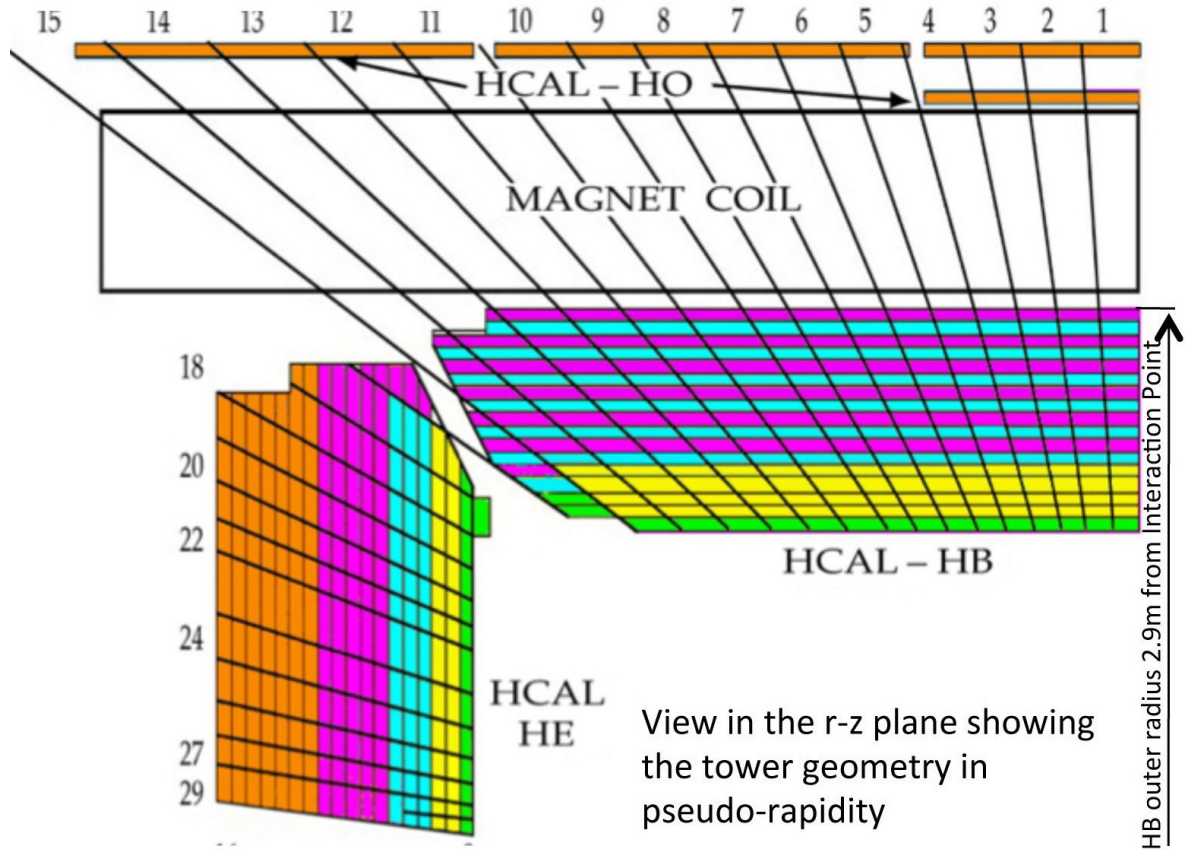
FIG. 3.6. Longitudinal view of the CMS hadronic calorimeter [65].

$|\eta| < 1.3$. It utilizes alternating layers of brass as an absorber and plastic scintillator as an active material, and consists of 36 identical azimuthal wedges, which form two half-barrels. The hadron calorimeter endcaps (HE) cover the range $1.3 < |\eta| < 3.0$. It has a construction of alternating brass and scintillator layers similar to HB. The structure is designed to minimise the cracks between the HB and HE rather than the single-particle energy resolution, since the resolution of jets in HE will be limited by pileup, magnetic field effects, and parton fragmentation.

3.2.5 Muon System

The muon system [63, 66, 67] has three functions: muon identification, momentum measurement, and triggering. The high-field solenoid magnet and its flux-return yoke enable good muon momentum resolution and triggering capability. The muon system, shown in Figure 3.7, consists of three different types of gaseous detectors: drift tube chambers (DT), cathode strip chambers (CSC), and resistive plate chambers (RPC).
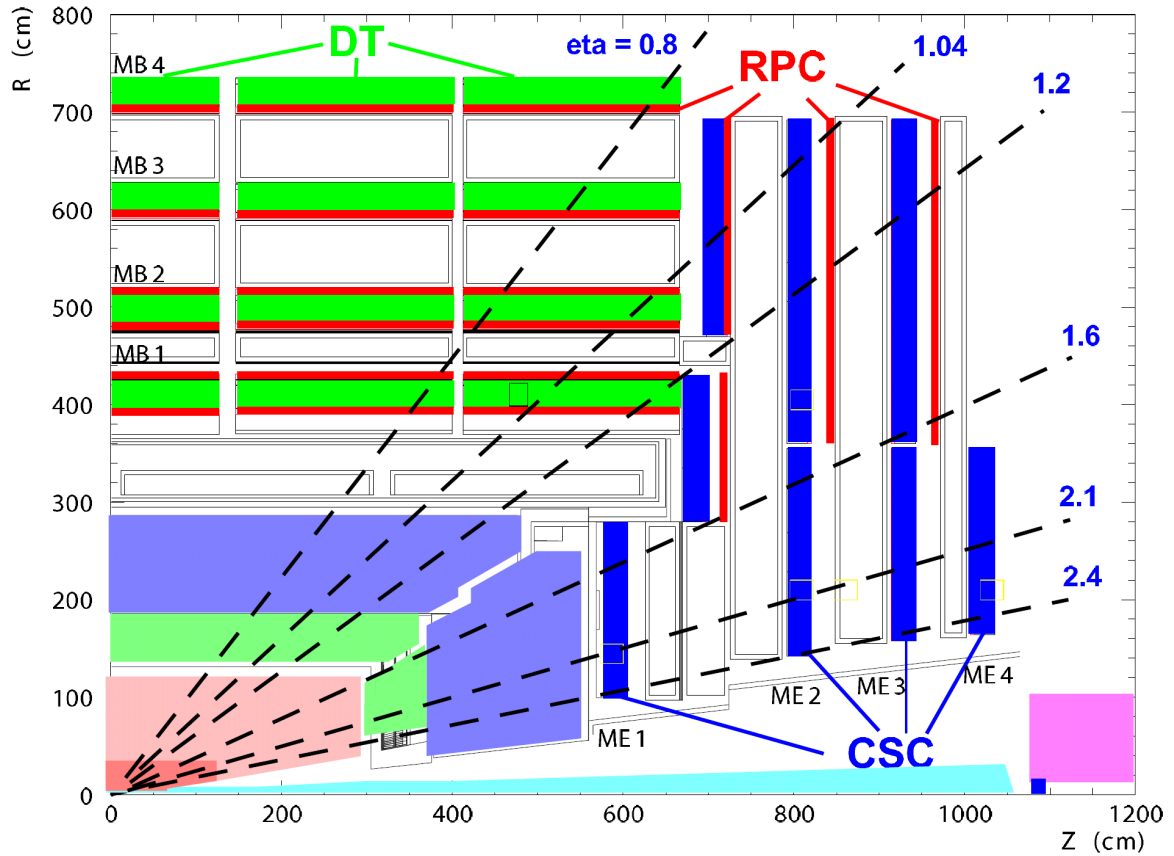
FIG. 3.7. Longitudinal view of the CMS muon system [66].

DTs are used in the barrel ($|\eta| < 1.2$), where the flux of the particles is low and the stray magnetic field is small. The drift cell (Figure 3.8) consists of a stainless steel anode wire placed between two parallel aluminium layers. The efficiency of a single chamber lies around 99.8%, with a spatial resolution of ~ 180 μm. A DT station consists of three superlayers of four stacked layers of drift tube chambers that are staggered to solve left-right track ambiguities. The track position of each DT is reconstructed by measuring the drift time of the avalanche electrons originating from the muon crossing.
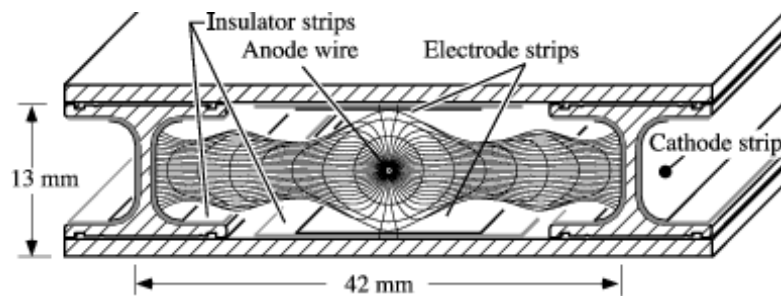
FIG. 3.8. Schematic view of a drift cell [66].
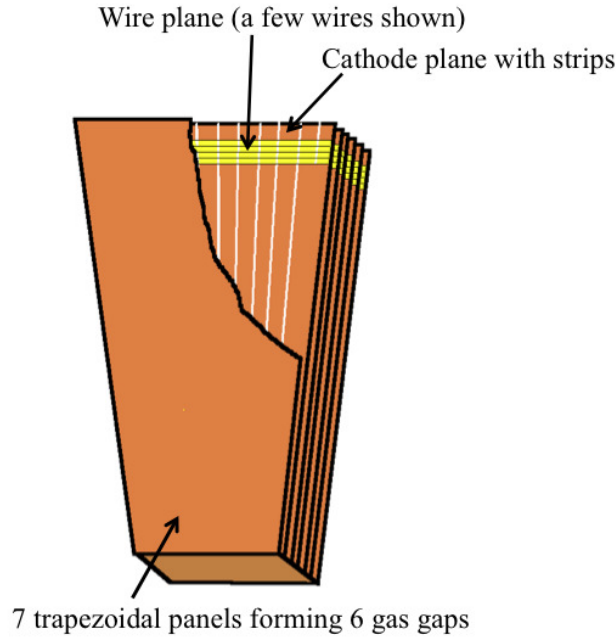
FIG. 3.9. Schematic view of the CSC [66].

The higher radiation environment in the endcaps requires the deployment of more robust detectors like CSCs. Each CSC consists of closely spaced anode wires stretched between two cathodes. The hit position is measured from the charge distribution induced by the avalanche on the cathode and by the hit wire itself. The endcap is divided into four stations of CSCs of trapezoidal shape, and is installed perpendicularly to the beam line. There are six gas gaps on each CSC (Figure 3.9).

The RPCs are deployed both in the barrel and in the endcaps, providing fast response with good time resolution, but coarser position resolution; the RPCs can unambiguously assign a muon to the correct bunch crossing. For this reason, a dedicated muon trigger is based on RPCs. The RPCs consist of two gaps formed by four bakelite electrodes covered by graphite in order to uniformly distribute the high voltage over the surface. Since the RPCs work in the avalanche mode, the gas gain is low and the signal has to be amplified by the readout electronics. Figure 3.10 shows a schematic view of an RPC.

3.2.6 Trigger

The trigger system provides the necessary rate reduction from the LHC bunch-crossing rate of 40 MHz to a rate of about 100 Hz, according to what is allowed by the limits on the
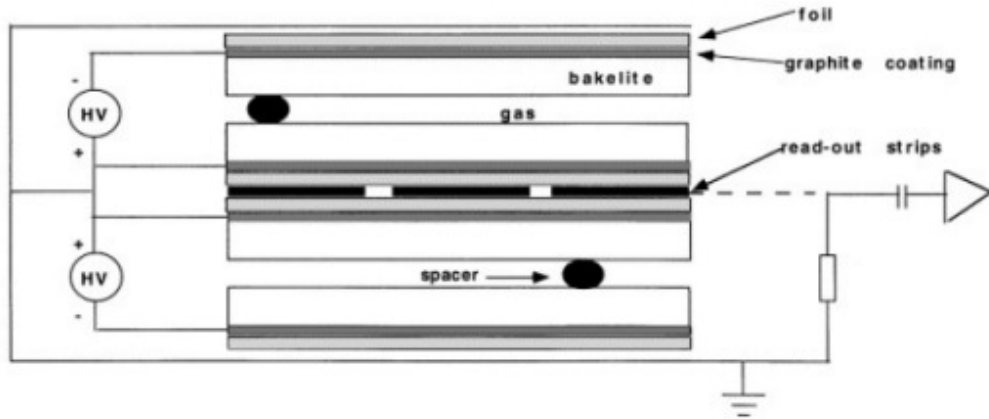
FIG. 3.10. Layout of the RPC double-gap structure [66].

storage capacity. This goal is achieved by the trigger system in two steps: the Level-1 (L1) trigger and the High-Level trigger (HLT). The L1 trigger consists of custom designed, largely programmable electronics, whereas the HLT is a software system implemented in a filter farm of about one thousand commercial processors. Data readout from the front-end electronics must reach the service cavern that houses the L1 trigger system that returns a signal back to the front-end electronics to provide a decision about taking or discarding the data from a particular bunch crossing. It takes about 3.2 μs to perform a decision.

The L1 trigger [68–70] maintains a high efficiency for interesting events while reducing the event rate to 100 KHz. The L1 trigger uses only the calorimeters (calorimeter trigger), the muon system (muon trigger), and a correlation among both systems (global trigger) as the time in which the trigger has to take a decision is too short to consider information from all raw data. The L1 trigger decisions are based on reconstruction of trigger primitives above some E_T and p_T thresholds. The triggered objects pass to the subsequent data acquisition system (DAQ) and HLT for further reconstruction and selection steps.

The HLT [71–73] uses more information and reconstruction algorithms than the L1 trigger to further reduce the event rate to about 100 Hz. The data coming from the readout buffers are transferred to processors, each running the HLT software code to produce a smaller output rate for mass storage. At a certain expense of robustness and

efficiency, isolation criteria can be used to reduce the trigger rates due to muons that are created from the decay of particles. HLT processing of a typical event involving tracking takes roughly 100 ms in the presence of an average value of ten pile-up events.

Chapter 4

Analysis Method

The analysis strategy of the contact interaction search is briefly explained with the method used to test the 2012 CMS data against the LLIM predictions along with the concept of signal and background predictions. The limit setting procedure is also discussed to determine the lower limits on compositeness energy scale Λ, as the 2012 CMS data is consistent with the SM predictions.

4.1 Selecting Sensitive Regions

Based on the experience gained through the contact interaction study performed using 2011 CMS data (at center of mass energy of 7 TeV), it is highly unlikely to observe a CI signal with Λ below 9 TeV. Therefore, the CI study for 2012 CMS data is performed beyond $\Lambda = 9$ TeV which is believed to be the maximum sensitive region for CI studies for the collision data at 8 TeV center of mass energy. Also the maximum sensitivity region for CI studies is the region of dimuon mass above 900 GeV since the previous studies at center of mass energy of 7 TeV have large event samples up to dimuon mass of 1500 GeV.

This CI analysis is carried out as a counting experiment with 100 GeV steps of dimuon mass ranging from 300 GeV to 2000 GeV chosen based on the knowledge of maximum sensitivity regions discussed above. The study incorporated with 2012 CMS data is explained in Section 6.1. The signal and background predictions in the context of LLIM are described in Section 5.1. In order to have better accuracy in the predictions, correction

factors, QCD K-factor and QED K-factor, are also evaluated as described in Sections 7.1.2 and 7.1.3.

4.2   Predictions of Signal and Background Events

The contact interaction signal is inseparable from the standard model DY and non-DY particle processes (irreducible backgrounds) which give dimuons in their final states. Therefore, the CI signal is evaluated as an enhancement of cross section to the known standard model DY and non-DY processes as described in Section 7.1. The strategy used to find the contact interaction signal is based on a comparison of the signal + background (CI/DY + non-DY) and the background (DY + non-DY) hypotheses.

The expected number of signal + background events is evaluated using

$$N_{CI/DY} = [CI/DY(\Lambda)] \times K_{QCD} \times K_{QED} + BKG_{\mu^+\mu^-}^{non-DY} \tag{4.1}$$

where $CI/DY(\Lambda)$ is the number of signal events reported by PYTHIA, K_{QCD} and K_{QED} are the QCD and QED K-factors, and $BKG_{\mu^+\mu^-}^{non-DY}$ is the number of dimuons coming from all the non-DY background sources.

Similarly, the expected number of background events (N_{SM}) is given by

$$N_{SM} = [DY(POWHEG)] \times K_{QED} + BKG_{\mu^+\mu^-}^{non-DY} \tag{4.2}$$

where $DY(POWHEG)$ is the number of DY events reported by POWHEG.

All the predictions are based on fully simulated (event generation and detector simulation) Monte Carlo samples using MC generators including PYTHIA, POWHEG, and MADGRAPH. The QCD and QED K-factors are utilized to bring the LO event yields to the level of NLO accuracy and a detailed description of correction factors is given in Section 7.1.1. The expected number of events under both hypotheses can then be tested against the observed number of events from 2012 CMS data at center of mass energy of 8 TeV to find possible new physics or to redefine the sensitive region for compositeness energy scale Λ.

4.3　Limit Setting on Λ

A consistency check is performed by evaluating the p value as described in Section 9.2 to find the level of agreement between the experimentally observed data and the background-only hypothesis (DY + non-DY).

If the data and background-only hypothesis are in good agreement (p value > 5 %), then lower limits on Λ are evaluated using the modified frequentist method as explained in Section 9.3.

Chapter 5

Monte Carlo Programs

Event simulation is a necessary part of high energy experiments as it permits experiments to model how signal and background processes would be reconstructed in the detector and thus allows a comparison with data and a means for either quantifying signals in discoveries or setting limits on signal cross sections.

5.1 Monte Carlo Event Generation

The structure of an event from an LHC collision is difficult to predict from first principles due to its extremely complex nature. Monte Carlo (MC) generators address this problem by dividing the whole process into more manageable sub-processes. Some of these sub-processes can be explained from first principles and others rely on appropriate high energy particle physics models with up-to-date parameters [74]. These MC event generators are key tools within almost all high energy particle physics experiments; they are used for simulating signal processes and their backgrounds. These MC generators are also essential to relate the experimentally measured variables with the theoretically established parameters that spur investigation.

Event generators simulate proton-proton collisions starting from basic particle interactions and predict the possible stable particles which can be captured by particle detectors [75]. This simulation process can be described with a few main steps: simulation of the hard process, the parton shower, hadronization, the underlying event, and

unstable particle decays, as shown in Figure 5.1.

Hard scattering is the maximum momentum transfer process in a proton-proton collision and its simulation starts from the center of the collision. This involves the Parton Distribution Functions (PDFs), which describes the incoming partons in lowest order perturbation theory and explains the probability distribution of incoming partons.

The parton shower addresses the behavior of incoming and outgoing partons after the hard collision. Evaluation of the particle shower starts from the hard scattering momentum scale and goes down to the lowest momentum scale until perturbation theory is no longer valid. Quarks and gluons are color−charged particles that interact by hard scattering. Similar to scattered electric charges which radiate photons, scattered colored charges radiate gluons when partons approach and leave the collision center. These emitted gluons are also colored and they can radiate by themselves creating an extended shower of soft gluons.

Hadronization is the process of forming hadrons from quarks after particle collisions. These hadrons are the final state particles which can be physically detected. The hadronization process is not fully understood and models have to be introduced to accurately explain the mechanism by which partons are confined to hadrons. The string model implemented in Pythia, and the cluster model implemented in Herwig, are the two main hadronization models currently available.

The spatial structure of a proton in its rest frame is spherical. However, in the lab frame, two protons move towards each other with velocities close to the speed of light and Lorentz contraction makes each proton into a thin disk. At the collision point, these two thin disks overlap each other and there is a large probability for interactions other than the hard scattering. This leads to the generation of an underlying event. The underlying event can have a large number of soft hadrons.

The contact interaction analysis utilizes several MC generators for different physical processes. The PYTHIA MC generator is used mainly for generating CI signal samples, DY samples, and diboson non−DY background samples. The POWHEG generator [76–78] is used to produce DY samples and some non−DY background samples. A non−DY
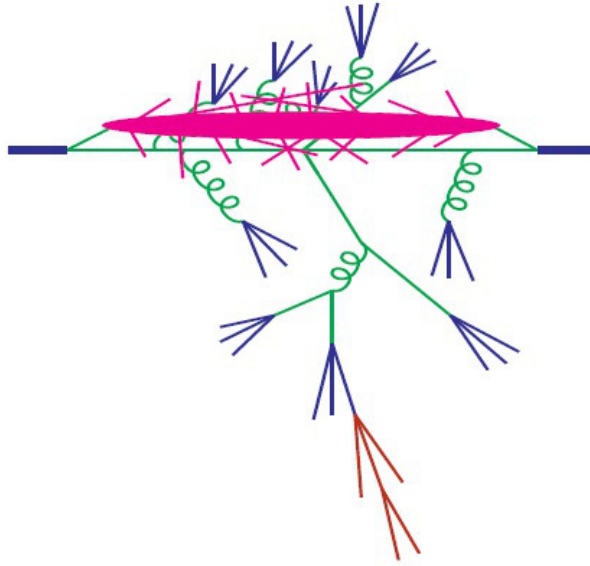
FIG. 5.1. The structure of a proton-proton collision, where the colors indicate: black-hard process, green-parton shower, indigo-hadronization, pink-underlying events, and brown-unstable particle decays [75].

background sample, W + jets, is produced using the MADGRAPH event generator. The HORACE generator is used to produce DY samples for QED $K-$factor analysis. The HERWIG generator is used to shower the hard events generated by MC@NLO in QCD $K-$factor calculations.

5.2 Monte Carlo Detector Simulation

Another use of MC generators in high energy physics is the simulation of particles traveling through detector components. Standard detector simulation programs provide tools to define the geometry of a detector using standard shapes. It also involves tracking the particles through the detector by considering all the appropriate physical processes: multiple scattering, interaction, decay, energy loss, and radiation [79]. The GEANT4 (GEometry ANd Tracking) object oriented simulation toolkit is used to fully simulate the CMS detector. This version is the successor of GEANT3 and was designed by the GEANT4 collaboration. The GENAT4 simulation software is highly powerful, robust, and maintainable and also capable of fulfilling emerging requirements of the CMS detector. It has

the following functionalities which are crucial in complex detector simulations [80].

1. Simple tools to define complex detector geometry and sensitive detector response.

2. Transporting particles through the geometry by considering boundary crossing under the influence of electric or magnetic fields.

3. Physics models for electromagnetic and hadronic interactions.

4. Alternative tools for Monte Carlo integration.

5. Visualization tools for geometries, tracks, and hits.

5.3 Compositeness Models

5.3.1 Helicity Conserving and Non-Conserving Compositeness Models in PYTHIA

A generator level quark and lepton compositeness study is carried out using the Monte Carlo event generator PYTHIA 6.4, which simulates contact interaction signal and composite Drell-Yan samples. There are mainly two compositeness models in the ISUB165 sub-process based on helicity: helicity conserving model (LLIM) and helicity non-conserving model (HNC). In this analysis the LLIM is used to study quark and lepton compositeness. Event generation can be done in five different scenarios in PYTHIA by simply changing the ITCM(5) card; all the other available compositeness options are listed in Table 5.1. The PYTHIA MC treats the LLIM as a $2 \to 1$ process by default, even though it treats SM DY production as a $2 \to 2$ process. To insure a consistent Q^2 scale in parton distributions, PYTHIA is forced to treat the LLIM as a $2 \to 2$ process by introducing the MSTP(32) = 4 card as recommended in the PYTHIA manual [81].

Cross sections reported by PYTHIA are analyzed for standard DY production using MSUB(1) and composite production (essentially infinite Λ) using ITCM(5)=0 after selecting MSTP(32) = 4. These cross sections are found to be identical within 0.4 % either in FSR ON or FSR OFF conditions that are available in PYTHIA. A comparison of event

yields for standard DY production and composite production are shown in Figure 5.2 for FSR turned OFF (Python code is provided in Appendix B).

Table 5.1. Compositeness models in PYTHIA.

Subprocess	ITCM5 Card	Model	Quark Compositeness
ISUB = 165	0	SMDY	None
	1	LLIM	u, d
	2	LLIM	u, d, c, s, t, b
	3	HNC	u
	4	HNC	u, c, t

This compositeness study is based only on the LLIM since this model is the benchmark model in the dimuon search. According to the model, all the initial state quarks are presumed to be composite objects by setting the $ITCM(5) = 2$, and the final state is chosen to be dimuon throughout the study. This represents the physics behind the first term of the Lagrangian in Equation 2.4 and there is a possibility of extending the analysis to the other terms in the Lagrangian. But this study is limited to the first term because the PDG limits are exclusively given for the LLIM model. The $RTCM(42)$ card sets the sign of η for constructive and destructive interference. A detailed description of technical information for event generation is given in Table 5.2.

Table 5.2. Technical details of event generation using PYTHIA.

Parameter	Value	Description
MSEL	0	turn OFF global process selection
MSUB(165)	1	turn ON $q + \bar{q} \rightarrow Z\gamma^* \rightarrow \mu^+\mu^-$
MSTP(32)	4	forces $2 \rightarrow 2$ (CI) to $2 \rightarrow 1$ process ($Z \rightarrow \mu\mu$)
RTCM(42)	-1 or 1	constructive or destructive interference
RTCM(41)	9	compositness energy scale Λ. Here it is 9000 GeV.
ITCM(5)	2	LLIM with all composite quarks
KFPR(165, 1)	13	final state with muon particles
CKIN(1)	300	lower cut off on mass in GeV. Here it is 300 GeV.
CKIN(2)	2000	upper cut off on mass in GeV. Here it is 2000 GeV.

ITCM5 Vs MSUB1 (FSR OFF) at 8 TeV 100K
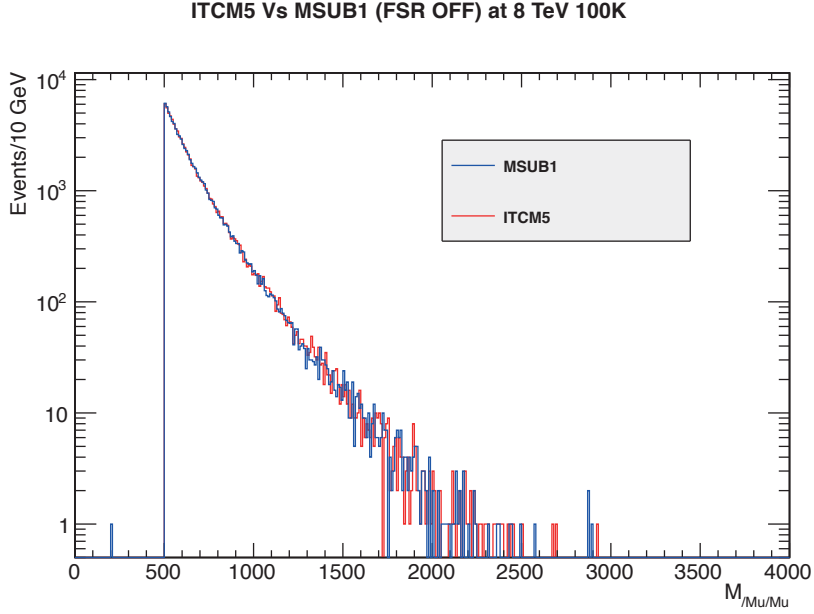
FIG. 5.2. Dimuon event yields for standard DY production through MSUB(1) and composite production through ITCM(5)=0.

5.3.2 The Left-Left Isoscalar Model in PYTHIA

The left-left isoscalar model (LLIM) of fermion compositeness in PYTHIA, which is the first term in the Lagrangian of Equation 2.4, is used to study the dimuon mass spectrum at generator level. Figures 5.3 (a) and (b) show dimuon event yields in the LLIM with different compositeness energy scales, Λ, ranging from 5 TeV to 17 TeV in constructive and destructive interference. The selection criteria are $p_T > 40$ GeV and $|\eta| < 2.1$ for both muons in the dimuon pairs, and the dimuon invariant mass threshold $M_{\mu\mu} > 120$ GeV. These criteria are used in order to select events in the signal region and within the geometrical acceptance of the CMS muon spectrometer.

Curves corresponding to different Λ values have less steeply falling cross sections than for DY production. When Λ increases, cross sections in each interference approach the DY limit as per Equation 2.5. It is also clear that the contact interaction is not visible below the Z^0 peak which justifies the dimuon invariant mass threshold requirement of 120 GeV. The terms "CI/DY" or "CI signal" will be used to refer to the process which contributes to the cross section in Equation 2.5 throughout this analysis. The dimuon angular distribution is another promising technique to study quark and lepton
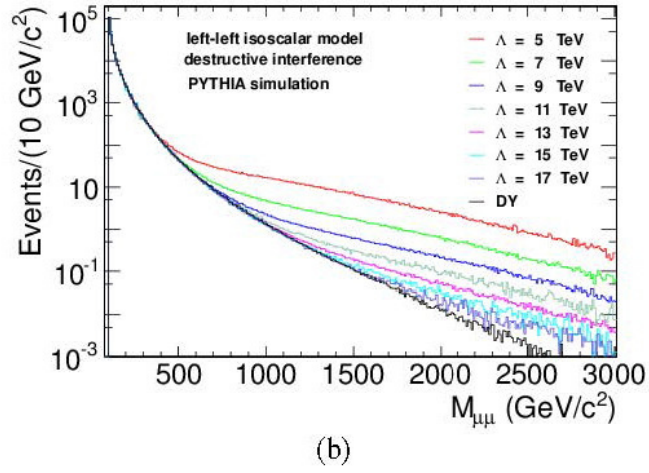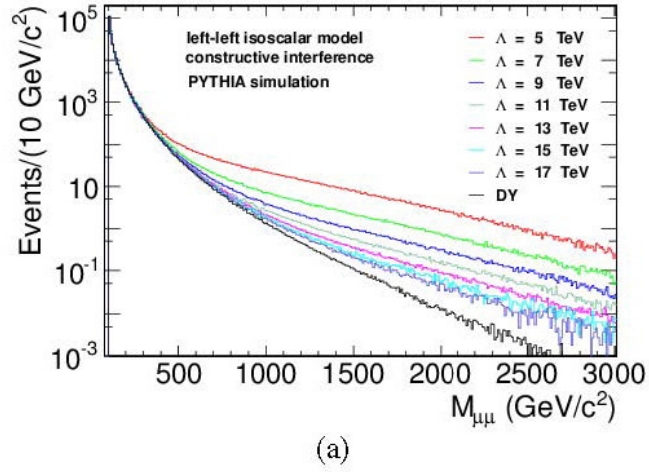
FIG. 5.3. Simulated dimuon mass spectra using the LLIM for (a) constructive interference and for (b) destructive interference [31].

compositeness as described in Appendix C.

Chapter 6

Data Set and Event Selection

Since the first proton-proton collision at 7 TeV center of mass energy in March 2010, the LHC has vastly improved the instantaneous luminosity. Over the course of the first three years of operation [82], the total integrated luminosity that was delivered by the LHC to the CMS detector reached nearly 30 fb^{-1}. A detailed description of delivered and recorded luminosity is given in Table 6.1.

Table 6.1. Integrated luminosity of pp collisions from 2010 to 2012 (LHC Run 1).

Year	Date Range	Collision Energy	LHC Delivered	CMS Recorded
2010	March - October	7 TeV	44.22 pb^{-1}	40.76 pb^{-1}
2011	March - October	7 TeV	6.13 fb^{-1}	5.55 fb^{-1}
2012	April - December	8 TeV	23.30 fb^{-1}	21.79 fb^{-1}

6.1 The 2012 CMS Data Set

A 1 TeV increase in collision energy by the LHC was achieved in 2012 after successfully recording pp collision data at 7 TeV center of mass energy during 2010 and 2011. The CMS detector began recording collision data from April 2012 to December 2012 at an upgraded center of mass energy of 8 TeV. As mentioned in Table 6.1, the LHC delivered a total of 23.3 fb^{-1} of pp collision data and CMS recorded a total of 21.79 fb^{-1} of collision data with a luminosity uncertainty of 2.6% as shown in Figure 6.1.

CMS Integrated Luminosity, pp, 2012, $\sqrt{s} = 8$ TeV
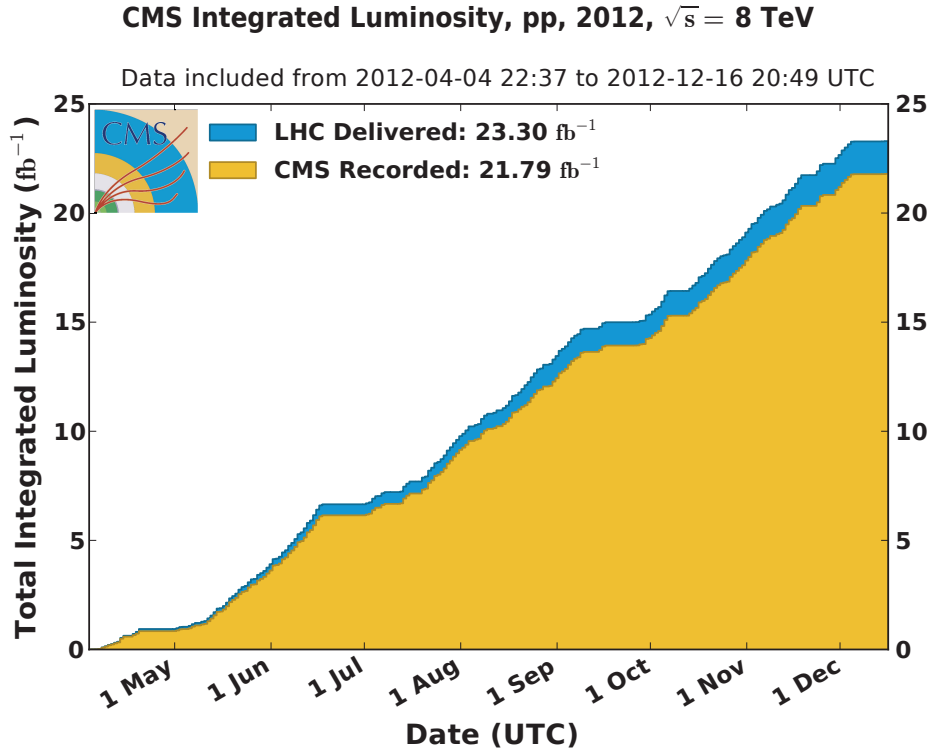
FIG. 6.1. Total integrated luminosity of *pp* collisions in 2012 [82].

The period over which data were recorded in 2012 is separated into four different sections based on the instantaneous luminosity. These are named 2012A, 2012B, 2012C, and 2012D [83]. The contact interaction analysis is based on the full 2012 CMS dataset with appropriate triggers at collision energy of 8 TeV which corresponds to 20.6 fb^{-1}. This analysis utilizes the single muon trigger, HLT_Mu40_eta2p1, which requires a muon with $p_T > 40$ GeV and $|\eta| < 2.1$. The datasets are reconstructed with CMSSW_5_3_X and a detailed description of the datasets used in this analysis is presented in Table 6.2 .

Table 6.2. Datasets [31].

Data Set	Run Range	Luminosity (fb^{-1})
/SingleMu/Run2012A-13Jul2012-v1/AOD	$190456 - 193621$	0.85
/SingleMu/Run2012A-recover-06Aug2012-v1/AOD	$190782 - 190949$	0.08
/SingleMu/Run2012B-13Jul2012-v1/AOD	$193833 - 196531$	4.83
/SingleMu/Run2012C-24Aug2012-v1/AOD	$198022 - 198913$	0.50
/SingleMu/Run2012C-PromptReco-v2/AOD	$198934 - 203746$	6.80
/SingleMu/Run2012D-PromptReco-v1/AOD	$203768 - 208686$	7.57

Even though the CMS detector performed remarkably well during 2012, some of the sub-detectors were not always fully functional. Therefore it is necessary to certify the quality of all CMS data prior to any physics analysis. All the runs and the luminosity sections which are used in this anlaysis are selected based on the official JSON files provided by the data certification group, presented in Table 6.3 .

Table 6.3. JSON files [31].

No	JSON files for Dimuons
1	Cert 190456-196531 8TeV 13Jul2012ReReco Collisions12 JSON MuonPhys v3.txt
2	Cert 190782-190949 8TeV 06Aug2012ReReco Collisions12 JSON MuonPhys.txt
3	Cert 190456-196531 8TeV 13Jul2012ReReco Collisions12 JSON MuonPhys v4.txt
4	Cert 198022-198523 8TeV 24Aug2012ReReco Collisions12 JSON MuonPhys.txt
5	Cert 190456-203002 8TeV PromptReco Collisions12 JSON MuonPhys v2.txt
6	Cert 190456-208686 8TeV PromptReco Collisions12 JSON MuonPhys.txt

6.2   Trigger Requirements in 2012

The lowest p_T threshold unprescaled single-muon trigger is used to select events for this analysis with the Level-1 (L1) and High Level Trigger (HLT). This trigger selection simplifies the analysis with respect to using a dimuon trigger. The HLT trigger path for the 2012 run period is HLT_Mu40_eta2p1, which requires at least one muon with $p_T > 40$ GeV; the acceptance of the trigger is restricted to $|\eta| < 2.1$.

The combined L1 and HLT trigger efficiency is shown in Figure 6.2 as a function of dimuon invariant mass. The predicted total trigger effiency is about 97% for the dimuon mass range of interest and the efficiency in 2012 is approximately 2% lower than that from 2011. A detailed comparison of performance between these two years is given in Figure 6.3. One possible explanation for this slight drop might be that, at L1, the CSCTF changed its p_T assignment algorithms and for the HLT, new cuts were implemented to reduce contamination from mismeasured low p_T muons [84].

The CMS Muon Physics Object Group (MPOG) has measured the single-muon trigger effiencies in the data. The effciencies are determined by applying the "Tag and Probe"
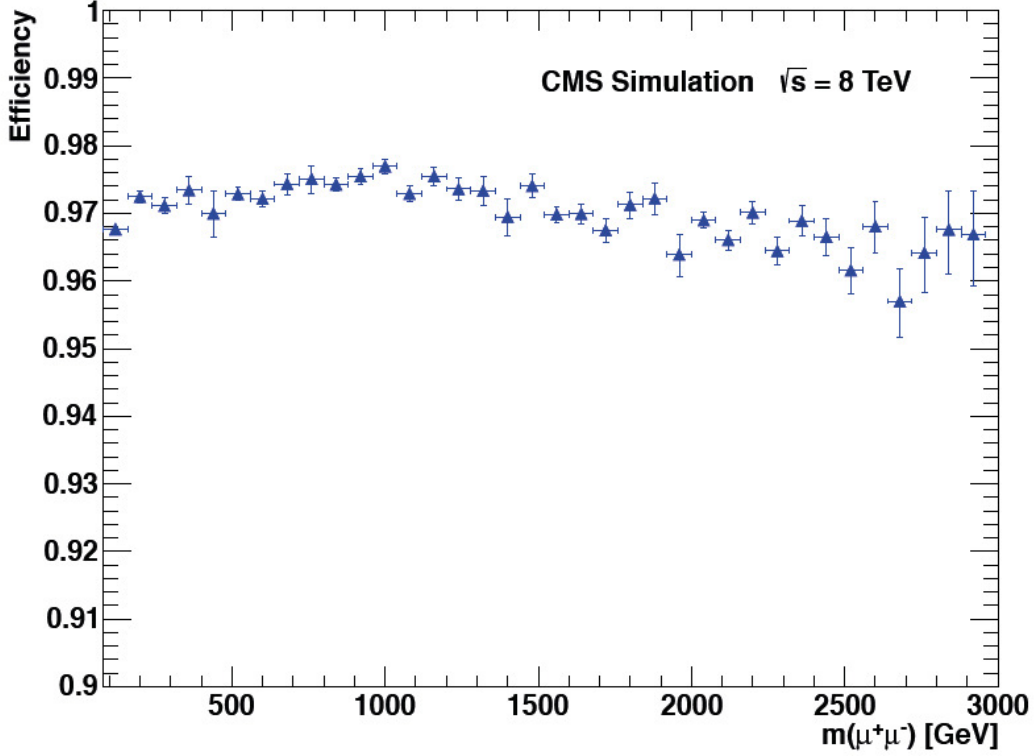
FIG. 6.2. The efficiency of the single muon trigger path as a function of dimuon invariant mass [85].

technique [67] to muons from Z decays, and then comparing these with MC predictions. The trigger efficiencies are evaluated with respect to muons reconstructed offline and passing through a very similar selection criteria to that given in Section 6.3. The overall efficiency of the single-muon trigger used in this analysis is about 94.1 % for $|\eta| < 0.9$, 84.3 % for $0.9 < |\eta| < 1.2$, and 82.7% for $1.2 < |\eta| < 2.1$ [85].

6.3 Event Selection

The MPOG high p_T criteria are followed for selection of events, individual muons, and dimuon pairs. The exact same selection criteria are imposed on the data and in Monte Carlo simulation studies. The selection criteria for the generator level studies is chosen less restrictively and each muon is required to have $p_T > 40$ GeV/c and $|\eta| < 2.6$.

Reconstruction cuts for baseline selection of events

1. Events are filtered by requiring that at least 25% of the tracks in the silicon tracker are marked as high purity [86] in order to avoid events which are coming from beam
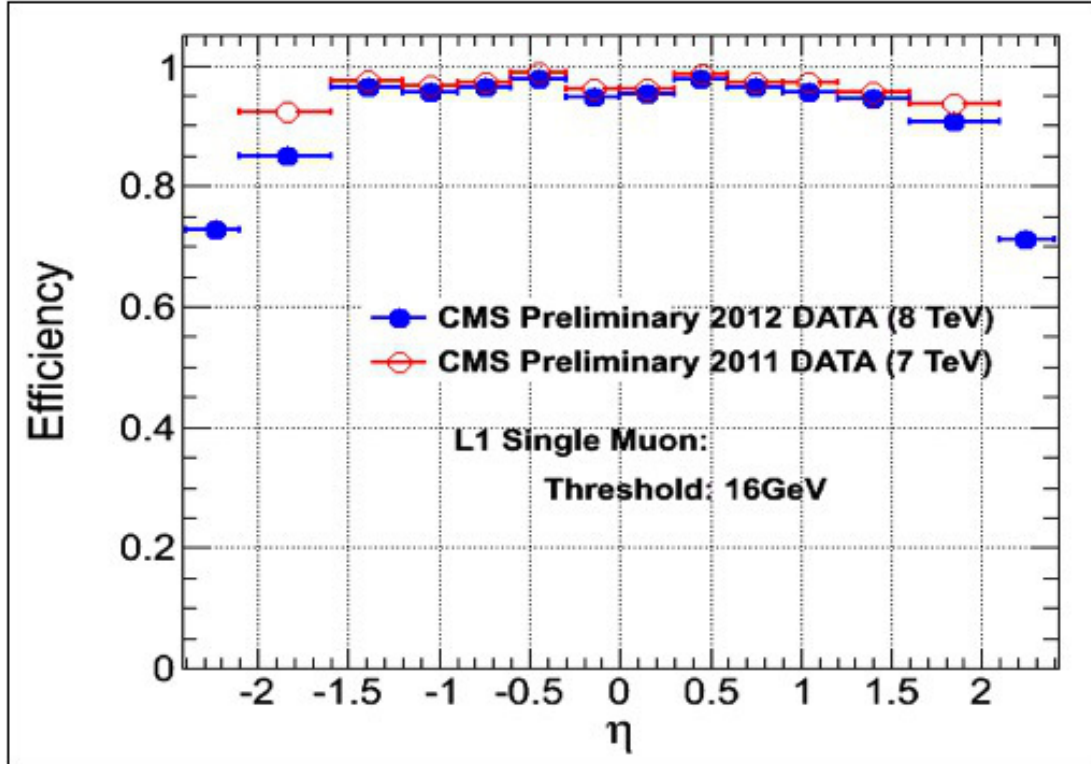
FIG. 6.3. L1SingleMu16 trigger efficiency in 2011 and 2012 [84].

backgrounds.

2. Events are required to have at least one good offline reconstructed primary vertex to reject cosmic ray muons triggered in empty bunch-crossings which can produce fake dimuons when traversing the detector close to the interaction point. As defined by the tracking POG, a primary vertex is considered good if it is associated with at least four tracks and the vertex must be located within $|r| < 2$ cm and $|z| < 24$ cm of the nominal interaction point.

Reconstruction cuts for individual muons

1. The muon candidate is required to be reconstructed as a global and a track muon [67].

2. The muon candidate must have at least 45 GeV of p_T as reconstructed offline.

3. The global muon track must have at least six valid tracker layers with hits.

4. The global muon track must include at least one valid tracker pixel hit.

5. The tracker muon must be matched to segments in at least two muon stations.

6. The muon's transverse impact parameter with respect to the beam spot must be less than 0.2 cm.

7. The relative p_T error, $\delta p_T/p_T$, must be less than 0.3 to suppress any grossly misreconstructed muons.

8. A tracker based isolation cut is implemented to suppress muons coming from hadronic decays requiring that Σp_T of all other tracks in a cone of $\Delta R = \sqrt{(\Delta\eta)^2 + (\Delta\phi)^2} <$ 0.3 (excluding the muon's tracker track) should be less than 10% of the muon's p_T.

Dimuon selection criteria

1. Both muons must be oppositely charged.

2. To suppress cosmic ray muons travelling close to the interaction point, the 3 - - dimensional opening angle between the two muons must be less than $\pi - 0.02$ radians.

3. To ensure that the two muons originate from a common vertex, the vertex fit is required to have $\chi^2/$ d.o.f < 10.

Events that have more than two reconstructed muons passing all the above requirements are very rare. The two highest p_T muons are selected if an event has three or more reconstructed muons and these two muons must be oppositely charged to retain the event. There are 62 dimuon pairs which have masses above 900 GeV and 38 events which exceed a dimuon mass of 1 TeV. A description of only the highest 20 dimuon events is given in Table 6.4 and the event displays for the two highest mass events are shown in Figure 6.4. The complete description of all 62 dimuon events above mass 900 GeV is given in Appendix A.
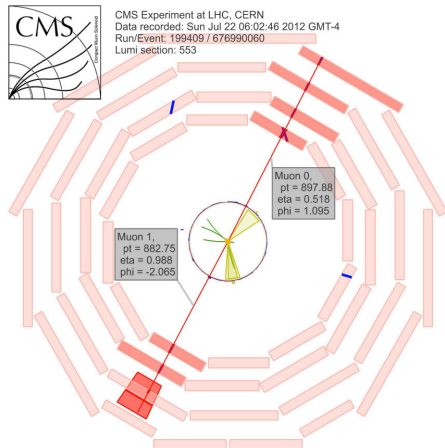
(a) Transverse view of 1824 GeV dimuon event
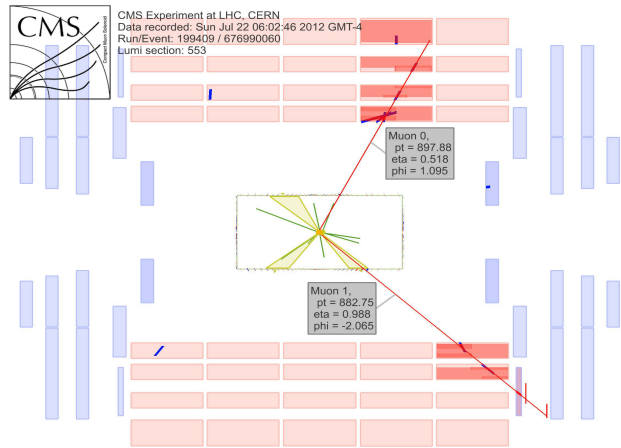
(b) Longitudinal view of 1824 GeV dimuon event
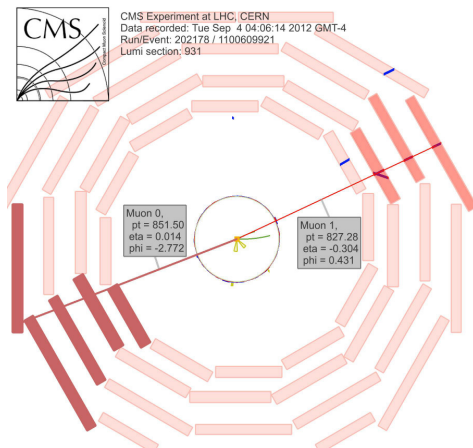
(c) Transverse view of 1697 GeV dimuon event
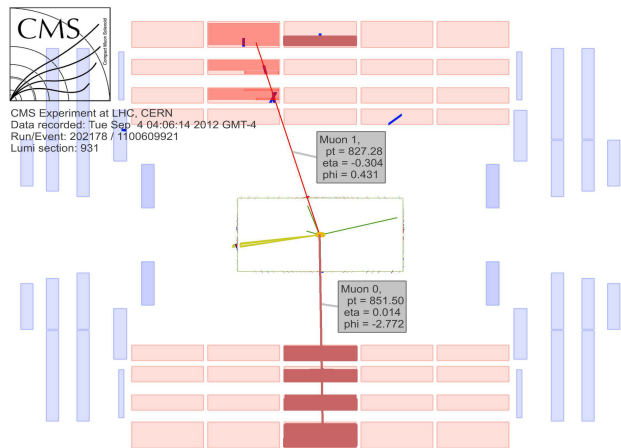
(d) Longitudinal view of 1697 GeV dimuon event

(a)

FIG. 6.4. Event display of the two highest mass dimuons [85].

Table 6.4. High mass dimuon events [31].

No	Lumi-Section	Run No	Event No	$M_{\mu\mu}$ (GeV)
1	553	199409	676990060	1824
2	931	202178	1100609921	1697
3	398	205694	416479300	1694
4	153	206207	186909124	1592
5	215	207924	209747123	1486
6	193	195378	225870452	1453
7	531	199409	654043540	1367
8	1215	204601	1278017291	1357
9	77	196433	39187003	1327
10	1054	199833	1136357968	1325
11	995	194050	936530164	1322
12	541	199812	636694094	1319
13	90	196431	66057632	1290
14	666	208391	845554877	1248
15	78	207492	65524201	1232
16	641	198969	779619791	1212
17	323	202087	421813187	1192
18	368	204563	499818262	1188
19	444	194912	739866334	1168
20	97	199571	109753290	1166

6.4   Pileup Effect

High luminosity stable beams are crucial for the success of the LHC physics program since it involves creating more collisions which in turn leads to the observation of rare particle phenomena. The increased luminosity of the proton beam also increases the probability of multiple pp interactions within a single bunch crossing, which is referred to as a pileup effect. Simply, this pileup effect is a by product of the improvement of the luminosity in proton beams which can decrease signal efficiency from isolation requirements (muons are required to be isolated according to our selection criteria). The CMS pileup distribution for 2012 is shown in Figure 6.5 [87].

The challenge is to accurately assign data to correct pp interactions since the pileup effect requires the reconstruction of more charged tracks and is also associated with greater energy deposition in calorimeters for each primary interaction. As mentioned in
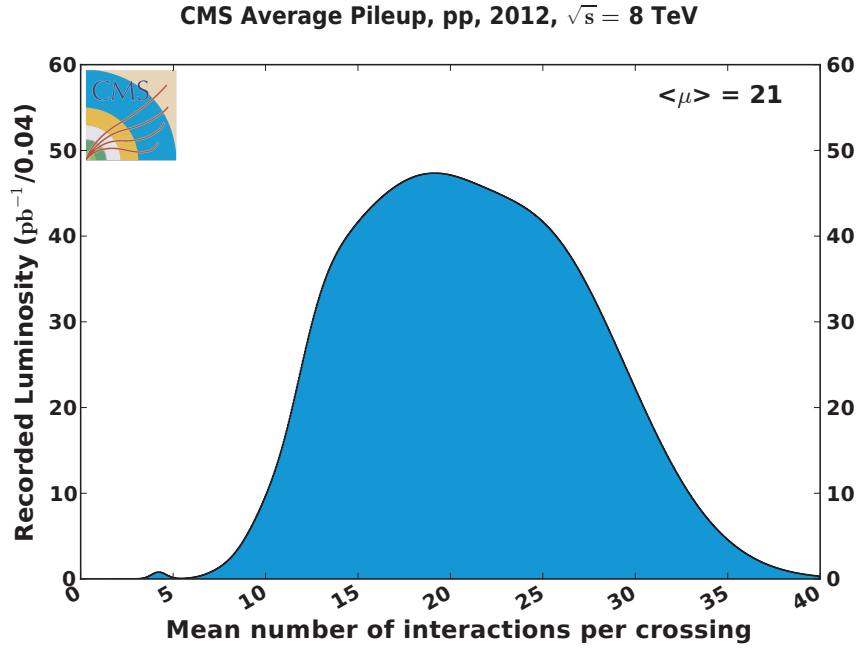
FIG. 6.5. The CMS pileup distribution in 2012 [87] .

Section 6.3 (reconstruction cuts for individual muons), our muon isolation requirement is a loose one. Therefore, the dependence of tracker isolation on the pileup effect is lowered by considering only charged tracks which originate within $\Delta z = 0.2$ cm of the primary vertex when calculating Σp_T. Because of this, tracker only isolation makes the analysis intrinsically more efficient with pileup effects as shown in Figure 6.6.
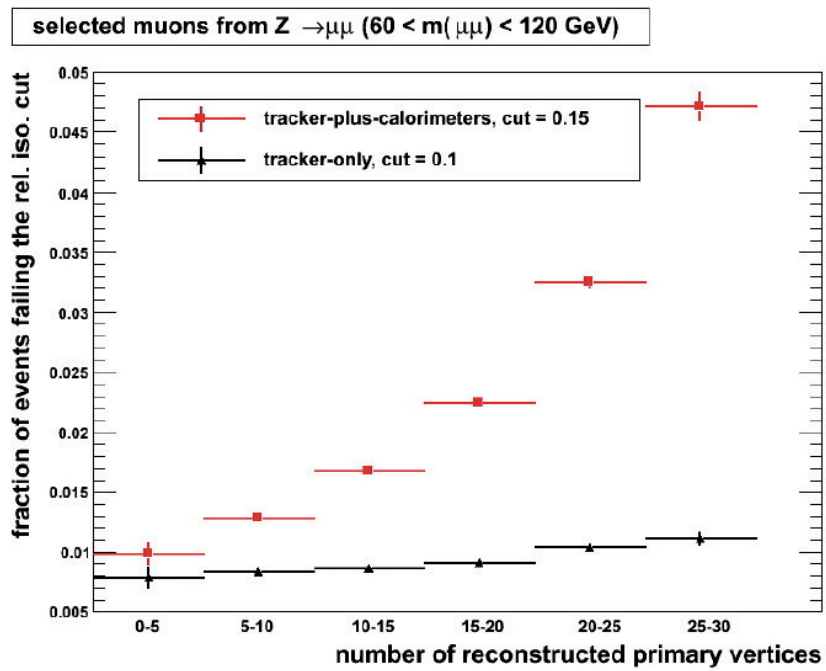
FIG. 6.6. Considering dimuons in the Z peak ($60 < M_{\mu\mu} < 120$ GeV/c^2) in the data, the fraction of muons that fail a cut on tracker$-$only and tracker$-$plus$-$calorimeters relative isolation variables at thresholds of 0.1 and 0.15, respectively, as a function of the number of reconstructed primary vertices [88].

Chapter 7

Full Simulation of Signal and Background Events

The observed dimuon mass spectrum is compared with the theoretically determined dimuon mass spectrum to find any deviation from the standard model which yields evidence of quark and lepton compositeness. Therefore, it is a crucial part in this analysis to predict the expected dimuon mass spectrum from contact interactions and from standard model sources. The predictions of expected events for CI/DY (CI signal), DY, and non-DY processes are performed using a series of Monte Carlo generators followed by full detector simulation.

7.1 Simulation of Expected Signal

The CI signal samples are generated in the context of the LLIM using the Monte Carlo event generator PYTHIA version 6.4 and the detector simulation toolkit GEANT4 under CMSSW_5_3_2_patch4. As described in Section 5.3, the LLIM is implemented in PYTHIA with subprocess parameter ISUB = 165 for constructive and destructive interference. A detailed description of the other PYTHIA parameters used for CI signal sample generation, such as MSEL, MSUB(165), ITCM(5), MSTP(32), RTCM(41), RTCM(42), CKIN(1), CKIN(2), and KFPR(165, 1) is given in Section 5.3. The CTEQ6L1 parton distribution functions [89] are used by PYTHIA for incident protons and the V19E baseline

alignment scenario is used for detector simulations.

Generator level kinematic cuts are applied to each muon in the dimuon pair ($p_T >$ 40 GeV and $|\eta| < 2.6$) using standard PYTHIA filters. The CI signal samples are generated with different minimum mass cuts ($M_{\mu\mu}^{min}$) and different Λ values for constructive and destructive interference as shown in Table 7.1. Λ is chosen based on expectations for the 95% confidence level limits and different $M_{\mu\mu}^{min}$ values are used to obtain maximum statistical precision over the mass range in this analysis. Standard DY samples are also produced using POWHEG to validate the behavior of the CI signal implementation in the limit where the compositeness energy scale $\Lambda \to \infty$. The $M_{\mu\mu}^{min} = 300$ GeV sample is used to predict event yields in the mass range 300 GeV < M < 600 GeV, the $M_{\mu\mu}^{min}= 500$ sample is used for the mass range 600 GeV < M < 1000 GeV, and the $M_{\mu\mu}^{min}= 800$ GeV sample is used for the mass range M > 1000 GeV. The file names of all 33 signal samples used in this analysis are listed in Table 7.2.

The expected number of signal events ($N_{CI/DY}$) is the product of the fully simulated number of CI signal events (CI/DY), QCD K-factor, QED K-factor, and summed with the event contributions from all the non-DY background sources as given by Equation 4.1. Also the expected number of background events (N_{SM}) is given by Equation 4.2.

7.1.1 K-factors

The PYTHIA Monte Carlo event generator is used to produce fully simulated CI signal samples since it is the only generator which incorporates the quark and lepton compositeness model LLIM. The PYTHIA MC is a leading order (LO) event generator; incorporating only LO processes can underestimate the cross sections by a factor of two or more at high energy collider experiments [90]. Therefore it is important to consider all possible higher order terms up to next-to-leading order (NLO) or next-to-next-to-leading-order (NNLO) to obtain the maximum possible accuracy. There are two major types of higher order corrections needed for this compositeness study. The first, the NLO QCD correction, involves strong interactions and the second, the NLO QED correction, involves

Table 7.1. Details of CI signal samples simulated using PYTHIA [31].

		$\mathrm{M}_{\mu\mu}^{\min}$ (GeV)					
		300	500	800	300	500	800
Λ (TeV)	η	Events			σ (pb)		
∞		50970	24832	25343	0.2619	0.03549	0.004512
19	-1	49758	24931	25154	0.2676	0.03817	0.005514
17		49647	25528	24659	0.2697	0.03913	0.005868
15		49943	24997	25714	0.2720	0.04031	0.006455
13		48959	25099	14312	0.2779	0.04288	0.007523
11		52138	23564	26822	0.2847	0.04717	0.009625
9		49833	25281	25052	0.3026	0.05680	0.014540
15	+1	49444	25890	25040	0.2565	0.03391	0.004429
13		50248	24100	24990	0.2543	0.03399	0.004776
11		50532	25531	24955	0.2539	0.03531	0.005811
9		49393	25620	25167	0.2559	0.03910	0.008847

electroweak interactions. Therefore, two K-factors are used to improve the accuracy of PYTHIA generated CI signal samples and compostiness DY samples. The K-factor is defined as the cross section calculated up to NLO divided by the cross section calculated up to LO, as shown in Equation 7.1.

$$\text{K-factor} = \frac{\sigma_{NLO}}{\sigma_{LO}}. \tag{7.1}$$

7.1.2 QCD K-factor

A QCD K-factor of 1.3 (QCD higher order correction) is used to boost the event yields which are simulated using the PYTHIA LO generator. This mass independent constant value for the QCD higher order correction is consistent with the method in Ref. [88]. Figure 7.1 explains the QCD K-factor dependence on the dimuon mass for different PDF sets and justifies the choice of 1.3 in the calculation. There is also a flat correction factor of 1.024 [88] chosen to improve the Monte Carlo predictions from the NLO level to the level of NNLO as a result of a study done using FEWZ [91].

The QCD K-factor is determined by generating standard DY samples at the gen-

Table 7.2. File names of signal samples [31].

No	Sample Name
1	CIToMuMu_ITCM5_M-300_TuneZ2star_8TeV-pythia6/Summer12_DR53X-PU_S10_START53_V19E-v1/AODSIM
2	CIToMuMu_ITCM5_M-500_TuneZ2star_8TeV-pythia6/Summer12_DR53X-PU_S10_START53_V19E-v1/AODSIM
3	CIToMuMu_ITCM5_M-800_TuneZ2star_8TeV-pythia6/Summer12_DR53X-PU_S10_START53_V19E-v1/AODSIM
4	CIToMuMu_Con_Lambda-9_M-300_TuneZ2star_8TeV-pythia6/Summer12_DR53X-PU_S10_START53_V19E-v1/AODSIM
5	CIToMuMu_Con_Lambda-9_M-500_TuneZ2star_8TeV-pythia6/Summer12_DR53X-PU_S10_START53_V19E-v1/AODSIM
6	CIToMuMu_Con_Lambda-9_M-800_TuneZ2star_8TeV-pythia6/Summer12_DR53X-PU_S10_START53_V19E-v1/AODSIM
7	CIToMuMu_Con_Lambda-11_M-300_TuneZ2star_8TeV-pythia6/Summer12_DR53X-PU_S10_START53_V19E-v1/AODSIM
8	CIToMuMu_Con_Lambda-11_M-500_TuneZ2star_8TeV-pythia6/Summer12_DR53X-PU_S10_START53_V19E-v1/AODSIM
9	CIToMuMu_Con_Lambda-11_M-800_TuneZ2star_8TeV-pythia6/Summer12_DR53X-PU_S10_START53_V19E-v1/AODSIM
10	CIToMuMu_Con_Lambda-13_M-300_TuneZ2star_8TeV-pythia6/Summer12_DR53X-PU_S10_START53_V19E-v1/AODSIM
11	CIToMuMu_Con_Lambda-13_M-500_TuneZ2star_8TeV-pythia6/Summer12_DR53X-PU_S10_START53_V19E-v1/AODSIM
12	CIToMuMu_Con_Lambda-13_M-800_TuneZ2star_8TeV-pythia6/Summer12_DR53X-PU_S10_START53_V19E-v1/AODSIM
13	CIToMuMu_Con_Lambda-15_M-300_TuneZ2star_8TeV-pythia6/Summer12_DR53X-PU_S10_START53_V19E-v1/AODSIM
14	CIToMuMu_Con_Lambda-15_M-500_TuneZ2star_8TeV-pythia6/Summer12_DR53X-PU_S10_START53_V19E-v1/AODSIM
15	CIToMuMu_Con_Lambda-15_M-800_TuneZ2star_8TeV-pythia6/Summer12_DR53X-PU_S10_START53_V19E-v1/AODSIM
16	CIToMuMu_Con_Lambda-17_M-300_TuneZ2star_8TeV-pythia6/Summer12_DR53X-PU_S10_START53_V19E-v1/AODSIM
17	CIToMuMu_Con_Lambda-17_M-500_TuneZ2star_8TeV-pythia6/Summer12_DR53X-PU_S10_START53_V19E-v1/AODSIM
18	CIToMuMu_Con_Lambda-17_M-800_TuneZ2star_8TeV-pythia6/Summer12_DR53X-PU_S10_START53_V19E-v1/AODSIM
19	CIToMuMu_Con_Lambda-19_M-300_TuneZ2star_8TeV-pythia6/Summer12_DR53X-PU_S10_START53_V19E-v1/AODSIM
20	CIToMuMu_Con_Lambda-19_M-500_TuneZ2star_8TeV-pythia6/Summer12_DR53X-PU_S10_START53_V19E-v1/AODSIM
21	CIToMuMu_Con_Lambda-19_M-800_TuneZ2star_8TeV-pythia6/Summer12_DR53X-PU_S10_START53_V19E-v1/AODSIM
22	CIToMuMu_Des_Lambda-9_M-300_TuneZ2star_8TeV-pythia6/Summer12_DR53X-PU_S10_START53_V19E-v1/AODSIM
23	CIToMuMu_Des_Lambda-9_M-500_TuneZ2star_8TeV-pythia6/Summer12_DR53X-PU_S10_START53_V19E-v1/AODSIM
24	CIToMuMu_Des_Lambda-9_M-800_TuneZ2star_8TeV-pythia6/Summer12_DR53X-PU_S10_START53_V19E-v1/AODSIM
25	CIToMuMu_Des_Lambda-11_M-300_TuneZ2star_8TeV-pythia6/Summer12_DR53X-PU_S10_START53_V19E-v1/AODSIM
26	CIToMuMu_Des_Lambda-11_M-500_TuneZ2star_8TeV-pythia6/Summer12_DR53X-PU_S10_START53_V19E-v1/AODSIM
27	CIToMuMu_Des_Lambda-11_M-800_TuneZ2star_8TeV-pythia6/Summer12_DR53X-PU_S10_START53_V19E-v1/AODSIM
28	CIToMuMu_Des_Lambda-13_M-300_TuneZ2star_8TeV-pythia6/Summer12_DR53X-PU_S10_START53_V19E-v1/AODSIM
29	CIToMuMu_Des_Lambda-13_M-500_TuneZ2star_8TeV-pythia6/Summer12_DR53X-PU_S10_START53_V19E-v1/AODSIM
30	CIToMuMu_Des_Lambda-13_M-800_TuneZ2star_8TeV-pythia6/Summer12_DR53X-PU_S10_START53_V19E-v1/AODSIM
31	CIToMuMu_Des_Lambda-15_M-300_TuneZ2star_8TeV-pythia6/Summer12_DR53X-PU_S10_START53_V19E-v1/AODSIM
32	CIToMuMu_Des_Lambda-15_M-500_TuneZ2star_8TeV-pythia6/Summer12_DR53X-PU_S10_START53_V19E-v1/AODSIM
33	CIToMuMu_Des_Lambda-15_M-800_TuneZ2star_8TeV-pythia6/Summer12_DR53X-PU_S10_START53_V19E-v1/AODSIM

erator level using Monte Carlo event generators MC@NLO 3.4 [92] with HERWIG 6 [93] and PYTHIA. The NLO generator MC@NLO is used for hard event generation and HER-WIG for showering and hadronization of the hard events produced by MC@NLO. The samples are generated for the dimuon mass thresholds starting from 200 GeV to 2000 GeV in step sizes of 100 GeV and subjected to the transverse momentum cut $p_T > 45$ GeV for each muon, $|\eta| < 2.1$ for the first muon, and $|\eta| < 2.4$ for the second muon. A total of 36 samples (18 samples by MC@NLO and an additional 18 by PYTHIA) are generated having 200000 events at 8 TeV center of mass energy. All the samples are generated after turning off QED final state radiation in PYTHIA by using MSTJ(41)=1 for
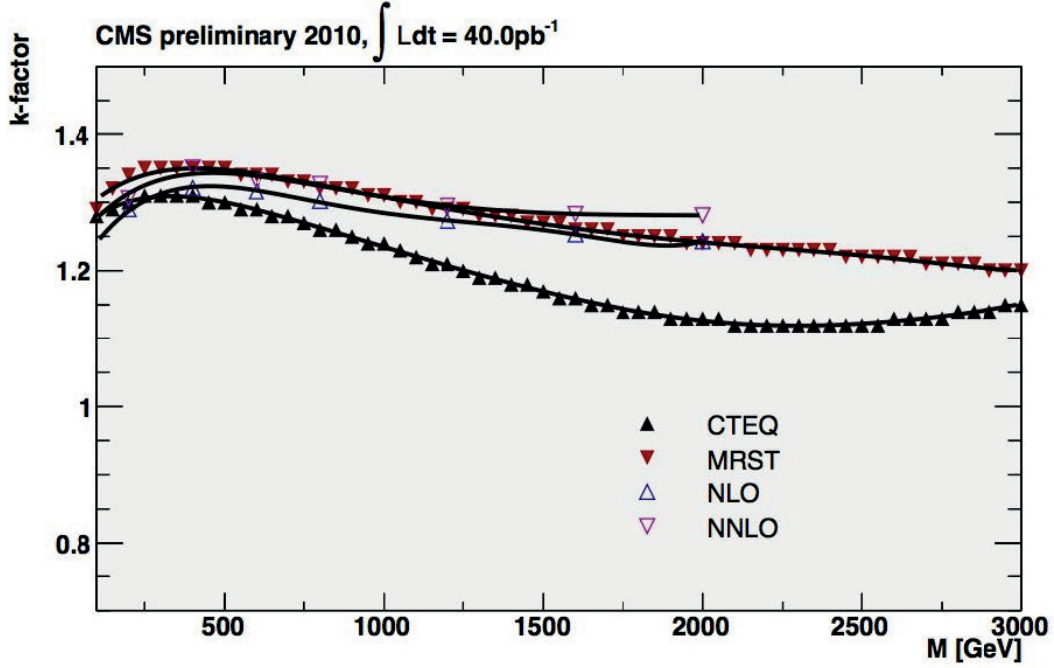
FIG. 7.1. The QCD K-factor dependence on dimuon mass for different PDF sets [95].

consistency with HERWIG. After passing all the filters the events which survive in each dimuon mass bin are calculated for bins with mass thresholds starting at 200 GeV and normalized to the number of events in the 200 GeV bin using MC@NLO. To determine the QCD K-factor, the total number of dimuon events are considered above a particular mass threshold after passing all the cuts rather than considering the full cross section. The QCD K-factors determined for DY production are always above one, varying from 1.26 to 1.31, and contributing to an enhancement of overall cross section. But, if a more current NLO PDF set than the CTEQ6M PDF set is used, one will get QCD K-factors that show less variation with mass and are closer to 1.3.

7.1.3 QED K-factor

Another correction factor that is determined to improve the leading order Monte Carlo predictions is the QED K-factor. It is used because the electroweak NLO calculations involve non negligible corrections to the DY cross section in the high mass region. The QED K-factor is determined using the HORACE 3.1 event generator [94] and it is always calculated with respect to the POWHEG NLO QCD cross section. This factor is weakly mass dependent as explained by Equation 7.2 and always less than one, which leads to

a decrease in the overall cross section. The effect of the QED K-factor increases with dimuon mass. A detailed description of systematic uncertainties from the QED K-factor is given in Chapter 7.

$$\text{QED K-factor} = 1.01 - 4.2 \times 10^{-5} \times M_{\mu\mu}^{\min}. \tag{7.2}$$

7.2 Simulation of Standard Model Backgrounds

7.2.1 SM DY Background

The major background in the analysis is the SM DY process. This background is considered as an "irreducible" background since it cannot be distinguished from the CI signal process in the detector. A set of fully simulated samples are generated for the SM DY process ($Z/\gamma^* \to \mu\mu$) to predict the event yields from the major background. All the standard DY samples are generated using the NLO Monte Carlo event generator POWHEG [89] for different dimuon mass threshold ($M_{\mu\mu}^{\min}$) values from 120 GeV to 2000 GeV.

The standard DY samples produced by POWHEG are also required to determine the systematic uncertainty in the predicted CI/DY event yields as a result of uncertainty in the PDFs. The data set paths for the POWHEG NLO samples are listed in Table 7.3 and the details of cross sections and integrated luminosities of those samples are listed in Table 7.4.

Table 7.3. Dataset paths for SM DY samples generated using the POWHEG NLO generator [31].

No	Data Set Path Name
1	/DYToMuMu_M-120_CT10_TuneZ2star_8-powheg-pythia6/Summer12_DR53X-PU_S10_START53_V7C1-v1/AODSIM
2	/DYToMuMu_M-200_CT10_TuneZ2star_8-powheg-pythia6/Summer12_DR53X-PU_S10_START53_V7C1-v1/AODSIM
3	/DYToMuMu_M-500_CT10_TuneZ2star_8-powheg-pythia6/Summer12_DR53X-PU_S10_START53_V7C1-v1/AODSIM
4	/DYToMuMu_M-800_CT10_TuneZ2star_8-powheg-pythia6/Summer12_DR53X-PU_S10_START53_V7C1-v1/AODSIM
5	/DYToMuMu_M-1000_CT10_TuneZ2star_8-powheg-pythia6/Summer12_DR53X-PU_S10_START53_V7C1-v1/AODSIM
6	/DYToMuMu_M-1500_CT10_TuneZ2star_8-powheg-pythia6/Summer12_DR53X-PU_S10_START53_V7C1-v1/AODSIM
7	/DYToMuMu_M-2000_CT10_TuneZ2star_8-powheg-pythia6/Summer12_DR53X-PU_S10_START53_V7C1-v1/AODSIM

Table 7.4. Full simulation sample details for DY production generated using the POWHEG NLO generator [31].

$M_{\mu\mu}^{\min}$ (GeV)	$\sigma(pb)$	Integrated Luminosity (pb^{-1})
120	1.189×10^1	8.409×10^3
200	1.485×10^0	6.733×10^4
500	4.415×10^{-2}	2.265×10^6
800	5.491×10^{-3}	1.821×10^7
1000	1.796×10^{-3}	5.567×10^7
1500	1.710×10^{-4}	5.865×10^8
2000	2.210×10^{-5}	4.528×10^9

7.2.2 SM Non-DY Backgrounds

Other than the major SM DY background, the reducible SM non-DY processes are considered which contribute to a relatively small number of events in this analysis. These reducible backgrounds involve distinguishable signatures to separate the signal by applying appropriate selection cuts. The dataset paths relevant to this analysis for SM non-DY processes are listed in Table 7.5 and the details of simulated samples are given in Table 7.6.

All the SM non-DY event yields are listed in Table 7.7. They are arranged according from most to least significant starting from dimuon mass threshold 300 GeV. The "Other" column represents the cumulative event yields of the four different SM non-DY processes: W+jets, $\bar{t}$W, tW, and QCD.

Table 7.5. Dataset path details for SM non-DY background samples [31].

Process	Dataset path
DY$\to \tau^+\tau^-$	/DYToTauTau_M-20_CT10_TuneZ2star_8-powheg-pythia6/Summer12_DR53X-PU_S10_START53_V7A-v1/AODSIM
$t\bar{t}$	/TT_CT10_TuneZ2star_8-powheg-tauola/Summer12_DR53X-PU_S10_START53_V7A-v2/AODSIM
	/TT_Mtt-1000toInf_CT10_TuneZ2star_8-powheg-tauola/Summer12_DR53X-PU_S10_START53_V7A-v1/AODSIM
tW	/T_tW-channel-DR_TuneZ2star_8-powheg-tauola/Summer12_DR53X-PU_S10_START53_V7A-v1/AODSIM
$\bar{t}W$	/Tbar_tW-channel-DR_TuneZ2star_8-powheg-tauola/Summer12_DR53X-PU_S10_START53_V7A-v1/AODSIM
WW	/WW_TuneZ2star_8_pythia6_tauola/Summer12_DR53X-PU_S10_START53_V7A-v1/AODSIM
WZ	/WZ_TuneZ2star_8_pythia6_tauola/Summer12_DR53X-PU_S10_START53_V7A-v1/AODSIM
ZZ	/ZZ_TuneZ2star_8_pythia6_tauola/Summer12_DR53X-PU_S10_START53_V7A-v1/AODSIM
W+jets	/WJetsToLNu_TuneZ2Star_8-madgraph-tarball/Summer12_DR53X-PU_S10_START53_V7A-v1/AODSIM
QCD	/QCD_Pt_20_MuEnrichedPt_15_TuneZ2star_8_pythia6/Summer12_DR53X-PU_S10_START53_V7A-v3/AODSIM

Table 7.6. Sample details for SM non-DY background samples [31].

Process	Generator	Generator level cuts	Events	σ(pb)	Int. Lumi (pb^{-1})	Order
DY$\to \tau^+\tau^-$	POWHEG	$\sqrt{\hat{s}} >$20 GeV	$\sim$3.3M	1.915×10^3	1.721×10^3	NNLO
$t\bar{t}$	POWHEG	no cuts	$\sim$21.6M	2.34×10^2	9.263×10^4	NLO
	POWHEG	$\sqrt{\hat{s}} >$1000 GeV	$\sim$1.2M	3.28	3.808×10^5	NLO
tW	POWHEG	no cuts	$\sim$500k	1.11×10^1	4.483×10^4	NLO
$\bar{t}W$	POWHEG	no cuts	$\sim$500k	1.11×10^1	4.445×10^4	NLO
WW	PYTHIA	no cuts	$\sim$10M	5.480×10^1	1.825×10^5	NLO
WZ	PYTHIA	no cuts	$\sim$10M	3.320×10^1	3.012×10^5	NLO
ZZ	PYTHIA	no cuts	$\sim$10M	8.1	1.210×10^6	NLO
W+jets	MADGRAPH	no cuts	$\sim$18M	3.626×10^4	5.073×10^2	NNLO
QCD	PYTHIA	p$_T >$20 GeV	$\sim$21.4M	1.35×10^5	1.59×10^2	LO

7.2.3 Summary of SM Backgrounds

The predicted SM DY and total number of SM non-DY event yields are listed in Table 7.8 with their uncertainties according to the minimum dimuon masses ranging from 300 GeV to 2000 GeV. All the event yields are normalized to the integrated luminosity of 20 fb^{-1}. The dominant contribution to the dimuon event yields stems from the SM DY process for each dimuon mass threshold.

7.3 Predicted Dimuon Event Yields

The predicted event yields are evaluated using Equation 4.2 following to the method described in Section 7.1. The event yields correspond to an integrated luminosity of 20.6 fb^{-1} and are predicted as a function of Λ and M$_{\mu\mu}^{\min}$. The predicted CI signal event yields are based on 30 simulated CI signal samples (12 samples for destructive interference and another 18 samples for constructive interference), as described in Section 7.1, and those samples are produced only for odd Λ values. The prediction of events for even Λ values are based on the functional form of the CI/DY versus Λ. This functional form is associated with Equation 2.5 for the CI/DY cross section. The functional parameters are evaluated from a fit to the event yields for odd Λ values as illustrated in Figure 7.2. The

Table 7.7. The predicted event yields for SM non-DY processes after normalizing to the integrated luminosity of 20 fb^{-1}. "Other" represents the sum of event yields of W+jets, $\bar{t}$W, tW, and QCD processes [31].

M$_{\mu\mu}^{\min}$ (GeV)	$t\bar{t}$	Diboson	Other	Z$\to \tau^+\tau^-$
300	671.22	223.17	92.70	11.62
400	193.60	85.92	26.55	0.00
500	59.40	37.91	8.10	0.00
600	19.36	17.60	4.50	0.00
700	7.92	9.50	1.35	0.00
800	3.52	5.35	1.35	0.00
900	1.76	2.98	0.90	0.00
1000	0.44	1.60	0.00	0.00
1100	0.70	0.89	0.00	0.00
1200	0.40	0.66	0.00	0.00
1300	0.25	0.44	0.00	0.00
1400	0.20	0.26	0.00	0.00
1500	0.10	0.04	0.00	0.00
1600	0.00	0.04	0.00	0.00
1700	0.00	0.04	0.00	0.00
1800	0.00	0.00	0.00	0.00
1900	0.00	0.00	0.00	0.00
2000	0.00	0.00	0.00	0.00

predicted event yields for any Λ value are determined by linear interpolation between integer values of Λ using Table 7.9 and Table 7.10. A complete description of predicted event yields for SM DY and CI signals is given in Table 7.9 and Table 7.10 for destructive and constructive interference. Also the predicted event yields for the SM DY process can be compared with the data for a given dimuon mass threshold, M$_{\mu\mu}^{\min}$.
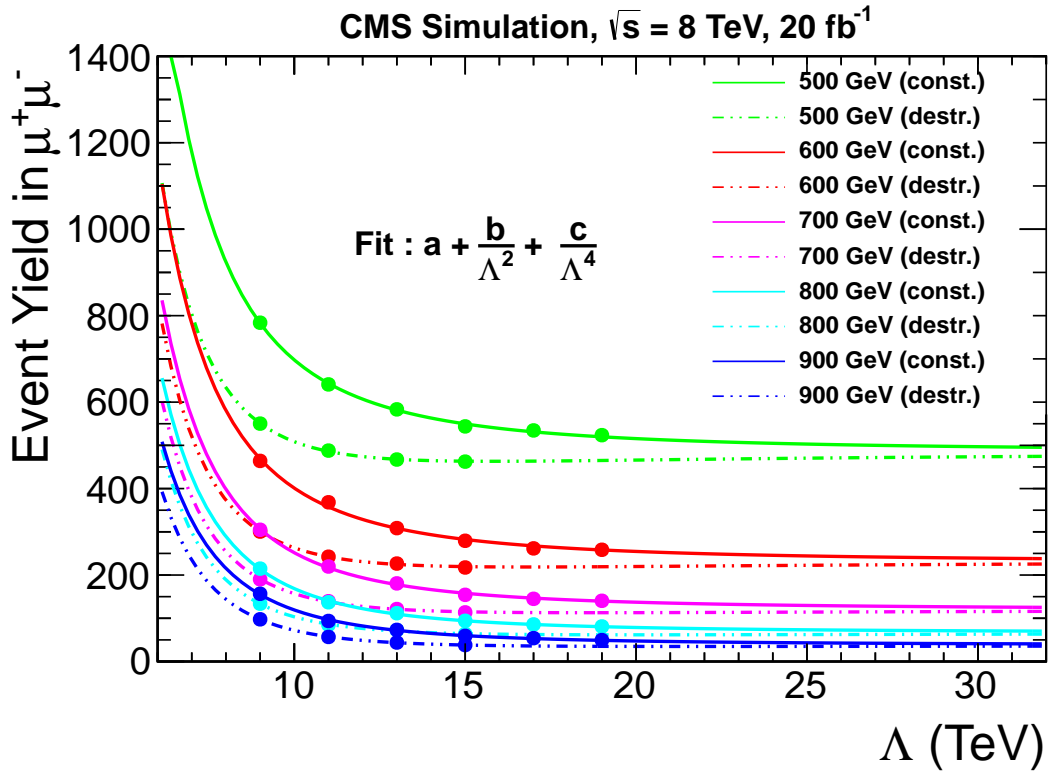
FIG. 7.2. Examples of fits to the predicted CI signal event yields versus Λ for different mass thresholds for constructive and destructive interference. These fitted functions are used to determine the predicted event yields for even Λ values. All the curves are fitted using the functional form of Equation 2.5 and the circles are for predictions for odd Λ values [31].

Table 7.8. The predicted event yields for SM DY and non-DY processes after normalizing to the integrated luminosity of 20 fb^{-1} [31].

	DY		Non-DY	
$M_{\mu\mu}^{min}$(GeV)	Events	Uncertainty	Events	Uncertainty
300	3937.81	80.153	998.71	29.86
400	1392.95	19.282	306.07	15.42
500	584.73	11.478	105.41	8.98
600	264.83	6.059	41.46	5.51
700	144.83	1.035	18.77	3.45
800	78.41	0.696	10.22	2.39
900	44.89	0.434	5.64	1.54
1000	26.29	0.155	2.04	0.83
1100	15.90	0.112	1.59	0.68
1200	9.85	0.077	1.06	0.51
1300	6.08	0.043	0.69	0.34
1400	3.90	0.032	0.46	0.21
1500	2.52	0.023	0.14	0.08
1600	1.66	0.015	0.04	0.04
1700	1.10	0.006	0.04	0.04
1800	0.74	0.005	0.00	0.00
1900	0.51	0.004	0.00	0.00
2000	0.34	0.003	0.00	0.00

Table 7.9. Observed and predicted number of dimuon events using the SM and LLIM for $M_{\mu\mu}^{min}$. The LLIM predictions are shown for destructive interference. Both the SM and CI predictions include small contributions from non-DY background. The integrated luminosity is 20.6 fb^{-1} [31].

$M_{\mu\mu}^{min}$ (GeV)	500	600	700	800	900	1000	1100	1200	1300	1400	1500
Source	Number of Events										
data	706.0	338.0	175.0	103.0	62.0	38.0	27.0	16.0	12.0	6.0	4.0
SM pred.	716.6	316.7	168.5	90.9	51.6	28.8	17.7	11.0	6.8	4.4	2.6
σ(SM pred.)	85.5	41.3	23.8	14.2	8.9	5.5	3.8	2.6	1.8	1.2	0.8
Λ (TeV)											
20	723.2	329.4	166.4	90.7	50.6	28.6	17.7	11.2	7.2	4.6	2.8
19	722.2	328.7	166.2	90.8	50.8	28.9	18.0	11.4	7.4	4.8	3.0
18	721.3	328.2	166.2	91.1	51.3	29.3	18.4	11.8	7.7	5.1	3.2
17	720.7	328.1	166.6	91.7	52.0	30.1	19.0	12.4	8.2	5.5	3.6
16	720.5	328.3	167.3	92.8	53.1	31.1	20.0	13.2	8.9	6.1	4.1
15	721.0	329.3	168.9	94.5	54.8	32.8	21.4	14.5	9.9	7.0	4.8
14	722.8	331.6	171.6	97.3	57.5	35.2	23.5	16.3	11.5	8.2	5.8
13	726.8	336.0	176.3	101.9	61.7	39.0	26.7	19.0	13.8	10.1	7.4
12	734.6	344.1	184.3	109.5	68.5	44.9	31.7	23.2	17.3	13.1	9.9
11	749.3	358.7	198.0	122.1	79.4	54.3	39.6	29.9	23.0	17.8	13.8
10	776.6	384.9	222.0	143.5	97.7	70.0	52.8	40.9	32.2	25.4	20.2

Table 7.10. Observed and predicted number of dimuon events as in Table 7.9. The LLIM predictions are shown for constructive interference [31].

$M_{\mu\mu}^{min}$ (GeV)	500	600	700	800	900	1000	1100	1200	1300	1400	1500
Source	Number of Events										
data	706.0	338.0	175.0	103.0	62.0	38.0	27.0	16.0	12.0	6.0	4.0
SM pred.	716.6	316.7	168.5	90.9	51.6	28.8	17.7	11.0	6.8	4.4	2.6
σ(SM pred.)	85.5	41.3	23.8	14.2	8.9	5.5	3.8	2.6	1.8	1.2	0.8
Λ (TeV)											
20	783.4	374.9	197.6	112.0	66.1	39.5	25.8	17.1	11.6	8.1	5.5
19	788.9	379.6	200.9	114.4	67.9	40.8	26.9	18.0	12.3	8.6	5.9
18	795.6	385.3	205.0	117.3	70.2	42.6	28.2	19.1	13.2	9.3	6.4
17	804.0	392.2	210.1	121.0	73.1	44.8	30.0	20.5	14.3	10.1	7.1
16	814.5	401.0	216.5	125.8	76.8	47.7	32.3	22.3	15.7	11.3	8.1
15	828.1	412.1	224.8	132.0	81.7	51.5	35.3	24.8	17.6	12.8	9.3
14	845.9	426.7	235.7	140.4	88.3	56.7	39.5	28.1	20.3	14.9	11.0
13	869.8	446.0	250.5	151.9	97.4	63.9	45.3	32.6	23.9	17.9	13.3
12	903.0	472.4	270.9	168.1	110.3	74.2	53.5	39.2	29.2	22.1	16.7
11	950.6	509.9	300.3	191.9	129.4	89.5	65.8	49.0	37.0	28.4	21.8
10	1021.4	565.2	344.1	228.2	158.5	113.2	84.7	64.0	49.2	38.3	29.6

Chapter 8

Estimation of Systematic Uncertainties

Most measurements of physical quantities involve both statistical uncertainties and systematic uncertainties. Systematic uncertainties are important factors in the measurement of physical quantities and play a key role with respect to the statistical uncertainties. The sources of the systematic uncertainties can be identified as uncertainties related to the nature of the detector, assumptions considered by the experimenter, and the parameters of the model used to make inferences that are themselves not precisely determined. The statistical analysis method used to define the 95% confidence level lower limits on the compositeness energy scale, Λ, also takes into account systematic uncertainties which can be classified into two categories, theoretical uncertainties and experimental uncertainties.

8.1 Theoretical Uncertainties

Theoretical uncertainties used in this analysis come from the uncertainties in higher order QCD K-factors, higher order QED K-factors, and the Parton Distribution Functions (PDFs).

Uncertainties of QCD and QED K-factors

Since the CI signal and DY samples are generated using the PYTHIA leading order Monte Carlo event generator, QCD and QED K-factors are used to bring the event yields to NLO accuracy. The theoretical uncertainty on the QCD K-factor is assigned as 3% based on a study using different PDF sets [95], which is slightly larger than the NNLO correction and independent of $M_{\mu\mu}^{\min}$ [96]. As mentioned previously, the QED K-factor is determined using Equation 7.2 and a theoretical uncertainty of 6.1% is assigned based on the deviations of QED K-factors from two different event generators [88].

Parton Distribution Function Uncertainties

A parton distribution function (PDF), $f_i(x, Q^2)$, is the probability density for finding a parton of flavor i, quark or gluon, in a proton carrying a fraction x of the proton momentum. This parton distribution function depends on two variables: momentum fraction x carried by a parton and the energy scale of the hard interaction, Q. The uncertainty of the parton distribution function is determined as a function of dimuon mass by analyzing the variations in event yields from fully simulated POWHEG samples for DY production for three PDF sets: CT10 [97], MSTW08 [98], and NNPDF21 [46]. The event yield is determined using the PDF4LHC [99] weighting procedure. The variations are considered with respect to the CT10 central value and the maximum and minimum envelope values are averaged to obtain a final value for uncertainty.

The Hessian method is used to derive these PDF sets [44] in which an N eigenvector basis of the PDFs is constructed and provides a method from which uncertainties on observables can be calculated. There are two main methods to evaluate the PDF uncertainties: the PDF weighting technique and the brute force method. This analysis utilized the PDF weighting technique to estimate PDF uncertainties since the brute force method involves generating a large number of MC samples and is extremely time consuming.

The modified tolerance method is used to determine the maximal positive and negative variations of the DY event yields since it gives the best performance even in cases where the fluctuations are not symmetric around the central values. The systematic uncertainties are evaluated at 68% confidence level at NLO and rely on the PDF4LHC

study. The 90% confidence level variations for the CT10 PDF set are scaled down to 68% using a factor of 1.64485. There is no scaling involved for the MSTW08 and NNPDF21 PDF sets since their variations are given at 68%. The results for the variations in the number of DY events based on the envelope of the three different PDF sets mentioned above, using the modified tolerance method, are given in the Table 8.1. The error bands in Figure 8.1 represent the asymmetric positive and negative uncertainties of the PDFs, $f_i(x, Q^2)$, calculated [100] using,

$$
\begin{aligned}
\Delta X^+ &= \sqrt{\sum_{i=1}^{N} [\max(X_i^+ - X_0, \ X_i^- - X_0, \ 0)]^2}, \\
\Delta X^- &= \sqrt{\sum_{i=1}^{N} [\max(X_0 - X_i^+, \ X_0 - X_i^-, \ 0)]^2},
\end{aligned}
$$

where the number of events X are X_0 using the central PDF value and $X_i^{\pm}$ using the PDFs for positive and negative variations of the PDF parameters along the ith- eigenvector direction in the n-dimensional PDF parameter space.

8.2 Experimental Uncertainties

The experimental uncertainties involved in this analysis are muon p_T scale uncertainty, muon p_T resolution uncertainty, dimuon reconstruction uncertainty, uncertainty in luminosity, and uncertainty for SM background estimates (DY and non-DY event yields).

The uncertainty in muon p_T scale occurs from the calibration of the magnetic field and the accuracy of the tracker alignment. This results in a dimuon yield uncertainty [88]

$$
\frac{\delta M}{M}(\%) = 0.0695^{(-0.000171 \times M)} + 9.98 \times 10^{-8}(M)^2 \tag{8.1}
$$

where M represents $M_{\mu\mu}^{\min}$ in units of GeV.

The uncertainty in muon p_T resolution increases with increasing p_T. This leads to an uncertainty on the dimuon event yields given by [88],
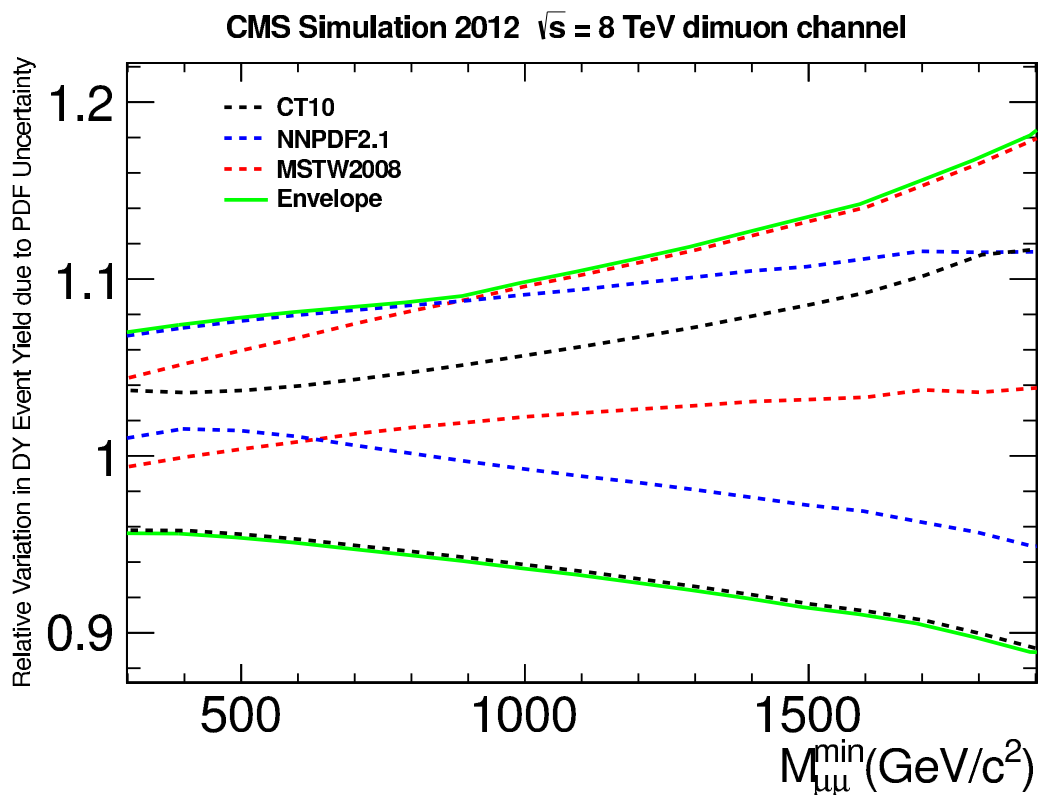
FIG. 8.1. Maximal positive and negative PDF uncertainties as a function of minimum dimuon mass based on the CT10, MSTW08 and NNPDF21 PDF sets [31].

Table 8.1. Maximal positive and negative event yield uncertainties due to PDF uncertainties evaluated from the envelope of the CT10, MSTW08 and NNPDF21 PDF sets using the modified tolerance method [31].

$M_{\mu\mu}^{\min}$ (GeV)	$\Delta X^+(\%)$	$\Delta X^-(\%)$
300	6.8	4.2
400	7.2	4.2
500	7.6	4.4
600	8.0	4.7
700	8.2	5.1
800	8.5	5.4
900	8.9	5.8
1000	9.6	6.2
1100	10.2	6.5
1200	10.9	7.0
1300	11.6	7.4
1400	12.5	7.9
1500	13.3	8.4
1600	14.1	8.8
1700	15.3	9.3
1800	16.5	10.1
1900	17.9	10.9
2000	20.5	11.1

$$\frac{\delta M}{M}(\%) = 5.3 \times 10^{-4} + 1.73 \times 10^{-2} M + 6.86 \times 10^{-3} (M)^2 \tag{8.2}$$

where M represents $M_{\mu\mu}^{\min}$ in units of TeV.

The uncertainty in muon reconstruction efficiency leads to a mass independent dimuon yield uncertainty of 3% [88] and the uncertainty in luminosity is 2.6% as quoted by the Luminosity Working Group [101]. The total uncertainty in the predicted number of events for SM dimuon production (DY and non-DY), including both statistical and systematic uncertainties, is shown in Figure 8.2 as a function of minimum dimuon mass. These DY predictions are based on POWHEG samples and non-DY predictions are based on POWHEG and MADGRAPH samples as described in Section 7.2. A complete description of theoretical and experimental uncertainties on dimuon yields is given in Table
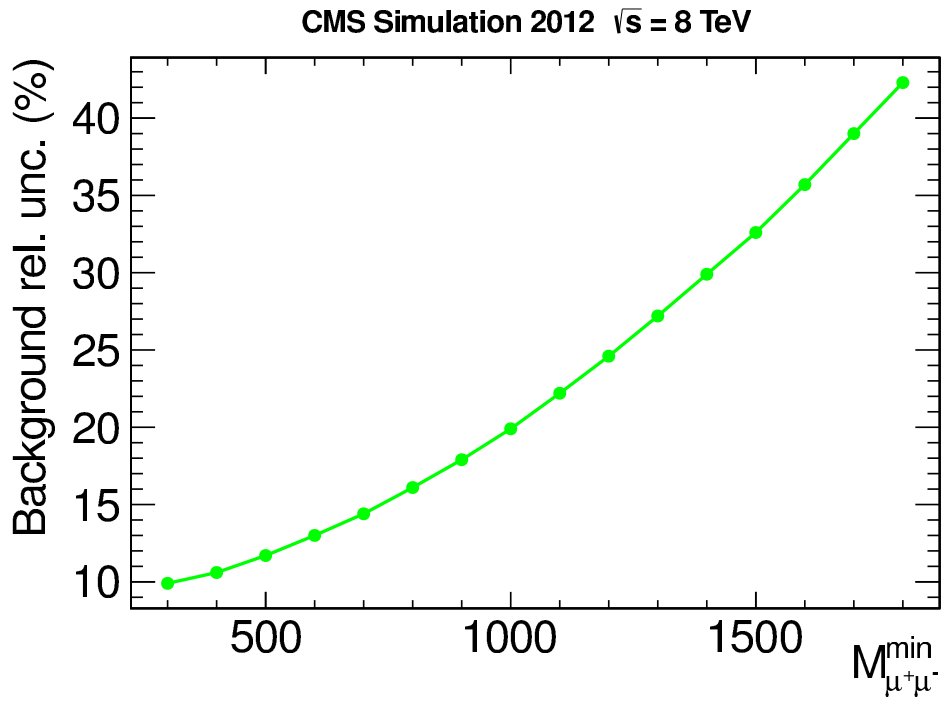
FIG. 8.2. The total relative uncertainty in the predicted event yields for SM dimuon production as a function of minimum dimuon mass. Here the uncertainty does not include the 2.6% uncertainty in luminosity.

8.2.

Table 8.2. All the systematic uncertainties on dimuon event yields. The PDF, p_T scale, p_T resolution, and QED K$-$factor uncertainties are quoted for $M_{\mu\mu}^{\min}$=1500 GeV; the other uncertainties are independent of $M_{\mu\mu}^{\min}$ [31].

SOURCE	Rel. Uncert. (%)
Momentum scale	27.8
PDF	10.8
QED K-factor	6.1
Momentum resolution	4.7
Luminosity	2.6
Muon reconstruction	3.0
QCD K-factor	3.0

Chapter 9

Statistical Method

A search for contact interactions is performed in the high mass region of the dimuon spectrum after all simulation corrections, event selections, and normalization to data are applied. This chapter introduces the frequentist approach for statistical inference, outlines the procedure for determining the consistency of the observed dimuon mass spectrum with the predicted distribution including background contribution, and in lieu of a discovery of new physics, provides general tools to set limits using the frequentist method. As will be discussed in Section 9.1, a modified version of the classical frequentist method (CL_s) [102,103], is used in the determination of the limits for constructive and destructive interference. Lower limits on Λ are established for the LLIM since the expected contribution from DY and other SM background sources are found to be consistent with the dimuon mass distribution measured using the 2012 CMS dataset, which will be discussed in detail in Section 9.2. Finally, the effect of the systematic uncertainties on the results will be discussed in Section 9.3.

9.1 Modified Frequentist Method

Uncertainties play a major role in experimental results, hence a measurement is incomplete or inconsequential unless an error interval is attributed to it. Different statistical methods have been used for this purpose. One of the two dominant statistical approaches used in high energy physics is based on the Bayesian framework, and the other is within

the frequentist framework. The Bayesian statistical method depends on a prior probability distribution which treats the data in an arbitrary manner. However, we frequently want to consider data that do not depend on a prior probability distribution. Thus, the classical frequentist statistical method is used as a framework for reporting search results. In this CI analysis, with no significant excess of events observed, exclusion limits are set using a modified version of the classical frequentist method (CL_s).

The limit setting procedure discussed below depends on either nuisance parameters or parameters of interest. Examples of nuisance parameters are fluctuations due to PDFs, detector efficiencies, etc.; parameters that have an impact on the predictions but are not under investigation in an experiment. If a parameter is being constrained in a given analysis in the absence of a signal, it is known as a parameter of interest. In this section, θ is used for nuisance parameters and μ for parameters of interest. The background signal and the expected signal are denoted by "b" and "s", respectively. Signal and background predictions are generally influenced by nuisance parameters, so, they normally become functions of nuisance parameters, $s(\theta)$ and $b(\theta)$.

Classical Frequentist Method

In the classical frequentist method, a test statistic [104] q_μ is defined to distinguish the signal-like events from the background-like events for the case of no systematic uncertainties. This method is derived from the probability density function of the test statistic:

$$q_\mu = -2 \ln \frac{\mathcal{L}(data|s(\mu) + b)}{\mathcal{L}(data|b)} \tag{9.1}$$

where $\mathcal{L}(data|s(\mu)+b)/\mathcal{L}(data|b)$ is the likelihood ratio with $\mathcal{L}(data|rate)$ the product of Poisson probabilities for a number of either observed or simulated events in each sub-channel given the expected signal and background rates. This test statistic compresses all signal-vs-background discriminating information into one number. J. Neyman and E.S. Pearson [105] showed that this test statistic, which is the ratio of the likelihoods [106], is the most powerful discriminator among all other test statistics. The goal is to determine

whether the data are consistent with background only or require new physics.

The next step after defining the test statistic is to construct a probability distribution functions (pdf) of q_μ under the *signal + background* hypothesis. With the use of these *pdfs*, the probability $P(q_\mu \geq q_\mu^{data}|s(\mu)+b)$ for the observed value of q_μ^{data} can be evaluated. This probability is denoted as CL_{s+b}. If $CL_{s+b} \leq 0.05$, the signal model is regarded as excluded at a 95% confidence level. The problem with the classical frequentist approach is that if the observed number of background events has a sufficient downward fluctuation [102], then the background only hypothesis will be falsely excluded. Even though one expects this exclusion probability to be zero, in the CL_{s+b} procedure, it approaches 0.05. Therefore, the CL_s method is used to prevent excluding background models in cases of low sensitivity. The CL_s method is used to set limits, and is one of the three methods described by the PDG [107] and is currently widely used at the LHC.

Modification of the Classical Frequentist Method

The CL_s method was first used in the Higgs search at LEP and illustrates the use of confidence levels. This method is utilized to obtain conservative limits on the signal hypothesis. In the modified frequentist method [108], $CL_s = CL_{s+b}/(1-CL_b)$ is calculated. Although this CL_s is a ratio of confidence levels, the signal hypothesis is considered excluded when $1 - CL_s \leq CL$, i.e., the value of confidence level CL_s is required to be less than or equal to 0.05 in order to exclude the signal at 95% C.L. By construction, the CL_s-based limits are one-sided. The method introduced by Feldman and Cousins, currently used at the LHC, constructs unified (i.e. one/two sided) confidence intervals based on the likelihood-ratio test statistic

$$q_\mu = -2\,ln\frac{\mathcal{L}(data|s(\mu)+b)}{\mathcal{L}(data|s(\hat{\mu})+b)}, \tag{9.2}$$

with $0 \leq \hat{\mu} \leq \mu$, and $\hat{\mu}$ maximizes the likelihood $\mathcal{L}(data|s(\mu)+b)$.

Systematic Uncertainties

There are two ways to introduce systematic uncertainties on signal ($s(\theta)$) and back-

ground ($b(\theta)$) rates: by modifications to the test statistics or the way in which pseudo data is generated. The effect of the systematic uncertainty is introduced before each pseudo data set is generated by drawing random numbers from the *pdf* distribution, $p(\theta|\tilde{\theta})$, where θ is the nuisance parameter and $\tilde{\theta}$ is the nominal value of the nuisance parameter. At the LHC, the test statistic is redefined to handle nuisance parameters by extending the likelihood

$$\mathcal{L}(data|s(\mu,\theta)+b(\theta)) = Poisson(data|s(\mu,\theta)+b(\theta))p(\theta|\tilde{\theta}). \tag{9.3}$$

After maximizing the likelihood with respect to the nuisance parameter, one can define the test statistic as

$$\tilde{q}_\mu = -2\,ln\frac{\mathcal{L}(data|s(\mu)+b,\hat{\theta}_\mu)}{\mathcal{L}(data|s(\hat{\mu})+b,\hat{\theta})}, \tag{9.4}$$

with $0 \leq \hat{\mu} \leq \mu$. Here $\hat{\theta}_\mu$ and $\hat{\theta}$ are maximum likelihood estimators for the *signal + background* hypothesis and *background-only* hypothesis, respectively. This one sided test statistic does not allow negative signals ($0 \leq \mu$) and ensures that the limits obtained are one-sided ($\hat{\mu} \leq \mu$), i.e., upward fluctuations of the data ($\hat{\mu} > \mu$) are not considered as evidence against the signal hypothesis. By assuming a signal with signal strength μ in the *signal + background* hypothesis and *background-only* hypothesis, Monte Carlo pseudo data is generated to construct *pdfs* $f(\tilde{q}_\mu|s(\mu)+b,\hat{\theta}_\mu^{obs})$ and $f(\tilde{q}_\mu|b,\hat{\theta}_0^{obs})$. Finally, with these distributions, two p-values associated with the actual observation for the *signal + background* (p_μ) and *background-only* (p_b) hypotheses are defined;

$$p_\mu = P(\tilde{q}_\mu \leq \tilde{q}_\mu^{obs}|signal + background) = \int_0^{\tilde{q}_\mu^{obs}} f(\tilde{q}_\mu|s(\mu)+b,\hat{\theta}_\mu^{obs})d\tilde{q}_\mu$$

$$1 - p_b = P(\tilde{q}_\mu \leq \tilde{q}_\mu^{obs}|background - only) = \int_0^{\tilde{q}_0^{obs}} f(\tilde{q}_\mu|b,\hat{\theta}_0^{obs})d\tilde{q}_\mu, \tag{9.5}$$

where $\hat{\theta}_\mu^{obs}$ and $\hat{\theta}_0^{obs}$ are values of nuisance parameters for the *signal + background* and *background-only* hypothesis respectively, that maximize the likelihood using the experimentally observed data. $\tilde{q}_\mu^{obs}$ is the observed value of the test statistic using experimental

data for a given signal parameter μ.

To calculate $CL_s(\mu)$:

$$CL_s(\mu) = \frac{p_\mu}{1 - p_b}. \tag{9.6}$$

Then this μ is adjusted until $CL_s = 0.05$ in order to quote the 95% confidence level upper limit.

Expected Limits

In order to define $\pm 1\sigma$ and $\pm 2\sigma$ bands, a large set of *background-only* pseudo data are generated and are used in CL_s calculations as if they are real data. Then a cumulative probability distribution of results is built and the point at which the distribution crosses the 50% quantile becomes the median expected value. At the 16% and 84% quantiles, the $\pm 1\sigma$ (68%) band is defined and at 2.5% and 97.5% quantiles, the $\pm 2\sigma$ (95%) band is defined.

9.2 Agreement of Data with SM Predictions

The measured dimuon mass spectrum for the integrated luminosity 20.6 fb^{-1} is shown in Figures 9.1 and 9.2 with predictions for the SM and the LLIM with constructive and destructive interference. The differential spectrum in $M_{\mu\mu}$ is shown in Figure 9.1 with variable bin widths. The integral spectrum is shown in Figure 9.2. The integral spectrum shows the number of events with $M_{\mu\mu} > M_{\mu\mu}^{min}$. These two figures also show the predicted distributions for CI/DY production for $\Lambda = 11, 13$, and 15. The error bars for data points show the statistical (Poisson) uncertainties. In Figure 9.2, it can also be seen that ratio of observed to predicted events in the SM is consistent with unity and this indicates the consistency of the data with the SM. The background-only probability can be used to quantify the background-only hypothesis by using a test statistic q_0:

$$q_0 = -2\ln\frac{\mathcal{L}(data|b, \hat{\theta}_0)}{\mathcal{L}(data|s(\hat{\mu}) + b, \hat{\theta})}, \tag{9.7}$$

FIG. 9.1. The dimuon mass spectrum for 20.6 fb^{-1} shown with predictions for the SM and the LLIM with constructive and destructive interference. The differential spectrum in M is shown with variable bin width. The error bars for data points show statistical (Poission) uncertainties. The error bars in the pedestal plot include statistical uncertainties in the data and both statistical and systematic uncertainties in the predictions [31].
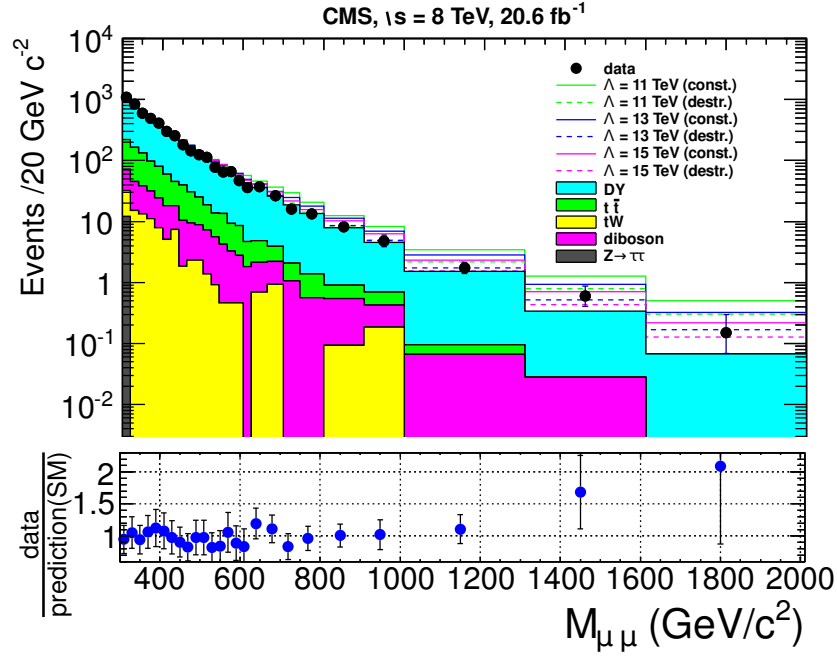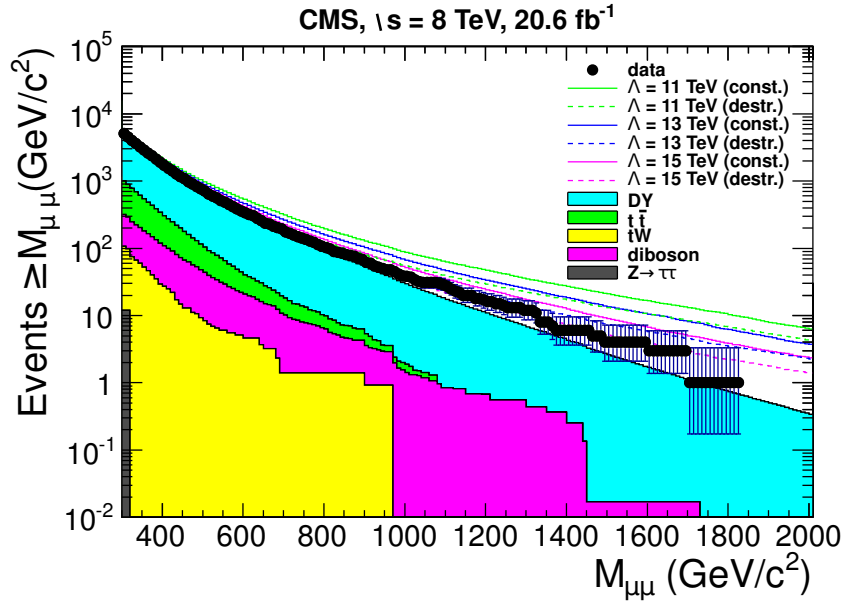

FIG. 9.2. The observed dimuon mass spectrum for 20.6 fb^{-1} shown with predictions for the SM and the LLIM with constructive and destructive interference. The integral spectrum in M is shown with variable bin width. The error bars for data points show statistical (Poisson) uncertainties [31].

with $\hat{\mu} \geq 0$. For events with downward fluctuations, the constraint $\hat{\mu} \geq 0$ gives an accumulation of the test statistic at zero.

Following this, pseudo data for nuisance parameters can be generated around $\hat{\theta}_0^{obs}$ to build the distribution $f(q_0|\hat{\theta}_0^{obs})$ for event counts under the assumption of the background-only hypothesis. By using this distribution, one can evaluate the probability that corresponds to a given experimental observation by

$$p_0 = P(q_0 \geq q_0^{obs}) = \int_{q_\mu^{obs}}^{\infty} f(q_0|b, \hat{\theta}_0^{obs})dq_0. \tag{9.8}$$

If $p_0 \geq 0.05$ (0.41 in this study), a good agreement can be seen between experimentally observed data and the background-only hypothesis. Based on the procedure mentioned above, one can calculate the p_0 values by considering the observed data, SM background predictions, and a set of nuisance parameters listed in Table. 8.2.

9.3 Lower Limits on Λ

The search for physics beyond the standard model is conducted by examining the dimuon final state. This study shows consistency between the observed events and the prediction from the standard model, thus motivating the setting of lower limits on Λ in the context of the LLIM. The limits are determined at 95% CL by using the CL_s modified frequentist method described above. The observed limits and the corresponding median expected limits are presented with the 1-σ and 2-σ bands, which are calculated using the LHC style CL_s prescription [109]. Throughout this analysis, an integrated luminosity of 20.6 fb^{-1} is used with the absolute error of 0.5 fb^{-1}, corresponding to a 2.6% uncertainty in the integrated luminosity. The expected mean for the number of signal events is the difference between number of CI/DY events expected for a given Λ and the number of DY events. The expected mean for the predicted background events includes the sum of DY and non-DY contributions. POWHEG samples are used to determine these DY yields.

Limits are determined for $M_{\mu\mu}^{min}$ in the mass range 300 GeV - 2000 GeV in steps

of 100 GeV. By taking into account fluctuations of the expected SM background, limits are set at 95% CL interval for a possible signal. During this procedure, the uncertainties in integrated luminosity, signal acceptances and background yields are considered as nuisance parameters with log-normal distributions. Version V00-02-06 of the roostat_cl95 routine is used to implement the CL_s method.

The input parameters for the CLs program are integrated luminosity, error on integrated luminosity, efficiency $\times$ acceptance, error on efficiency $\times$ acceptance, background estimate, error on background estimate, and number of observed events. The options chosen for this analysis are Poisson statistics for the signal fluctuation, lognormal [110, 111] distributions for nuisance parameters, and the CL_s method for statistical inference. To find the error on the predicted background, one can use the quadratic sum of the systematic uncertainties appropriate for each channel which include systematic uncertainties due to PDFs, p_T scale, p_T resolution, and K-factors (Table 8.2) along with statistical uncertainties.

As mentioned above using all the key arguments the CLs program returns the observed limit and the median of the expected lower limit on the cross section for CI signal as a function of $\mathrm{M}_{\mu\mu}^{min}$ at 95 % CL with 1-σ and 2-σ fluctuations. The resultant cross sections are converted to event yields using multiplication by luminosity followed by a mapping which depends on Λ as shown in Tables 7.9 and 7.10.

Figures 9.3 and 9.4 show the observed and expected lower limits on Λ as a function of $M_{\mu\mu}^{min}$ at 95% CL for destructive and constructive interference. The expected limit of $M_{\mu\mu}^{min}$ peaks at 1200 GeV for constructive interference and 1500 GeV for destructive interference, and the observed (expected) limits on Λ are 14.8 TeV (16.9 TeV) for constructive interference and 12.4 TeV (13.1 TeV) for destructive interference. The observed and expected limits agree within the uncertainties with an excursion into the $\pm 2\sigma$ band where the observed number of events have an upward fluctuation [31].
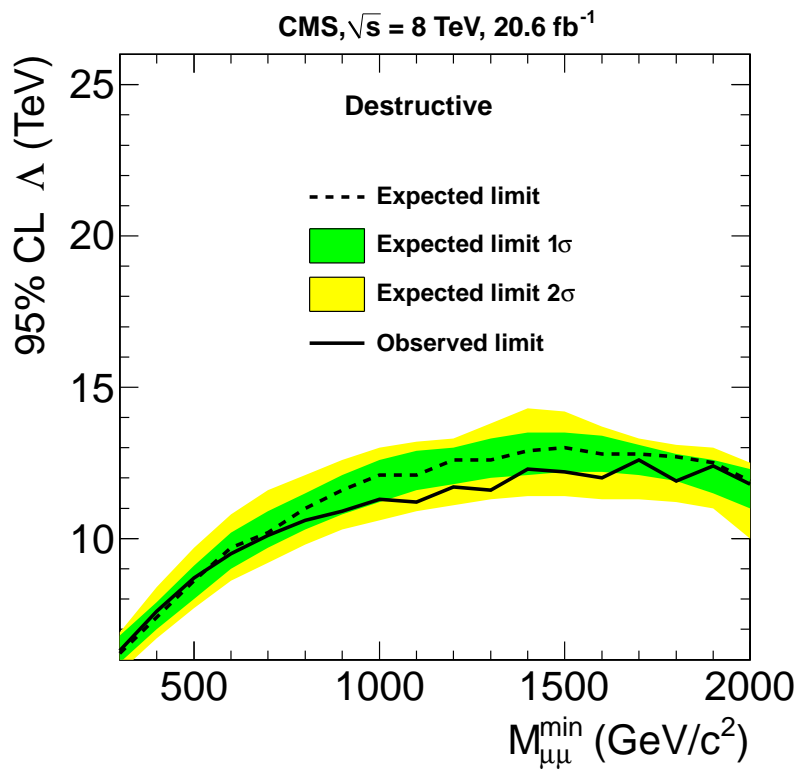
FIG. 9.3. Observed and expected limits on Λ for destructive interference [31].
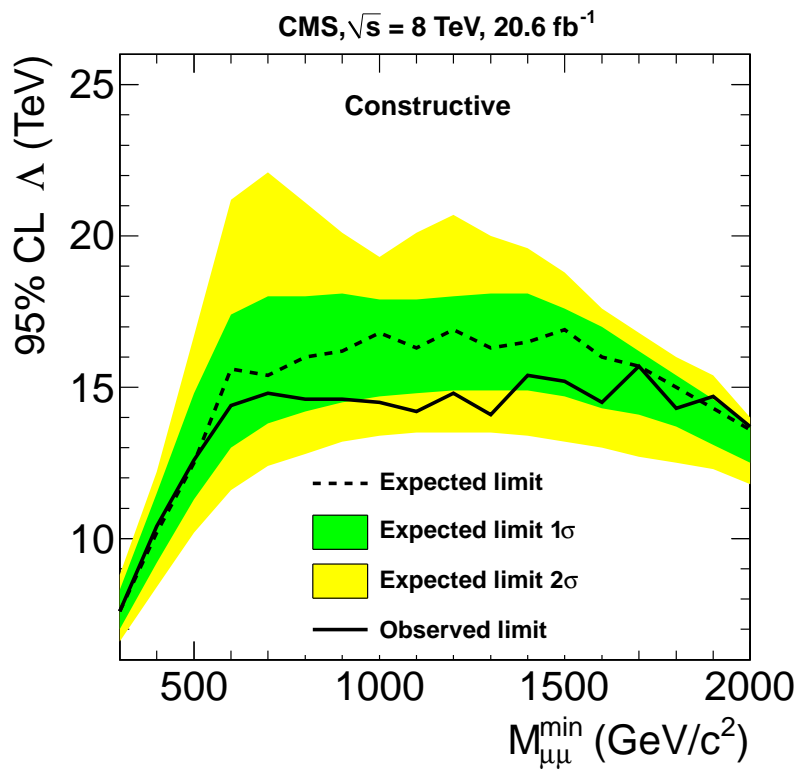
FIG. 9.4. Observed and expected limits on Λ for constructive interference [31].

Chapter 10

Results and Conclusion

This dissertation represents an effort to find contact interactions using the data collected by the CMS experiment at center of mass energy of 8 TeV during its operation in 2012. The dimuon invariant mass spectrum is measured based on an integrated luminosity of 20.6 fb^{-1}. The predictions for the number of signal and background events are made using Monte Carlo simulations in the context of left-left isoscalar model of quark and lepton compositeness with energy scale parameter Λ and the SM. The observed dimuon invariant mass spectrum for 2012 CMS data is found to be consistent with the predicted standard model DY and other standard model non-DY sources for the dimuon invariant mass ranging from 300 to 2000 GeV/c^2. At 95% confidence level, lower limits on compositness energy scale Λ are determined for constructive and destructive interference in the context of the LLIM. The limits, 14.8 TeV for constructive and 12.4 TeV for destructive interference represent the most stringent limits to date with respect to the current published limits of 13.1 TeV and 9.5 TeV.

Since the LLIM is an helicity conserving model to study quark and lepton compositeness and the limit on Λ is already increased up to 14.8 TeV during this study, it might be useful to study the dimuon mass spectrum using the helicity non conserving model which is already built in PYTHIA. The dimuon angular spectrum is another possible method to search for evidence for quark and lepton compositeness either in helicity conserving or non-conserving compositeness models as explained in Appendix C.

The sensitivity of the compositeness search improves with increasing center of mass energy of the colliding protons. Therefore, there is always an excellent opportunity to find evidence for quark and lepton compositeness once the LHC resumes its operation at the unprecedented center of mass energy of 14 TeV in 2015. This LHC Run II might be very interesting and an exciting time for particle physicists to confirm or rule out possible new physics in the TeV energy domain.

APPENDIX A
Highest Mass Dimuon Event Details

No	Lumi-Section	Run No	Event No	$M\mu\mu$ (GeV/c^2)
1	553	199409	676990060	1824
2	931	202178	1100609921	1697
3	398	205694	416479300	1694
4	153	206207	186909124	1592
5	215	207924	209747123	1486
6	193	195378	225870452	1453
7	531	199409	654043540	1367
8	1215	204601	1278017291	1357
9	77	196433	39187003	1327
10	1054	199833	1136357968	1325
11	995	194050	936530164	1322
12	541	199812	636694094	1319
13	90	196431	66057632	1290
14	666	208391	845554877	1248
15	78	207492	65524201	1232
16	641	198969	779619791	1212
17	323	202087	421813187	1192
18	368	204563	499818262	1188
19	444	194912	739866334	1168
20	97	199571	109753290	1166
21	40	199753	42023310	1136
22	327	202237	509578194	1130
23	1075	198487	1150495912	1125
24	733	202504	919226848	1114
25	13	194225	14353212	1112
26	685	206869	629195087	1109
27	171	191718	211765901	1106
28	1359	193621	1067285891	1097
29	699	198271	802097775	1095
30	194	201624	250169307	1083
31	654	194424	909915359	1077
32	50	207922	55833120	1030
33	221	204563	272281825	1029
34	96	208487	170918748	1023
35	244	194150	302855323	1018
36	186	204601	252896431	1017

37	556	195915	836688041	1014
38	39	207273	47981615	1006
39	4	207884	4187119	995
40	394	202328	589121740	986
41	215	206187	274374421	983
42	160	199008	179760542	976
43	280	194115	257882341	974
44	39	205667	42407203	974
45	167	201173	145943466	974
46	166	199436	119847245	965
47	99	196027	153238373	964
48	413	202060	527655267	961
49	57	201669	104849581	946
50	676	206243	974886749	945
51	48	195774	94924923	938
52	431	206744	605265207	934
53	79	199574	60631621	928
54	82	194533	85367726	927
55	472	195397	673031590	923
56	591	196218	860336640	918
57	802	198230	738690849	918
58	1568	194050	1391733189	916
59	591	199008	721792661	913
60	341	201202	312065562	911
61	1611	195552	1774851027	908
62	847	202060	1016136621	906

APPENDIX B

Dimuon Event Yields for Standard DY Production and Composite Production

(modified version of an existing software code)

```
# File Name: DY_MUMU_GEN_ITCM5.py

# Revision: 1.353

# Source: /local/reps/CMSSW.admin/CMSSW/Configuration/PyReleaseValidation
         /python/ConfigBuilder.py


import FWCore.ParameterSet.Config as cms
process = cms.Process('GEN')


# import of standard configurations
process.load('Configuration.StandardSequences.Services_cff')

process.load('SimGeneral.HepPDTESSource.pythiapdt_cfi')

process.load('FWCore.MessageService.MessageLogger_cfi')

process.load('Configuration.EventContent.EventContent_cff')

process.load('SimGeneral.MixingModule.mixNoPU_cfi')

process.load('Configuration.StandardSequences.GeometryDB_cff')

process.load('Configuration.StandardSequences.MagneticField_38T_cff')

process.load('Configuration.StandardSequences.Generator_cff')

process.load('IOMC.EventVertexGenerators.VtxSmearedRealistic8TeV
            Collision_cfi')

process.load('GeneratorInterface.Core.genFilterSummary_cff')

process.load('Configuration.StandardSequences.EndOfProcess_cff')

process.load('Configuration.StandardSequences.Frontier
            Conditions_GlobalTag_cff')
```

```
process.maxEvents = cms.untracked.PSet(
    input = cms.untracked.int32(100000))


# Input source
process.source = cms.Source("EmptySource")
process.options = cms.untracked.PSet()


# Production Info
process.configurationMetadata = cms.untracked.PSet(
    version = cms.untracked.string('$Revision: 1.353 $'),
    annotation = cms.untracked.string('Configuration/GenProduction
                /python/EightTeV/PY_MSUB1_200_MuMu_cfi.py nevents:1000'),
    name = cms.untracked.string('PyReleaseValidation'))


# Output definition
process.RAWSIMoutput = cms.OutputModule("PoolOutputModule",
    splitLevel = cms.untracked.int32(0),
    eventAutoFlushCompressedSize = cms.untracked.int32(5242880),
    outputCommands = process.RAWSIMEventContent.outputCommands,
    fileName = cms.untracked.string
            ('SEMI_FINAL_PYTHIA_M500_FSROFF_n2p4_Pt5_100K_ITCM5.root'),
    dataset = cms.untracked.PSet(
        filterName = cms.untracked.string(''),
        dataTier = cms.untracked.string('GEN-SIM')),
    SelectEvents = cms.untracked.PSet(
        SelectEvents = cms.vstring('generation_step')))


# Additional output definition
# Other statements
```

```
process.GlobalTag.globaltag = 'START53_V5::All'


process.generator = cms.EDFilter("Pythia6GeneratorFilter",
    pythiaPylistVerbosity = cms.untracked.int32(0),
    filterEfficiency = cms.untracked.double(1.0),
    pythiaHepMCVerbosity = cms.untracked.bool(False),
    comEnergy = cms.double(8000.0),
    maxEventsToPrint = cms.untracked.int32(0),
    PythiaParameters = cms.PSet(
        pythiaUESettings = cms.vstring('MSTU(21)=1
                ! Check on possible errors during program execution',


            'MSTJ(41)=1     ! FSR turn OFF',
            'MSTJ(22)=2     ! Decay those unstable particles',
            'PARJ(71)=10 .  ! for which ctau  10 mm',
            'MSTP(33)=0     ! no K factors in hard cross sections',
            'MSTP(2)=1      ! which order running alphaS',
            'MSTP(51)=10042 ! structure function chosen (external PDF CTEQ6L1)',
            'MSTP(52)=2     ! work with LHAPDF',
            'PARP(82)=1.921 ! pt cutoff for multiparton interactions',
            'PARP(89)=1800. ! sqrts for which PARP82 is set',
            'PARP(90)=0.227 ! Multiple interactions: rescaling power',
            'MSTP(95)=6     ! CR (color reconnection parameters)',
            'PARP(77)=1.016 ! CR',
            'PARP(78)=0.538 ! CR',
            'PARP(80)=0.1   ! Prob. colored parton from BBR',
            'PARP(83)=0.356 !Multiple interactions: matter distribution
                        parameter',
            'PARP(84)=0.651 !Multiple interactions: matter distribution
```

```
                         parameter',
      'PARP(62)=1.025 ! ISR cutoff',
      'MSTP(91)=1      ! Gaussian primordial kT',
      'PARP(93)=10.0  ! primordial kT-max',
      'MSTP(81)=21     ! multiple parton interactions 1 is Pythia default',
      'MSTP(82)=4      ! Defines the multi-parton model'),
  processParameters = cms.vstring('MSEL = 0   !User defined process',
#   'MSUB(1)      = 1     !Inclusive Z/Gamma* production or Pure DY',
     'MSUB(165)    = 1     !CI+g*/Z->mumu',
     'MSTP(32)     = 4     !forcing a 2->2 process to 2->1 process',
     'MSTP(43)     = 3     !Both Z0 and gamma*',
     'ITCM(5)      = 0     !LL, all upper quarks composite',
     'KFPR(165,1)  = 13    !mu+mu final state',
     'MDME( 174,1) = 0     !Z decay into d dbar',
     'MDME( 175,1) = 0     !Z decay into u ubar',
     'MDME( 176,1) = 0     !Z decay into s sbar',
     'MDME( 177,1) = 0     !Z decay into c cbar',
     'MDME( 178,1) = 0     !Z decay into b bbar',
     'MDME( 179,1) = 0     !Z decay into t tbar',
     'MDME( 182,1) = 0     !Z decay into e- e+',
     'MDME( 183,1) = 0     !Z decay into nu_e nu_ebar',
     'MDME( 184,1) = 1     !Z decay into mu- mu+',
     'MDME( 185,1) = 0     !Z decay into nu_mu nu_mubar',
     'MDME( 186,1) = 0     !Z decay into tau- tau+',
     'MDME( 187,1) = 0     !Z decay into nu_tau nu_taubar',
     'CKIN(1)      = 500',
#    'CKIN(2)      = 300' ),
  parameterSets = cms.vstring('pythiaUESettings',
      'processParameters')))
```

```
process.mumugenfilter = cms.EDFilter("MCParticlePairFilter",

    Status = cms.untracked.vint32(1, 1),

    MinPt = cms.untracked.vdouble(5, 5),

    MaxEta = cms.untracked.vdouble(2.4, 2.4),

    MinEta = cms.untracked.vdouble(-2.4, -2.4),

    ParticleCharge = cms.untracked.int32(-1),

    ParticleID1 = cms.untracked.vint32(13),

    ParticleID2 = cms.untracked.vint32(13))


process.ProductionFilterSequence =
        cms.Sequence(process.generator+process.mumugenfilter)


# Path and EndPath definitions
process.generation_step = cms.Path(process.pgen)

process.genfiltersummary_step = cms.EndPath(process.genFilterSummary)

process.endjob_step = cms.EndPath(process.endOfProcess)

process.RAWSIMoutput_step = cms.EndPath(process.RAWSIMoutput)


# Schedule definition
process.schedule = cms.Schedule(process.generation_step,process.
              genfiltersummary_step,process.endjob_step,
              process.RAWSIMoutput_step)


# filter all path with the production filter sequence for path
  in process.paths:
getattr(process,path)._seq= process.ProductionFilter
                        Sequence * getattr(process,path)._seq
```

APPENDIX C

Dimuon Angular Distribution

The Pythia MC generator is used to simulate the angular distributions of oppositely charged pairs of muons produced in pp collisions at center of mass energy 7 TeV. The distributions are evaluated in the context of standard model Drell-Yan production and an exotic left-left isoscalar model (LLIM) of quark and lepton compositeness. The angular distribution in the rest frame of the muon pair is characterized by the mean cosine of the angle between the negative muon and the boost direction. This study is performed to find the dependence of the mean cosine on the invariant mass of the pair and the energy scale parameter of the LLIM.

Definition of Dimuon Angle

Dimuon angle is defined as the angle between the direction of the lab frame and the direction of the μ^- in the dimuon rest frame, as shown in Figure C.1.

Mathematical Description of Dimuon Angle

The four-momentum vectors of the muons in the lab frame are

$P_1 = (P_{x1}, P_{y1}, P_{z1}, E_1),$

$P_2 = (P_{x2}, P_{y2}, P_{z2}, E_2),$ and sum

$P = P_1 + P_2,$

where P_1, P_2 and P are the four-momentum vectors of the μ^-, μ^+ and center of mass of dimuons in the lab frame. The four-momentum vectors of the muons in the dimuon rest frame are:

$P_1' = (P_{x1}', P_{y1}', P_{z1}', E_1'),$

$P_2' = (P_{x2}', P_{y2}', P_{z2}', E_2'),$ and sum

$P' = (P_1 + P_2),$

where P_1', P_2' and P' are the four-momentum vectors of the μ^-, μ^+ and the lab frame in the dimuon rest frame. Defining the decay angle of the dimuon pair using the
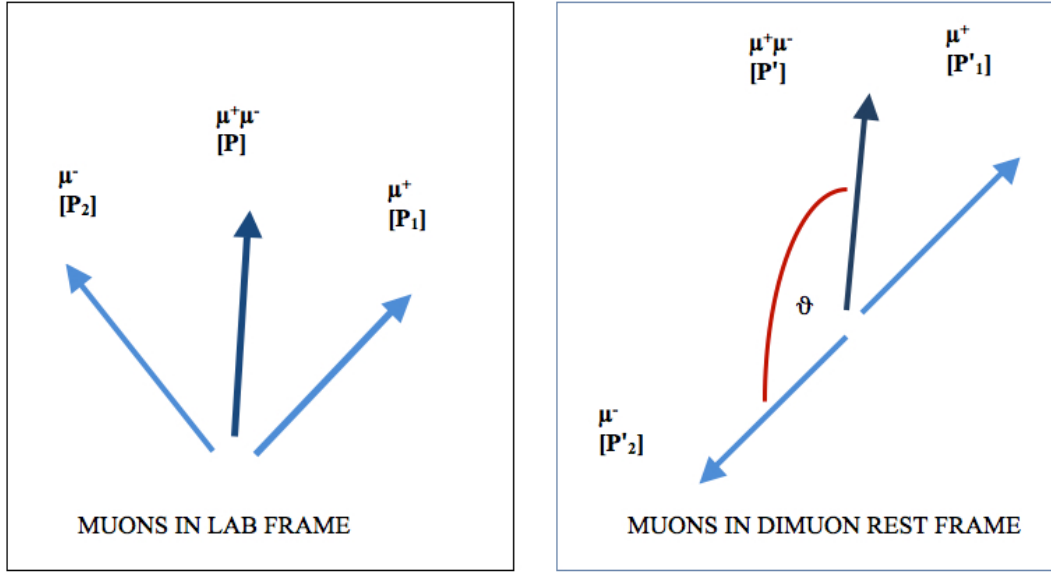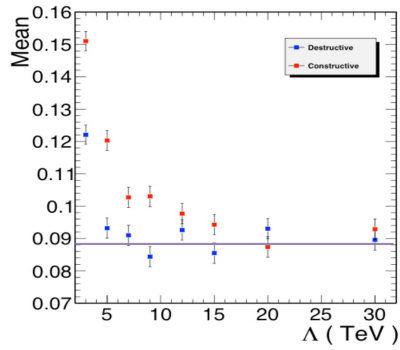
FIG. C.1. Dimuon Angle

scalar product of the four-momentum vectors of the μ^- and the lab frame in the dimuon rest frame,

$$P' \cdot P_1' = \mid P' \mid \mid P_1' \mid Cos(\Theta), \text{ and}$$

$$Cos(\Theta) = (P' \cdot P_1') \ / \ (\mid P' \mid \mid P_1' \mid).$$

Event production for the dimuon angular study is performed using the Pythia Monte Carlo event generator at 7 TeV center of mass energy. The LLIM is used with the kinematic cuts of $P_T > 40$ GeV and $\mid \eta \mid < 2.1$. The angular spectrum is analysed in three different dimuon mass ranges: $M_{\mu\mu} > 200$ GeV/c^2, $600 < M_{\mu\mu} < 900$ GeV/c^2 and $1900 < M_{\mu\mu} < 2000$ GeV/c^2.

The solid horizontal line in each plot represents the mean cosine of dimuon angle for the SM. The maximum deviation of the mean cosine of dimuon angle for the LLIM occurs at low values. This deviation decreases with and eventually approaches the SM prediction. The study also shows that the mean cosine of dimuon angle for constructive interference is larger than for destructive interference. For large dimuon masses, a large deviation of the LLIM prediction from the SM persists even at large values of Λ.

(a) Mean cosine distributions for $M_{\mu\mu} > 200$ GeV
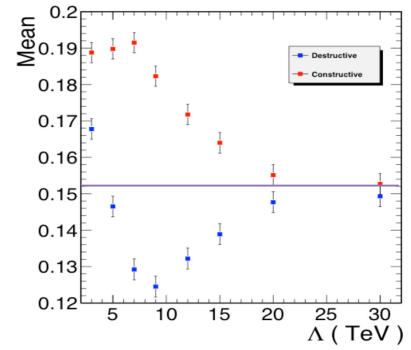
(b) Mean cosine distributions for 600 $< M_{\mu\mu} < 900$ GeV
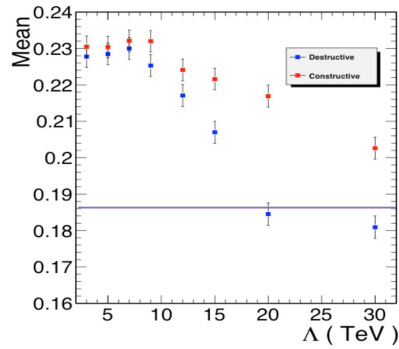
(c) Mean cosine distributions for 1900 $< M_{\mu\mu} < 2000$ GeV

FIG. C.2. Mean cosine distribution of dimuon angles for constructive and destructive interference.

BIBLIOGRAPHY

[1] F. Halzen and A. D. Martin, "Quark and Leptons: An Introductory Course in Modern Particle Physics", (John Wiley and Sons, New Jersey, 1984)

[2] M. E. Peskin and D. V. Schroeder, "An Introduction to Quantum Field Theory", (Westview Press, Colorado, 1995)

[3] S. L. Glashow, "Partial Symmetries of Weak Interactions", Nucl. Phys. **22**, 579-588 (1961)

[4] S. Weinberg, "A model of leptons", Phys. Rev. Lett. **19**, 1264 (1967)

[5] http://lhc-machine-outreach.web.cern.ch/lhc-machine-outreach

[6] D. Griffiths, "Introduction to Elementary Particles", (John Wiley and Sons, New Jersey, 2008)

[7] J. C. Pati, "Lepton number as the fourth color", Phys. Rev. D **10**, 275-289 (1974)

[8] H. Harari, "A schematic model of quarks and leptons", Phys. Lett. B **86**, 083-086 (1979)

[9] CDF Collaboration, "Limits on quark-lepton compositeness scales from dileptons produced in 1.8 TeV pp collisions", Phys. Rev. Lett. **79**, 2198 (1997)

[10] E. Eichten et al., "Supercollider Physics", Rev. Mod. Phys. **56**, 579-707 (1984)

[11] S. D. Drell and T. M. Yan, "Massive lepton-pair production in hadron-hadron collision at high energies", Phys. Rev. Lett. **25**, 316 (1970)

[12] P. A. M. Dirac, "The Quantum Theory of the Emission and Absorption of Radiation", Proc. Roy. Soc. **A114**, 243 (1927)

[13] R. P. Feynman, "Space-Time Approach to Non-Relativistic Quantum Mechanics", Rev. Mod. Phys. **20**, 367-387 (1948)

[14] R. P. Feynman, "Relativistic Cut-Off for Quantum Electrodynamics", Phys. Rev. **74**, 1430-1438 (1948)

[15] J. Schwinger, "On Quantum-Electrodynamics and the Magnetic Moment of the Electron", Phys. Rev. **73**, 416-417 (1948)

[16] S. Tomonaga and J. R. Oppenheimer, "On Infinite Field Reactions in Quantum Field Theory", Phys. Rev. **74**, 224-225 (1948)

[17] F. J. Dyson, "The Radiation Theories of Tomonaga, Schwinger, and Feynman", Phys. Rev. **75**, 486-502 (1949)

[18] W. Pauli, Open letter to the Radioactivity Group at the Regional Meeting at Tubingen, Zurich, December 4, 1930

[19] E. Fermi, "Versuch einer theorie der $\beta-$ strahlen-Towards the theory of $\beta-$rays", Z. Phys **88**, 161 (1934)

[20] S. L. Glashow, "Partial symmetries of weak interactions", Nucl. Phys. **22**, 579-588 (1961)

[21] S. Weinberg, "A model of leptons", Phys. Rev. Lett., **19**, 1264-1266 (1967)

[22] A. Salam, "Weak and electromagnetic interactions. Elementary Particle Theory", Proceedings of The Nobel Symposium held at Lerum, Sweden, 367-377 (1968)

[23] M. L. Perl, "The Discovery of the Tau Lepton", SLAC-PUB-5937 (1992)

[24] S. W. Herb et al., "Observation of a dimuon resonance at 9.5 GeV in 400 GeV proton-nucleus collision", Phys. Rev. Lett. **39**, 252-255 (1977)

[25] F. Abe et al., "Observation of top quark production in $p\bar{p}$ collisions with the Collider Detector at Fermilab", Phys. Rev. Lett. **74**, 2626-2631 (1995)

[26] S. Abachi et al., "Observation of the top quark", Phys. Rev. Lett. **35**, 1489 (1995)

[27] K. Kodama et al., "Observation of tau neutrino interactions", Phys. Lett. B **504**, 218-224 (2001)

[28] ATLAS Collaboration, "Observation of a new particle in the search for the Standard Model Higgs boson with the ATLAS detector at the LHC", Phys. Lett. B **716**, 1-29 (2012)

[29] CMS Collaboration, "Observation of a new boson at a mass of 125 GeV with the CMS experiment at the LHC", Phys. Lett. B **716**, 30 (2012)

[30] E. Eichten, K. Lane, and M. Peskin, "New Tests for Quark and Lepton Substructure", Phys. Rev. Lett. **50**, 811-814 (1983)

[31] CMS Collaboration, Search for Contact interactions in Dilepton Mass Spectra in pp Collisions at $\sqrt{s}$ =8 TeV, Internal Document

[32] H1 Collaboration, "Search for new physics in eq interactions at HERA", Phys. Lett. B **568**, 35-47 (2003)

[33] ZEUS Collaboration, "Search for contact interactions, large extra dimensions and fnite quark radius in ep collisions at HERA", Phys. Lett. B **591**, 23-41 (2004)

[34] L3 Collaboration, "Search for manifestations of new physics in fermion-pair production at LEP", Phys. Lett. B **489**, 81 (2000)

[35] DELPHI Collaboration, "Measurement and interpretation of fermion-pair production at LEP energies above the Z resonance", Eur. Phys. J. C **45**, 589-632 (2004)

[36] ALEPH Collaboration, "Measurement of the High-Mass Drell-Yan Cross Section and Limits on Quark-Electron Compositeness Scales", Eur. Phys. J. C **49**, 411-437 (2007)

[37] CDF Collaboration, "Limits on Quark-Lepton Compositeness Scales from Dileptons Produced in 1.8 TeV $p\bar{p}$ Collisions", Phys. Rev. Lett. **79**, 2198-2203 (1997)

[38] D0 Collaboration, "Measurement of the High-Mass Drell-Yan Cross Section and Limits on Quark-Electron Compositeness Scales", Phys. Rev. Lett. **82**, 4769-4774 (1999)

[39] D0 Collaboration, "Measurement of Dijet Angular Distribution at $\sqrt{s} = 1.96$ TeV and Searches for Quark Compositeness and Extra Spatial Dimensions", Phys. Rev. Lett. **103**, 191803 (2009)

[40] ATLAS Collaboration, "Search for quark contact interactions in dijet angular distributions in pp collisions at $\sqrt{s} = 7$ TeV measured with the ATLAS detector", Phys. Lett. B **694**, 327-345 (2011)

[41] ATLAS Collaboration, "Search for Contact Interactions in Dimuon Events from pp Collision at $\sqrt{s} = 7$ TeV with the ATLAS Detector", Phys. Rev. D **84**, 011101 (2011)

[42] CMS Collaboration, "Search for Quark Compositeness with the Dijet Centrality Ratio in pp Collisions at $\sqrt{s} = 7$ TeV", Phys. Rev. Lett. **105**, 262001 (2010)

[43] CMS Collaboration, "Search for contact interactions in $\mu^+\mu^-$ events in pp collisions at $\sqrt{s} = 7$ TeV", Phys. Rev. D **87**, 032001 (2013)

[44] A. D. Martin et al., "Parton distributions for the LHC", Eur. Phys. J. C **63**, 189-285 (2009)

[45] J. Pumplin et al., "New Generation of Parton Distributions with Uncertainties from Global QCD Analysis", JHEP 0207 (2002)

[46] NNPDF Collaboration, "Fitting Parton Distribution Data with Multiplicative Normalization Uncertainties", JHEP **1005** 075 (2010)

[47] J.C. Collins, D.E. Soper, and G. Sterman, "Factorization of hard processes in QCD", *adv.Ser.Direst.High Energy Phys.* **5** 1-91 (1988)

[48] CMS Collaboration, "The CMS experiment at the CERN LHC", JINST **3**, S08004 (2008)

[49] CMS Collaboration, "The Compact Muon Solenoid technical proposal", **CERN-LHCC-94-38** (1994)

[50] CMS Collaboration, "CMS physics technical design report, volume I: Detector performance and software", **CERN-LHCC-2006-001** (2006)

[51] http://lhc-machine-outreach.web.cern.ch/lhc-machine-outreach/images/complex/Cern-complex.gif

[52] CMS Collaboration, "The CMS experiment at the CERN LHC", JINST **3**, S08004 (2008)

[53] The ATLAS Collaboration, "The ATLAS Experiment at the CERN Large Hadron Collider", JINST **3**, S08003 (2008)

[54] The LHCb Collaboration, "The LHCb Detector at the LHC", JINST 3, S08005 (2008)

[55] The Alice Collaboration, "The Alice Detector at the LHC", JINST 3, S08002 (2008)

[56] CMS Collaboration, "CMS Technical Design Report, volume II: Physics Performance", J. Phys. G, **34**, 995 (2007)

[57] CMS Collaboration, "The CMS magnet project: Technical Design Report", **CERN-LHCC-97-010** (1997)

[58] CMS Collaboration, "Precise mapping of the magnetic field in the CMS barrel yoke using cosmic rays", JINST **5**, T03021 (2010)

[59] CMS Collaboration, "The CMS tracker system project: Technical Design Report", **CERN-LHCC-98-006** (1998)

[60] CMS Collaboration, "The Tracker Project: Technical Design Report", **CERN-LHCC-98-006** (1998)

[61] CMS Collaboration, "The CMS tracker : Addendum to the Technical Design Report", **CERN-LHCC-2000-016** (2000)

[62] CMS Collaboration, "The CMS electromagnetic calorimeter project : Technical Design Report", **CERN-LHCC-97-033** (1997)

[63] R. Adolphi et al. "The CMS experiment at the CERN LHC", JINST, **3** S08004 (2008)

[64] CMS Collaboration, "The hadron calorimeter project: Technical Design Report", **CERN-LHCC-97-031** (1997)

[65] http://cms.web.cern.ch/news/cms-prepares-pixel-and-hcal-upgrades

[66] CMS Collaboration, "The CMS muon project: Technical Design Report", **CERN-LHCC-97-032** (1997)

[67] CMS Collaboration, "Performance of CMS Muon Reconstruction in pp Collision Events at $\sqrt{s} = 7$ TeV", JINST **7** P10002 (2012)

[68] CMS Collaboration, "CMS The TriDAS Project: Technical Design Report, Volume I", **CERN-LHCC-2000-038** (2000)

[69] CMS Collaboration, "CMS trigger and data-acquisition project: Technical Design Report", CERN, Geneva (2004)

[70] CMS Collaboration, "CMS TriDAS project: Technical Design Report, Volume I: The Trigger Systems", CERN, Geneva (2004)

[71] CMS Collaboration, "CMS trigger and data-acquisition project: Technical Design Raport, Volume II, **CERN-LHCC-2000-038** (2002)

[72] CMS Collaboration, "The CMS high level trigger", Eur. Phys. J. C **46** (3) 605667 (2006)

[73] W. Adam et al. "The CMS high level trigger" Eur. Phys. J. , C **667** (2006)

[74] T. Sjostrand, "Monte Carlo Generators", hep-ph-0611247 CERN-LCGAPP-2006-06, CERN-2007-005 [**hep-ph**] (2006)

[75] M. H. Seymour and M. Marx, "Monte Carlo Event Generators", arXiv:1304.6677 [**hep-ph**] (2013)

[76] P. Nason, "A new method for combining NLO QCD with shower Monte Carlo algorithms", JHEP **11** 040 (2004)

[77] S. Frixione, P. Nason, and C. Oleari, "Matching NLO QCD computations with Parton Shower simulations: the powheg method", JHEP **11** 070 (2007)

[78] S. Alioli et al., "NLO vector-boson production matched with shower in powheg", JHEP **07** 060 (2008)

[79] J. Allison et al., "Geant4 Developments and Applications", IEEE Transaction on nuclear science, **53** (2006)

[80] S. Banerjee, "Readiness of CMS Simulation towards LHC Startup", Jounal of Physis, Conference Series **119** 032006 (2008)

[81] T. Sjostrand, S. Mrenna, and P. Skand, "PYTHIA 6.4 Physics and Manual", JHEP **05** 026 (2006)

[82] https://twiki.cern.ch/twiki/bin/view/CMSPublic/LumiPublicResults\#2012_Proton_Proton_Collisions

[83] https://twiki.cern.ch/twiki/bin/viewauth/CMS/PdmV2012Analysis

[84] https://twiki.cern.ch/twiki/bin/viewauth/CMSPublic/L1TriggerDPGResults\#Links_to_approval_slides

[85] G. Alverson et al., "Search for High-Mass Resonances Decaying to Muon Pairs in pp Collisions at $\sqrt{s} =8$ TeV", CMS AN 2012/422 (2013), Internal CMS document

[86] CMS Collaboration, "CMS Tracking Performance Results from early LHC Operation", Eur. Phys. J. C70 1165 (2010)

[87] https://twiki.cern.ch/twiki/bin/view/CMSPublic/LumiPublicResults\#Pileup_distribution

[88] CMS Collaboration, "Search for Large Extra Dimensions in Dimuon Events in pp Collisions at $\sqrt{s}$ =8 TeV", CMS Physics Analysis Summary, $CMS-PAS-12-027$ (2013)

[89] P. Nadolsky et al., "Implications of CTEQ global analysis for colllider observables", Phys. Rev. D **78**, 013004 (2008)

[90] R. Vogt, "What is the Real K Factor?", arXiv:hep-ph/0207359

[91] R. Gavin et al., "FEWZ 2.0: A Code for Hadronic Z Produciton at Next-to-Next-to Leading Order", Comp. Phys. Comm. **182** 2388 (2011)

[92] S. Frixione and B. R. Webber, "Matching NLO QCD computations and parton shower simulations", JHEP 0206:029 (2002)

[93] G. Corcella et al., "Event generator for hadron emission reactions with interfering gluons (including supersymmetric processes)", JHEP 0101:010 (2001)

[94] C. M. Carloni et al., "Precision electroweak calculation of the production of a high transvers-momentum lepton pair at hadron colliders", JHEP 0710:109 (2009)

[95] Dimitri Bourilkov, Private Communication

[96] CMS Collaboration, "Search for Resonances in the Dilepton Mass Distribution in pp Collisions at $\sqrt{s}$ =8 TeV", CMS Physics Analysis Summary, $CMS-PAS-EXO-12-061$ (2013)

[97] H. L. Lai et al., "New parton distributions for collider physics", Phys. Rev. D **82**, 074024 (2010)

[98] A. D. Martin et al., "Parton distributions for the LHC", Eur. Phys. Journal C **63**, 189-285 (2009)

[99] M. Botje et al., "The PDF Working Group Interim Recommendations", arXiv:hep-ph/1101.0538v1

[100] P. M. Nadolsky and Z. Sullivan, "PDF uncertainties in WH production at Tevatron", arXiv:hep-ph/0110378v2

[101] CMS Collaboration, "Absolute Calibration of the Luminosity Measurement at CMS: Winter 2012 Update", CMS Physics Analysis Summary (2012), $CMS - PAS - SMP - 12 - 008$

[102] A. Read, "Presentation of search results: the CLs technique", J. Phys. G **28** 2693 (2002)

[103] T. Junk, "Confidence level computation for combining searches with small statistics", Nucl. Instrum. Meth. A **434** 435 (1999)

[104] T. Junk, "Sensitivity, Exclusion and Discovery with Small Signals, Large Backgrounds, and Large Systematic Uncertainties", CDF Document CDF/DOC/STATISTICS/PUBLIC/8128, (2007)

[105] J. Neyman and E. Pearson, "On the Problem of the Most Efficient Tests of Statistical Hypotheses", Philosophical Transactions of the Royal Society of London, Series A, Containing Papers of a Mathematical or Physical Character **231** 694706 (1933)

[106] S. S. Wilks, "The Large-Sample Distribution of the Likelihood Ratio for Testing Composite Hypotheses", The Annals of Mathematical Statistics **9** 60 (1938)

[107] K. Nakumara et al., "Particle Data Group", J. Phys. G**37** (2010)

[108] A. L. Read, "Modified frequentist analysis of search results (the CLs method)", First Workshop on Confidence Limits, CERN, Geneva (2000)

[109] F. Dulat and B. Mistlberger, "Limit setting procedures and theoretical uncertainties in Higgs boson searches", arXiv: 1204.3851v2 (2012)

[110] W. T. Eadie et al., "Statistical Methods in Experimental Physics", (North Holland, Amsterdam), pp. **76**, 79 (1971)

[111] F. James, "Statistical Methods in Experimental Physics", (World Scientific, Singapore, 2nd edition), pp. 83 2006

ABSTRACT

SEARCH FOR CONTACT INTERACTIONS USING THE DIMUON MASS SPECTRUM IN P-P COLLISIONS AT $\sqrt{S} = 8$ TeV AT CMS

by

CHAMATH KOTTACHCHI

May 2014

Advisor: Prof. Paul E. Karchin

Major: Physics

Degree: Doctor of Philosophy

The mass hierarchy problem associated with the standard model suggests that there might be more fundamental particles in nature. If quarks and leptons have substructures, known as preons, the manifestation of compositeness can be a four-fermion contact interaction. The experimental signal for contact interactions is a non-resonant enhancement of the number of events in the high-mass region of the dimuon mass spectrum. This dissertation describes a detailed search strategy for contact interactions using the Compact Muon Solenoid experiment. The dimuon mass spectrum above 300 GeV has been studied using the data collected in 2012 at $\sqrt{s} = 8$ TeV corresponding to an integrated luminosity of 20.6 fb^{-1}. Comparison of the observed mass spectrum with a fully simulated Monte Carlo prediction for the standard model shows no significant deviation. In the context of the left-left isoscalar model for contact interactions with compositeness energy scale Λ, exclusion lower limits are placed on Λ of 14.8 TeV and 12.4 TeV at a 95 % confidence level for constructive and destructive interference, respectively. The limits obtained from the study represent the most stringent limits to date.

AUTOBIOGRAPHICAL STATEMENT

CHAMATH KOTTACHCHI

EDUCATIONAL QUALIFICATIONS

Ph.D. Candidate in Physics, Wayne State University, Detroit, 2014
MS in Physics, Wayne State University, Detroit, 2011
BS in Physics, University of Colombo, Sri Lanka, 2004

PROFESSIONAL EXPERIENCE

Graduate Research Assistant, Wayne State University, 05/2012 - 05/2014
Graduate Teaching Assistant, Wayne State University, 08/2008 - 04/2012
Instructional Assistant, Wayne State University, 01/2008 - 08/2008
Senior Business Analyst for VS at Brandix, 09/2005 - 01/2007
Business Analyst for NIKE at MAS Holdings, 12/2003 - 08/2005

AWARDS AND AFFILIATIONS

Summer Dissertation Fellowship Award, Wayne State University, 2013
Thomas C. Rumble Fellowship Award, Wayne State University, 2012-2013
George B. and Eveline R. Award, Graduate Research Day, Department of Physics and
Astronomy, Wayne State University, 2012
Member of Sigma Xi, APS, and IEEE

SELECTED PUBLICATIONS AND PRESENTATIONS

Search for contact interactions in the dilepton mass spectra in pp collisions at $\sqrt{s} = 8$
TeV, CMS Collaboration, CMS PAS EXO-12-020 (2013)
Search for contact interactions in $\mu^+\mu^-$ events in pp collisions at $\sqrt{s} = 7$ TeV, CMS
Collaboration, Phys. Rev. D 87, 032001 (2013)
Search for Quark and Lepton Compositeness in the Dimuon Final State in pp Colli-
sions using the CMS Experiment, APS Meeting, Denver, Colorado, April 15th, 2013
Search for Contact Interactions in the Dilepton Channel, CMS Exotica Workshop,
Rome, Italy, November 10th, 2012
Cathode Strip Chamber Detector on Call Report, CSC Operation and Detector Per-
formance Group Meeting, Geneva, Switzerland, May 2nd and 9th, 2012
Angular Distribution of Muon Pairs Produced by the Drell-Yan Mechanism Compared
to an Exotic Model of Contact Interactions for High Energy pp Collisions, APS Meet-
ing, Atlanta, Georgia, April 3rd, 2012